SEMIANALYTICAL SATELLITE THEORY AND SEQUENTIAL ESTIMATION

by

Stephen Paul Taylor

B.S., University of Wisconsin - Madison
(1978)

Submitted in partial fulfillment of the
requirements for the degree of

MASTER OF SCIENCE

at the

MASSACHUSETTS INSTITUTE OF TECHNOLOGY

February 1982

© Stephen Paul Taylor, 1982

Signature of Author _____
Department of Mechanical Engineering
September 1981

Approved by _____
Paul J. Cefola, Thesis Advisor

Certified by _____
J. Karl Hedrick, Thesis Supervisor

Accepted by _____
Warren M. Rohsenow, Chairman
Department Graduate Committee

Archives
MASSACHUSETTS INSTITUTE OF TECHNOLOGY
JUN 7 1982
LIBRARIES

SEMIANALYTICAL SATELLITE THEORY AND SEQUENTIAL ESTIMATION

by

Stephen Paul Taylor
2LT, U. S. Army Engineers

Submitted to the Department of Mechanical Engineering in September 1981 in partial fulfillment of the requirements for the degree of Master of Science in Mechanical Engineering

ABSTRACT

Kalman Filtering techniques are combined with a semianalytical orbit generator to develop two sequential orbit determination algorithms, analogous to the standard Linearized Kalman Filter (LKF) and Extended Kalman Filter (EKF), respectively. The new algorithms are called the Semianalytical Kalman Filter (SKF) and the Extended Semianalytical Kalman Filter (ESKF). The design implications of the interaction between the filter and the perturbations theory are discussed. The results of numerical tests conducted to verify design assumptions are presented.

The new algorithms were implemented in the testbed provided by the Research and Development version of the Goddard Trajectory Determination System (RD GTDS). They are investigated for computational efficiency, accuracy, and radius of convergence by comparison with the special perturbations LKF and EKF previously implemented in the RD GTDS FILTER capability. A short-arc test case is used to examine transient behavior. A many-orbit test case using real observational data illustrates ESKF and EKF steady state performance in the presence of real-world observation and force model errors. The ESKF is shown to meet or exceed EKF performance for these tests.

An algorithm is derived that allows calculation of a suitable process noise strength based on a priori physical considerations. This algorithm is verified using the real data test case.

The real data test case led to the discovery of an interesting force model anomaly: a truncated 3x8 GEM 9 gravity field gave better prediction performance than the full 21x21 field. The satellite was in a low altitude orbit in sharp resonance with the 16th order geopotential harmonics. The atmosphere was relatively quiet. The 16th order GEM 9 gravitational coefficients are shown to account for the prediction performance degradation. Additional work is required.

Thesis Supervisor: J. K. Hedrick, Ph.D.
Title: Associate Professor of Mechanical Engineering

Thesis Supervisor: P. J. Cefola, Ph.D.
Title: Section Chief
The Charles Stark Draper Laboratory

Lecturer
Dept. of Aeronautics and Astronautics

ACKNOWLEDGEMENTS

I wish to thank my advisors, Prof. Karl Hedrick (MIT), and Dr. Paul Cefola (CSDL), for their continued patience and guidance throughout this thesis effort. I owe Paul especially a very sincere note of appreciation for his role in directly supervising my thesis research. I owe Dr. Richard Battin (MIT/CSDL) a warm note of thanks for my initial elegant introduction to Astrodynamics and the orbit determination problem in particular.

This thesis research has made extensive use of previous work in Semianalytical Satellite Theory. I wish to thank Wayne McClain, Leo Early, Capt. Andrew J. Green (USA), Dr. Sean Collins, Capt. Jeffery Shaver (USAF), Dr. Mark Slutsky, Dr. Ronald Proulx, and Mr. Aaron Bobick for the use of their work and for numerous discussions, suggestions, and support. These men have contributed greatly to the richness of my eductional experience during their tenure at CSDL.

During this thesis research, I have been privileged to have the benefit of help and advice from many members of the technical community at large. I wish to thank in particular Drs. Anne Long and Joan Dunham of the Computer Sciences Corporation, Art Fuchs and Danny Mistretta of NASA-Goddard, Jim Wright of General Electric Company, Ron Roehrich and Paul Major of ADCOM, and Lt. Neil McCasland (USAF) for their contributions to my thesis effort.

I wish to thank Bill Manlove, Kevin Daly, and Peter Kampion, all of CSDL, for their very tangible support and guidance during this work. Sandy Williams and Susan Fennelly of MIT have similarly been of very great assistance to me.

A final and very special note of thanks is due Karen Smith, who typed this thesis. The highly polished nature of the final document is due solely to the high level of her professional standards and a matching expertise.

This work has been performed while the author is on educational leave from the U.S. Army. The Fannie and John Hertz Foundation has been most generous in their support during that time.

I hereby assign my copyright of this thesis to the Charles Stark Draper Laboratory, Inc., Cambridge, Massachusetts.

Stephen Paul Taylor

Permission is hereby granted by the Charles Stark Draper Laboratory, Inc. to the Massachusetts Institute of Technology to reproduce any or all of this thesis.

TABLE OF CONTENTS

TABLE OF CONTENTS
(cont.)

LIST OF APPENDICES

LIST OF FIGURES

LIST OF TABLES

LIST OF TABLES
(cont.)

Chapter 1

INTRODUCTION

Orbit determination processes require two capabilities: the capability to accurately predict an orbit, given initial conditions; and some estimation algorithm indicating how observations of the satellite orbit should be used in updating the ephemeris. Advances in the technology of either capability imply corresponding advances in orbit determination processes. This thesis exploits recent advances in Semianalytical Satellite Theory to develop and test two new sequential orbit determination algorithms.

In their overview of earth satellite orbit determination, Kolenkiewicz and Fuchs [1] predict widespread use of sequential estimation techniques by the mid 1990's. Indeed, orbit determination systems relying on sequential algorithms are already operational, motivated by increases in timeliness, accuracy, or efficiency of the results. A literature search turned up several examples that highlight interestingly the differences between the algorithms designed herein and previous work.

1.1 Previous Work

Telesat [2], a satellite communications system, has been using a sequential algorithm to support station keeping operations for several years now, with both improved accuracy and reduced costs. This system uses an Extended Kalman Filter (EKF) in conjunction with a special perturbations ephemeris generator. Any orbit generator that applies

a high precision numerical integrator directly to a formulation of the equations of motion [e.g., Cowell, Encke, VOP] is called a Special Perturbation Theory. Special perturbations theories have the advantage of being highly accurate, but suffer from computational expense due to the small stepsizes required by the high precision integrators. The special perturbations filter developed by the Computer Sciences Corporation (CSC) in support of NASA/Goddard's study of autonomous navigation technology illustrates this point well. CSC recommends use of a 10 or 15 second stepsize in order to achieve the desired accuracy [3].

Alternate satellite theories exist, called General Perturbations theories, that use analytical methods to improve computational efficiency; they require simplifications in the force model for analytical tractability, implicitly causing losses in accuracy. The United States Air Force Aerospace Defense Command (ADCOM) maintains a catalog containing approximate ephemerides for all manmade earth satellites. Efficiency is mandatory for this large orbit determination task; ADCOM uses general perturbations satellite theories and a recursive least squares estimation algorithm to accomplish the routine updating of the catalog [4], [5]. However, a special perturbations theory is still required for high accuracy orbit determination.

The Global Positioning System (GPS) uses a sequential orbit determination system with an interesting architecture [6]. This system was designed to estimate the positions of the GPS satellites with a 1.5 meter accuracy in real time, while simultaneously having low operating costs for continuous operation. The expensive real time computations are minimized by using current observations to tune a

highly accurate prestored nominal trajectory with a Kalman Filter (LKF) linearized about that trajectory. The nominal trajectory and all other parameters needed by the filter are generated offline, once again with a special perturbations theory. One of the algorithms investigated in this thesis also uses a LKF to tune a prestored nominal trajectory.

The last example is the Epoch State Navigation Filter, not operationally employed, but proposed by Battin, Croopnik, and Lenox [7], and later studied in application to autonomous navigation by Menendez [3]. The use of a Variation of Parameters (VOP) formulation of the equations of motion is an essential similarity to Semianalytical Satellite Theory, although the above investigations employed special perturbations methods thereafter.

Semianalytical Satellite Theory represents a unification of the strengths of special perturbations and general perturbations methods. Semianalytical Satellite Theory starts with the same force model as special perturbations theories, so the same accuracy is achievable in principle. By using VOP equations of motion, only the perturbing forces must be integrated. The small magnitudes of these forces allows formal application of asymptotic methods, a step beyond that taken in investigations of the Epoch State Navigation Filter. The asymptotic method is aptly based on the method of averaging, which was developed by Krylov and Bogoliubov for analysis of nonlinear oscillations. Heuristically, the method of averaging removes the periodic content of the VOP equations of motion, allowing either analytical solution or numerical integration with large stepsizes. It is the latter approach where the fundamental

THIS PAGE INTENTIONALLY LEFT BLANK.

difference with general perturbations methods occurs: analytically intractable portions of the force model are treated numerically, preserving real world accuracy.

1.2 Semianalytical Satellite Theory at CSDL

Since the sequential orbit determination algorithms discussed in this thesis are based on the Semianalytical Satellite Theory currently being developed at the Charles Stark Draper Laboratory (CSDL), that theory is described in more detail below.

McClain [9] formulated the asymptotic expansion of this theory in terms of the Generalized Method of Averaging (GMA). Use of the GMA allows the rigorous and recursive development of formal equations for approximations of arbitrary order. Equinoctial variables were selected to avoid artificial singularities in the VOP equations for near circular or equatorial orbits. Cefola [10], McClain [11] and Collins [12] have developed analytical expressions for the averaged equinoctial element rates due to central and third body gravity perturbations, employing special functions and recursion relations to maintain force model generality and flexibility while maximizing efficiency. Green [13] formulated the numerical treatment of drag perturbations. More important for orbit determination processes, though was his development of a Fourier series expansion of the short periodic components averaged out of the osculating elements. It is the efficient recovery of these short periodics that makes this Semianalytical Satellite Theory as accurate as special perturbations theories while preserving the efficiency gains accruing from the analytical development. Recent work at CSDL has been

directed toward increasing the efficiency of short periodic recovery by further analytical development of the gravity perturbations [14], [15], [16], [17], [18], and the design of appropriate interpolation algorithms [19]. The resulting theory can be 5 to 100 times as efficient as special perturbations theories, depending on the application.

The Semianalytical Satellite Theory has been investigated for orbit determination before. Green's work was motivated by an interest in orbit determination processes for low altitude satellites. He used his results in a batch differential corrections (DC) estimation algorithm, finding accuracies and convergence properties quite comparable to high precision Cowell results. He also proposed a sequential algorithm that generated the interest motivating this work.

1.3 Overview of Thesis

This thesis reports on the application of semianalytical satellite theory to sequential orbit determination. The sequential estimation techniques used are adaptations of the Kalman Filter. Although the Kalman Filter is not the optimal solution to the nonlinear estimation problem posed by orbit determination, experience [20] has shown that it can be adapted to perform quite adequately.

The first algorithm design is quite similar to that used by the GPS system described above. The Semianalytical orbit generator is used to generate an averaged ephemeris and associated short periodic interpolators. Thus highly accurate values for the osculating satellite position and velocity can be recovered at observation times; the result-

ing observation residuals are used by a Kalman filter linearized about the mean trajectory to improve the estimate. The resulting algorithm is called the Semianalytical Kalman Filter (SKF).

Sequential orbit determination experience has shown that the EKF generally has much superior performance than global linearizations like the LKF. Another algorithm was designed that employs extended-type ideas where possible. This algorithm is called the Extended Semianalytical Kalman Filter (ESKF).

Chapter 2 presents mathematical introductions to semianalytical satellite theory and estimation theory as background for the SKF and ESKF designs.

Chapter 3 discusses the designs of the SKF and ESKF. These filters are based on the standard Kalman algorithms rather than on the square root or similar algorithms since numerical stability is not an issue in this implementation. The results of numerical tests which justify key assumptions are also presented.

Chapter 4 presents the results of orbit determination test cases employing simulated observations. These test cases serve to validate the software and give preliminary indications of the properties and performance of the SKF and ESKF.

Chapter 5 gives the results of EKF and ESKF application to real observational data. The results are very promising.

Conclusions and suggestions for future work are stated in Chapter 6.

The Appendices A and B discuss process noise modelling and the software implementation, respectively.

Chapter 2

BACKGROUND

This chapter presents the mathematical background required for the design of the Semianalytical Kalman Filters (SKF and ESKF) discussed in Chapter 3. Semianalytical satellite theory is described first to define the notation and motivate its advantages. An introduction to filtering theory surveys candidate estimation algorithms.

2.1 Semianalytical Satellite Theory

The accurate and efficient propagation of an ephemeris requires both a precise model of the forces acting on the satellite and an accurate and efficient means of integrating the equations of motion. The equations of motion are given by Newton's Second Law as

$$\frac{d^2\underline{r}}{dt^2} + \frac{\mu}{r^3}\underline{r} = \underline{a}_d \qquad (2\text{-}1)$$

The terms from left to right are the satellite's acceleration, the point-mass gravitational attraction, and all other (disturbing) accelerations, due to oblatness, drag, third bodies, etc. The disturbing accelerations are typically several orders of magnitude smaller than the point mass force.

Now any integrator is most accurate and efficient for systems with only small nonlinearities and low frequencies in the force model. Historically, this fact has motivated tradeoffs between analytical methods, which use simplified force models and analytical approximations to obtain the integrated ephemeris efficiently, and numerical methods, which retain the full force model and use high precision numerical integrators to obtain the integrated ephemeris quite accurately.

To increase the efficiency of an ephemeris generator, it is necessary to decrease both the magnitude of the nonlinearities as well as the high frequency content of the force model. The magnitude of the nonlinearities can be reduced by choice of the orbital elements. For example, Keplerian and equinoctial elements incorporate the effects of the point-mass acceleration, leaving only the disturbing acceleration to be accounted for. The transformation from cartesian position and velocity to such an element set is the basis of Gauss' VOP equations.

The VOP equations for a general satellite orbit can be written

$$\dot{\underline{a}} = \varepsilon \underline{f}(\underline{a}, \underline{\theta}) \qquad (2\text{-}2)$$

$$\dot{\underline{\theta}} = \underline{n}(\underline{a}) + \varepsilon \underline{g}(\underline{a}, \underline{\theta})$$

Here the vector $\underline{a}$ represents those elements describing the shape and plane of the orbit, while the vector $\underline{\theta}$ is an appropriate set of phase variables that accounts for the high frequency variations in the satellite acceleration. Examples of such phase variables are the satellite angle and the Greenwich Hour Angle. Sometimes the angle of the sun, moon, or a planet is considered a phase variable in examining third body perturbations. Alternatively, the motion of the third body can be modelled by taking time itself as a phase variable. The symbol ε formally denotes the small magnitudes of the generalized disturbing accelerations $\varepsilon\underline{f}(\underline{a},\underline{\theta})$ and $\varepsilon\underline{g}(\underline{a},\underline{\theta})$. Just as a satellite's mean anomaly is analagous to time through Kepler's equation, the close relationship between time and other phase variables is indicated in Equation (2-2) by the dominant term in $\dot{\underline{\theta}}$ being the generalized mean motion, $\underline{n}(\underline{a})$, a nonzero, almost constant rate. Since a satellite orbit is almost periodic in time, the generalized disturbing accelerations $\varepsilon\underline{f}(\underline{a},\underline{\theta})$ and $\varepsilon\underline{g}(\underline{a},\underline{\theta})$ are almost periodic in $\underline{\theta}$; this is consistent with the phase variables accounting for the high frequency components of the disturbing accelerations. Semianalytical Satellite Theory averages the VOP equations (2-2) over the periods of the phase variables. The method is illustrated below in developing a first order theory (in ε) with a single phase variable, taken to be the satellite angle. See McClain [9], Green [13], and Collins [12] for extensions to higher order, weak time dependence, and multiple phase angles, respectively. McClain's work is fundamental and comprehensive, while Green's and Collins' results show the power and success of semianalytical satellite theory in two applications.

2.1.1 A First Order Semianalytical Satellite Theory

When the satellite mean longitude is taken as the only phase variable, the VOP equations become

$$\dot{\underline{a}} = \varepsilon \underline{f}(\underline{a}, \lambda)$$

$$\dot{\lambda} = n(\underline{a}) + \varepsilon g(\underline{a}, \lambda) \qquad (2\text{-}3)$$

This development uses equinoctial variables, which can be expressed in terms of classical Keplerian element as

$$\underline{a} = [a, h, k, p, q,]^T$$

$a = a$, the semimajor axis

$h = e \sin(\omega + I\Omega)$

$k = e \cos(\omega + I\Omega)$

$p = \tan^I(i/2) \sin \Omega$ (2-4)

$q = \tan^I(i/2) \cos \Omega$

$\lambda = M + \omega + I\Omega$

$I = \pm 1$, the retrograde factor

Thus $n(\underline{a})$, in the expression for the rate of λ in Equation (2-3), is the mean motion

$$n(\underline{a}) = n(a) = \sqrt{\frac{\mu}{a^3}} \qquad (2\text{-}5)$$

If the right hand sides of equations (2-3) depended explicitly only on time, then periodicity would imply that $\underline{a}$ and λ could be expanded in a Fourier series whose coefficients were linearly dependent on the small parameter ε. In actuality, a Fourier series expansion in λ is asymptotically valid, but the dependence of the coefficients on ε is complex, making expansions of various orders possible. The Generalized Method of Averaging (GMA) developed by Mitropolsky provides a rigorous mathematical formalism for obtaining asymptotic approximations of arbitrary order. To first order, the results of the GMA are equivalent to averaging the VOP differential equations over the period of the satellite angle, $0 \leq \lambda \leq 2\pi$, to obtain mean element rates. The resulting mean elements correspond to the constant term in the Fourier series. The averaging operation is denoted by a super-bar, so that the mean elements are denoted $\bar{\underline{a}}$ and $\bar{\lambda}$. The relationship between the mean elements and the unaveraged or osculating elements is stated by the near-identity transformation

$$\begin{aligned} \underline{a} &= \bar{\underline{a}} + \varepsilon \underline{\eta}(\bar{\underline{a}}, \bar{\lambda}) \\ \lambda &= \bar{\lambda} + \varepsilon \eta_6(\bar{\underline{a}}, \bar{\lambda}) \end{aligned} \qquad (2\text{-}6)$$

The functions $\underline{\varepsilon\eta}$ and $\varepsilon\eta_6$ are called the short periodic functions and to first order account for the periodic terms in the Fourier series; thus they satisfy the constraints

$$\varepsilon\eta_i(\underline{\bar{a}}, \bar{\lambda} + 2\pi) = \varepsilon\eta_i(\underline{\bar{a}}, \bar{\lambda}) \tag{2-7}$$

and

$$\int_0^{2\pi} \varepsilon\eta_i(\underline{\bar{a}}, \bar{\lambda})\, d\bar{\lambda} = 0 \tag{2-3}$$

for $i = 1,2,\ldots,6$.

Since the mean elements are obtained by integrating the average of the equations of motion (2-3), the mean element rates cannot depend on λ or $\bar{\lambda}$. Thus the equations of motion for the mean elements can be written

$$\dot{\underline{\bar{a}}} = \varepsilon\, \underline{A}(\underline{\bar{a}})$$

$$\dot{\bar{\lambda}} = \bar{n} + \varepsilon\, A_6(\underline{\bar{a}}) \tag{2-9}$$

The mean element rates and short periodic functions are completely determined by asymptotic matching between Equations (2-3) and (2-9), applying as constraints the near identity transformation (2-6) and short periodic properties (2-7) and (2-8). The matching is most easily carried out by formal Taylor series expansion; differentiate (2-6) to obtain

$$\dot{\underline{a}} = \dot{\bar{\underline{a}}} + \frac{\partial \varepsilon \underline{\eta}}{\partial \bar{\underline{a}}} \dot{\bar{\underline{a}}} + \frac{\partial \varepsilon \underline{\eta}}{\partial \bar{\lambda}} \dot{\bar{\lambda}}$$

$$\dot{\lambda} = \dot{\bar{\lambda}} + \frac{\partial \varepsilon \eta_6}{\partial \bar{\underline{a}}} \dot{\bar{\underline{a}}} + \frac{\partial \varepsilon \eta_6}{\partial \bar{\lambda}} \dot{\bar{\lambda}} \qquad (2\text{-}10)$$

Substituting for $\dot{\bar{\underline{a}}}$ and $\dot{\bar{\lambda}}$ from (2-9) and retaining terms to first order in ε for the asymptotic match gives

$$\dot{\underline{a}} = \varepsilon \underline{A}(\bar{\underline{a}}) + \frac{\partial \varepsilon \underline{\eta}}{\partial \bar{\lambda}} \bar{n}$$

$$\dot{\lambda} = \bar{n} + \varepsilon A_6(\bar{\underline{a}}) + \frac{\partial \varepsilon \eta_6}{\partial \bar{\lambda}} \bar{n} \qquad (2\text{-}11)$$

Equation (2-3) asymptotically becomes

$$\dot{\underline{a}} = \varepsilon \underline{f}(\bar{\underline{a}}, \bar{\lambda})$$

$$\dot{\underline{\lambda}} = n(\bar{a}) + \frac{\partial n(\bar{a})}{\partial \bar{a}} (a - \bar{a}) + \varepsilon q(\bar{\underline{a}}, \bar{\lambda}) \qquad (2\text{-}12)$$

since the residuals $\underline{a} - \bar{\underline{a}}$ and $\lambda - \bar{\lambda}$ are first order in ε. By differentiating the equation for the mean motion, (2-5), the final result is

$$\dot{\bar{\underline{a}}} = \varepsilon \underline{f}(\bar{\underline{a}}, \bar{\lambda})$$

$$\dot{\bar{\lambda}} = \bar{n} - \frac{3}{2} \frac{\bar{n}}{\bar{a}} \varepsilon \eta_1(\bar{\underline{a}}, \bar{\lambda}) + \varepsilon g(\bar{\underline{a}}, \bar{\lambda}) \qquad (2\text{-}13)$$

Explicit equations for the mean element rates and short periodic functions result from comparison of equations (2-11) and (2-13) and application of the constraints (2-7) and (2-8). Comparison yields

$$\varepsilon \underline{f}(\bar{\underline{a}}, \bar{\lambda}) = \varepsilon \underline{A}(\bar{\underline{a}}) + \frac{\partial \varepsilon \underline{\eta}}{\partial \bar{\lambda}} \bar{n}$$

$$\varepsilon g(\bar{\underline{a}}, \bar{\lambda}) - \frac{3\bar{n}}{2\bar{a}} \varepsilon \eta_1(\bar{\underline{a}}, \bar{\lambda}) = \varepsilon A_6(\bar{\underline{a}}) + \frac{\partial \varepsilon \eta_6}{\partial \bar{\lambda}} \bar{n} \qquad (2\text{-}14)$$

Integration over $0 \leq \bar{\lambda} \leq 2\pi$ allows application of (2-7) and (2-8) by use of the identities

$$\int_0^{2\pi} \frac{\partial \varepsilon \eta_i(\bar{\underline{a}},\bar{\lambda})}{\partial \bar{\lambda}} \bar{n}\, d\bar{\lambda} = \bar{n}[\varepsilon \eta_i(\bar{\underline{a}},\bar{\lambda}+2\pi) - \varepsilon \eta_i(\bar{\underline{a}},\bar{\lambda})] = 0$$

(2-15)

and

$$\int_0^{2\pi} \frac{\bar{n}}{\bar{a}} \varepsilon \eta_1(\bar{\underline{a}},\bar{\lambda})\, d\bar{\lambda} = \frac{\bar{n}}{\bar{a}} \int_0^{2\pi} \varepsilon \eta_1(\bar{\underline{a}},\bar{\lambda})\, d\bar{\lambda} = 0$$

(2-16)

Carrying out the averaging of equations (2-14) yields

$$\varepsilon \underline{A}(\bar{\underline{a}}) = \frac{1}{2\pi} \int_0^{2\pi} \varepsilon \underline{f}(\bar{\underline{a}},\bar{\lambda})\, d\bar{\lambda}$$

$$\varepsilon A_6(\bar{\underline{a}}) = \frac{1}{2\pi} \int_0^{2\pi} \varepsilon q(\bar{\underline{a}},\bar{\lambda})\, d\bar{\lambda} \qquad (2\text{-}17)$$

With the εA_i now known, equations (2-14) become a set of coupled partial differential equations. The solution satisfying the constraints is easily verified to be

$$\varepsilon\, \underline{\eta}(\bar{\underline{a}},\bar{\lambda}) = \frac{1}{\bar{n}} \int_0^{\bar{\lambda}} [\varepsilon\, \underline{f}(\bar{\underline{a}},\xi) - \varepsilon\, \underline{A}(\bar{\underline{a}})]\, d\xi + \varepsilon\, \underline{\eta}(\bar{\underline{a}},0)$$

$$\varepsilon\, \eta_6(\bar{\underline{a}},\bar{\lambda}) = \frac{1}{\bar{n}} \int_0^{\bar{\lambda}} [\varepsilon\, g(\bar{\underline{a}},\xi) - \varepsilon A_6(\bar{\underline{a}})]\, d\xi$$

$$- \frac{3}{2\bar{a}} \int_0^{\bar{\lambda}} \varepsilon\, \eta_1(\bar{\underline{a}},\xi)\, d\xi + \varepsilon\, \underline{\eta}_6(\bar{\underline{a}},0)$$

(2-18)

Equations (2-17) and (2-18) provide a natural structure to ephemeris generation by Semianalytical Satellite Theory. The Averaged Orbit Generator (AOG) computes the mean elements by use of (2-9) and (2-17); the Short Periodic Generator (SPG) recovers the short peridic variations by solution of (2-18). These equations are still purely formal results. The efficiency and accuracy of Semianalytical Satellite Theory depend on maximizing the analytical development, with numerical methods used when further analysis is not possible. Thus the averaging of gravity perturbations in (2-17) is done completely analytically [10], [11], while the mean element rates due to drag and solar radiation are computed by numerical quadrature [21]. Additional formal development of the short periodic functions is possible. The approach due to Green [13] is described below.

2.1.2 Fourier Series Development of the Short Periodics

Accurate solution of the VOP equations by semianalytical satellite theory requires recovery of the short periodic variations. But direct application of equations (2-18) is undesirable, since integration of the osculating force model would once again require small stepsizes. The constraint equations (2-7) and (2-8) imply that the short periodic functions can be developed in a Fourier series in the mean-mean longitude, $\bar{\lambda}$. Green [13] developed this expansion to achieve generality in the short-periodic model; this concept also leads to improved computational efficiency.

The SPG equations (2-18) imply that the disturbing forces also have a Fourier series expansion. The derivation starts with the assumption of such an expansion

$$\varepsilon\, \underline{f}(\bar{\underline{a}},\bar{\lambda}) = \varepsilon\, \underline{X}_0(\bar{\underline{a}}) + \sum_{\sigma=1}^{\infty} \varepsilon \underline{X}_\sigma(\bar{\underline{a}}) \cos \sigma\bar{\lambda}$$

$$+ \varepsilon \underline{Z}_\sigma(\bar{\underline{a}}) \sin \sigma\bar{\lambda}$$

$$\varepsilon\, q(\bar{\underline{a}},\bar{\lambda}) = \varepsilon X_{6,0}(\bar{\underline{a}}) + \sum_{\sigma=1}^{\infty} \varepsilon\, X_{6,\sigma}(\bar{\underline{a}}) \cos \sigma\bar{\lambda}$$

$$+ \varepsilon\, Z_{6,\sigma}(\bar{\underline{a}}) \sin \sigma\bar{\lambda} \qquad (2\text{-}19)$$

The Fourier coefficients of the disturbing forces can be written as

$$\varepsilon \underline{X}_0(\bar{\underline{a}}) = \frac{1}{2\pi} \int_0^{2\pi} \varepsilon \underline{f}(\bar{\underline{a}},\bar{\lambda})\, d\bar{\lambda} = \varepsilon \underline{A}(\bar{\underline{a}})$$

$$\varepsilon X_{6,0}(\bar{\underline{a}}) = \frac{1}{2\pi} \int_0^{2\pi} \varepsilon q(\bar{\underline{a}},\bar{\lambda})\, d\bar{\lambda} = \varepsilon A_6(\bar{\underline{a}})$$

$$\begin{Bmatrix} \varepsilon \underline{X}_\sigma(\bar{\underline{a}}) \\ \varepsilon \underline{Z}_\sigma(\bar{\underline{a}}) \end{Bmatrix} = \frac{1}{\pi} \int_0^{2\pi} \varepsilon \underline{f}(\bar{\underline{a}},\bar{\lambda}) \begin{Bmatrix} \cos \sigma\bar{\lambda} \\ \sin \sigma\bar{\lambda} \end{Bmatrix} d\bar{\lambda}$$

$$\begin{Bmatrix} \varepsilon X_{6,\sigma}(\bar{\underline{a}}) \\ \varepsilon Z_{6,\sigma}(\bar{\underline{a}}) \end{Bmatrix} = \frac{1}{\pi} \int_0^{2\pi} \varepsilon q(\bar{\underline{a}},\bar{\lambda}) \begin{Bmatrix} \cos \sigma\bar{\lambda} \\ \sin \sigma\bar{\lambda} \end{Bmatrix} d\bar{\lambda}$$

(2-20)

The Fourier coefficients of the short periodic functions can be related to these known coefficients of the disturbing function by substituting equations (2-19) into (2-18) and carrying out the integration explicitly.

Write the short periodic expansions as

$$\varepsilon\, \underline{\eta}(\bar{\underline{a}},\bar{\lambda}) = \sum_{\sigma=1}^{\infty} \varepsilon \underline{C}_\sigma \sin \sigma\bar{\lambda} - \varepsilon \underline{D}_\sigma \cos \sigma\bar{\lambda}$$

$$\varepsilon\, \eta_6(\bar{\underline{a}},\bar{\lambda}) = \sum_{\sigma=1}^{\delta} \varepsilon C_{6,\sigma} \sin \sigma\bar{\lambda} - \varepsilon D_{6,\sigma} \cos \sigma\bar{\lambda} \qquad (2\text{-}21)$$

The short periodic Fourier coefficients may finally be solved for as

$$\varepsilon \underline{C}_\sigma(\bar{\underline{a}}) = \frac{1}{\sigma\bar{n}}\, \varepsilon\, \underline{X}_\sigma(\bar{\underline{a}})$$

$$\varepsilon \underline{D}_\sigma(\bar{\underline{a}}) = \frac{1}{\sigma\bar{n}}\, \varepsilon\, \underline{Z}_\sigma(\bar{\underline{a}})$$

$$\varepsilon\, C_{6,\sigma}(\bar{\underline{a}}) = \frac{1}{\sigma\bar{n}}\, \varepsilon\, X_{6,\sigma}(\bar{\underline{a}}) + \frac{3}{2\sigma\bar{a}}\, \varepsilon\, D_{1,\sigma}(\bar{\underline{a}})$$

$$\varepsilon\, D_{6,\sigma}(\bar{\underline{a}}) = \frac{1}{\sigma\bar{n}}\, \varepsilon\, Z_{6,\sigma}(\bar{\underline{a}}) - \frac{3}{2\sigma\bar{a}}\, \varepsilon\, C_{1,\sigma}(\bar{\underline{a}}) \qquad (2\text{-}22)$$

Although this formulation still requires implicit integrations of the disturbing force models as in equations (2-20), three factors contribute greatly to efficiency gains

1. the integrations can be done analytically for all gravity perturbations;
2. the Fourier coefficients depend only on the slowly varying mean elements, and so vary slowly themselves, allowing extensive use of interpolators [13];
3. the series converge quickly, and so can be truncated at low harmonics.

Computational issues for the whole of Semianalytical Satellite Theory are discussed in more detail below after discussing the variational equations.

2.1.3 General Notation

The development so far has emphasized the essentially different mathematical character of the satellite angle $\bar{\lambda}$, and the other orbital elements, $\bar{a}$, by deriving separate equations for each. While this distinction is necessary to understand and implement Semianalytical Satellite Theory, it is less important for the application of Semianalytical Satellite Theory to orbit determination. By using vector notational conventions similar to the scalar Kronecker Delta, a common description of both the $\bar{\lambda}$ and the $\bar{a}$ equations can be developed. The unified equations are presented in Table 2-1, referenced to the text above by "primed" equation numbers. The rest of the thesis will reference the equations in Table 2-1.

Table 2-1
Unified Equations for First Order
Semianalytical Satellite Theory

Indicial vector

$$\underline{e}_i^T = [0 \ldots 010 \ldots 0]^T$$

↑ ith element, out of six elements

Orbital Elements

$$\underline{a}^T = [a,h,k,p,q,\lambda] \qquad (2\text{-}4)'$$

VOP Equations

$$\dot{\underline{a}} = n\underline{e}_6 + \epsilon \underline{f}(\underline{a}) \qquad (2\text{-}3)'$$

Near Identity Transformation

$$\underline{a} = \bar{\underline{a}} + \epsilon \underline{\eta}(\bar{\underline{a}}) \qquad (2\text{-}6)'$$

Mean Element Equations

$$\dot{\bar{\underline{a}}} = \bar{n}\, \underline{e}_6 + \epsilon \underline{A}(\bar{\underline{a}}) \qquad (2\text{-}9)'$$

Mean Element Rates

$$\epsilon \underline{A}(\bar{\underline{a}}) = \frac{1}{2\pi} \int_0^{2\pi} \epsilon \underline{f}(\bar{\underline{a}})\, d\bar{\lambda} \qquad (2\text{-}17)'$$

Short Periodic Functions

$$\epsilon \underline{\eta}(\bar{\underline{a}}) = \frac{1}{\bar{n}} \int^{\bar{\lambda}} [\epsilon \underline{f}(\bar{\underline{a}}) - \epsilon \underline{A}(\bar{\underline{a}})]\, d\bar{\lambda}$$

$$- \frac{3}{2\bar{a}} \underline{e}_6 \cdot \int^{\bar{\lambda}} \epsilon \underline{\eta}_1(\bar{\underline{a}})\, d\bar{\lambda} \qquad (2\text{-}18)'$$

Generalized Disturbing Acceleration Fourier Series Coefficients

$$\begin{Bmatrix} \varepsilon X_\sigma(\bar{a}) \\ \varepsilon Z_\sigma(\bar{a}) \end{Bmatrix} = \frac{1}{\pi} \int_0^{2\pi} \varepsilon f(\bar{a}) \begin{Bmatrix} \cos \sigma\bar{\lambda} \\ \sin \sigma\bar{\lambda} \end{Bmatrix} d\bar{\lambda} \quad (\sigma \geq 1) \qquad (2\text{-}20)'$$

Short Periodic Function Fourier Series Coefficients

$$\varepsilon C_\sigma(\bar{a}) = \frac{1}{\sigma\bar{n}} \varepsilon X_\sigma(\bar{a}) + \frac{3}{2\sigma\bar{a}} e_6 \varepsilon D_{1,\sigma}(\bar{a})$$

$$\varepsilon D_\sigma(\bar{a}) = \frac{1}{\sigma\bar{n}} \varepsilon Z_\sigma(\bar{a}) - \frac{3}{2\sigma\bar{a}} e_6 \varepsilon C_{1,\sigma}(\bar{a}) \qquad (2\text{-}22)'$$

Short Periodic Function Fourier Series

$$\varepsilon\eta(\bar{a}) = \sum_{\sigma=1}^{\infty} \varepsilon C_\sigma \sin \sigma\bar{\lambda} - \varepsilon D_\sigma \cos \sigma\bar{\lambda} \qquad (2\text{-}21)'$$

2.1.4 The Variational Equations

In addition to prescribing the method of computing a satellite's state over time, most satellite theories also indicate how to compute the variational equations, or partial derivatives of the satellite motion. These partials are required for orbit determination; the variational equations and all other partial derivatives required for orbit determination with Semianalytical Satellite Theory are presented here, following Green's development [13].

The variational equations describe to first order the effects of small perturbations or variations in the initial conditions on the satellite motion at later times. The equations of motion are linearized about the motion corresponding to the nominal initial conditions, resulting in a linearized differential equation describing the propagation of the perturbation. The state transition matrix of this differential equation is also called the matrix of partial derivatives of the satellite motion. For Semianalytical Satellite Theory, the partial derivatives of the motion give the dependence of the mean equinoctial elements at a time t_1 to the mean elements at an earlier time t_0. Denote the state transition matrix by $\Phi(t_1,t_0)$; then

$$\Phi(t_1,t_0) = \frac{\partial\, \bar{\underline{a}}(t_1)}{\partial\, \bar{\underline{a}}(t_0)} \qquad (2\text{-}23)$$

is a notational identity. Letting t_1 be an arbitrary time t and differentiating with respect to time gives

$$\dot{\Phi}(t,t_0) = \frac{d}{dt} \frac{\partial \bar{\underline{a}}(t)}{\partial \bar{\underline{a}}(t_0)} = \frac{\partial \dot{\bar{\underline{a}}}(t)}{\partial \bar{\underline{a}}(t_0)} \qquad (2\text{-}24)$$

Application of the chain rule for the partial derivatives with respect to $\bar{\underline{a}}(t_0)$ and substitution of equations (2-9) for the mean element rates gives

$$\dot{\Phi}(t,t_0) = \{\frac{\partial \varepsilon \underline{A}(\bar{\underline{a}})}{\partial \bar{\underline{a}}(t)} - \frac{3\bar{n}}{2\bar{a}} \underline{e}_6 \underline{e}_1^T\} \Phi(t,t_0) \qquad (2\text{-}25)$$

The effects of variations of dynamic parameters in the equations of motion are also described by variational equations. Let $\underline{c}$ be the vector of dynamic parameters and define

$$\psi(t,t_0) = \frac{\partial \bar{\underline{a}}(t)}{\partial \underline{c}} \qquad (2\text{-}26)$$

Chain rule expansion of the derivative of equation (2-26) gives rise to two terms in the variational equation for $\Psi(t,t_0)$

$$\dot{\Psi}(t,t_0) = \left\{\frac{\partial \varepsilon\ \underline{A}(\bar{\underline{a}})}{\partial\ \bar{\underline{a}}(t)} - \frac{3\bar{n}}{2\bar{a}}\ \underline{e}_6\underline{e}_1^T\right\} \Psi(t,t_0) + \frac{\partial \varepsilon\ \underline{A}(\bar{\underline{a}})}{\partial \underline{c}}$$

(2-27)

The first term accounts for variations in the mean element rates due to the implicit dependence of $\bar{\underline{a}}(t)$ on $\underline{c}$; the second term describes the explicit dependence of the rates. Use of Green's notation [13]

$$A(t) = \frac{\partial \varepsilon\ \underline{A}(\bar{\underline{a}})}{\partial\ \bar{\underline{a}}(t)} - \frac{3\bar{n}}{2\bar{a}}\ \underline{e}_6\underline{e}_1^T$$

$$D(t) = \frac{\partial \varepsilon\ \underline{A}(\bar{\underline{a}})}{\partial \underline{c}} \qquad (2\text{-}28)$$

$$B_2(t) = \Phi(t,t_0)$$

$$B_3(t) = \Psi(t,t_0)$$

gives his results for the Averaged Partial Generator (APG)

$$\dot{B}_2 = AB_2 \qquad (2\text{-}29)$$

$$\dot{B}_3 = AB_3 + D$$

The initial conditions for equations (2-25), (2-27), and (2-29) state the independence of the variables $\underline{\bar{a}}(t_0)$ and $\underline{c}$ for a fixed time t_0

$$\Phi(t_0,t_0) = B_2(t_0) = I$$

$$\Psi(t_0,t_0) = B_3(t_0) = 0 \qquad (2\text{-}30)$$

Since the desired output of Semianalytical Satellite Theory is the high accuracy osculating position and velocity at a given time t, the partials with respect to the corresponding mean elements are also needed. The transformation from mean elements to osculating position and velocity occurs in two steps: the near identity transformation (2-6) gives the osculating equinoctial elements, which are then converted to position and velocity by a well-known transformation [22]. The partial derivatives are developed by chain rule as

$$\frac{\partial \underline{x}(t)}{\partial \underline{\bar{a}}(t)} = \frac{\partial \underline{x}(t)}{\partial \underline{a}(t)} \cdot \left[I + \frac{\partial\ \varepsilon \underline{\eta}(\underline{\bar{a}})}{\partial \underline{\bar{a}}} \right] \qquad (2\text{-}31)$$

Here $\underline{x}$ is the six component vector of position and velocity; substitution of (2-6) results in the form of the second factor.

For special perturbations theories, the osculating position and velocity do not have any dependence on the dynamical parameter $\underline{c}$ if the orbital elements at the same time are also taken as independent variables. However, the explicit dependence of the short periodics on the disturbing forces, shown in (2-18), does result in nontrivial partials for Semianalytical Satellite Theory. Specifically

$$\frac{\partial \underline{x}(t)}{\partial \underline{c}} = \frac{\partial \underline{x}(t)}{\partial \underline{a}(t)} \cdot \frac{\partial \varepsilon \underline{\eta}(\bar{\underline{a}})}{\partial \underline{c}} \tag{2-32}$$

when $\bar{\underline{a}}(t)$ and $\underline{c}$ are taken as the independent variables. In Green's notation

$$B_1 = \frac{\partial \varepsilon \underline{\eta}(\bar{\underline{a}})}{\partial \bar{\underline{a}}}$$

$$B_4 = \frac{\partial \varepsilon \underline{\eta}(\bar{\underline{a}})}{\partial \underline{c}} \tag{2-33}$$

giving

$$\frac{\partial \underline{x}(t)}{\partial \bar{\underline{a}}(t)} = \frac{\partial \underline{x}(t)}{\partial \underline{a}(t)} \cdot [I + B_1]$$

$$\frac{\partial \underline{x}(t)}{\partial \underline{c}} = \frac{\partial \underline{x}(t)}{\partial \underline{a}(t)} \cdot B_4 \tag{2-34}$$

The partials of the transformation from osculating equinoctial elements to position and velocity are well-known and can be computed explicitly; the B_1, B_2, B_3, and B_4 matrices must be computed by the Semianalytical orbit generator. The details of computation of these and other outputs of Semianalytical Satellite Theory are discussed next. The computation of the B_2 and B_3 matrices is performed by the Averaged Partial Generator (APG); the B_1 and B_4 matrices are computed by the Short Periodic Partial Generator (SPPG).

2.1.5 Computational Aspects of Semianalytical Satellite Theory

The central goal of Semianalytical Satellite Theory is the development of the general formulation of a satellite's equations of motion for optimal computational efficiency. Full use has been made of special functions, recursive computation, and truncatable expansions in the analytical development of the AOG and the SPG. Thus each evaluation of a mean element rate or a short periodic Fourier series coefficient has been made as efficient as possible while still maintaining the generality of the theory. In an orbit determination environment, the osculating position and velocity must be computed at arbitrary times and arbitrarily frequently, to allow utilization of the observations. Semianalytical Satellite Theory relies heavily on global and local interpolation strategies developed by L. Early [19], A. Bobick [23], and P. Cefola [19] to meet this requirement efficiently. It is the interaction with these interpolators that constrains the design of a sequential estimation algorithm. Their structure is discussed here in detail.

2.1.5.1 Mean Element and Variational Equation Computations

The fundamental property of the averaged equations of motion (2-9), (2-25), and (2-27) is the absence of high frequency terms. Integration stepsizes from a half day for low altitude cases to several days for high altitude cases easily preserve computational accuracy. A self-starting Runge-Kutta integrator provides the flexibility to handle problems of any arc length. The mean element rates are computed by either analytical averages or numerical averaging quadratures. Computation of the A and D matrices (2-28) for computing the rates in the variational equations (2-29) can be done analytically for the oblateness perturbation, or by central finite differences applied to the mean element rates for all other perturbations. A hermite interpolator recovers the values of the mean elements and the partial derivatives of the motion (referenced to epoch) at output times. The state transition matrix between two arbitrary times t_1 and t_2 is computed by the semigroup property

$$\Phi(t_2,t_1) = \Phi(t_2,t_0)\ \Phi(t_0,t_1) \qquad (2\text{-}35)$$

and its corollary

$$\Phi(t_0,t_1) = \Phi^{-1}(t_1,t_0) \qquad (2\text{-}36)$$

The same hermite interpolator used to compute the partials $\Phi(t,t_0)$ can be used to compute its matrix inverse in (2-36) by using the rate equation

$$\dot{\Phi}^{-1}(t,t_0) = - \Phi^{-1}(t,t_0)\, \dot{\Phi}(t,t_0)\, \Phi^{-1}(t,t_0) \qquad (2\text{-}37)$$

This equation is obtained by differentiating the identity $\Phi(t,t_0)\, \Phi^{-1}(t,t_0) = I$.

A similar development can be used to calculate the partial derivatives of the motion with respect to the dynamic parameters at arbitrary times, from epoch referenced values. The variational equation interpolator computes the solution $\Psi(t,t_0)$ to equation (2-27) at required output times. The solution to equation (2-27) can be written formally by variation of parameters as

$$\Psi(t,t_0) = \int_{t_0}^{t} \Phi(t,\tau)\, D(\tau)\, d\tau \qquad (2\text{-}38)$$

The partials $\Psi(t_2,t_1)$ between arbitrary times t_1 and t_2 can be computed by expanding this integral

$$\int_{t_0}^{t_2} \Phi(t_2,\tau)\, D(\tau)\, d\tau = \Phi(t_2,t_1) \int_{t_0}^{t_1} \Phi(t_1,\tau)\, D(\tau)\, d\tau + \int_{t_1}^{t_2} \Phi(t_2,\tau)\, D(\tau)\, d\tau \qquad (2\text{-}39)$$

Appropriate identification of the terms leads to the desired result

$$\Psi(t_2,t_1) = \Psi(t_2,t_0) - \Phi(t_2,t_1)\,\Psi(t_1,t_0) \qquad (2\text{-}40)$$

Use of (2-35) and (2-40) allows all needed mean quantities to be computed quite efficiently. The interpolator for the transition matrix inverse results in off-diagonal elements on the order of 10^{-10}, compared to 10^{-16} for the exact inverse.

2.1.5.2 Short Periodic Coefficient Computation

As part of his study of the Fourier series expansion of the short periodic functions, Green examined the computation of the coefficients. Since the coefficients depend only on the slowly varying mean elements and not on the mean-mean longitude $\bar{\lambda}$, smooth time histories are expectable. Green [13] verified this hypothesis; his plots of short periodic coefficients show very smooth behavior over several-day spans. Early [19] implemented a variable order Lagrangian interpolator for these coefficients with the same stepsize as the Runge-Kutta interator. He found accuracies depending on the order and the stepsize as shown in Table 2-2. Since the short periodic coefficients have to be evaluated only once per step, it is clear that large gains in efficiency can be made even with low densities of output points.

Table 2-2
Short-Periodic Coefficient Interpolator Errors

Points	Step (days)	Zonal Errors*			Drag Errors**		
		ΔC_a(m)	ΔC_p(m)	ΔC_λ(m)	ΔC_a(m)	ΔC_p(m)	ΔC_λ(m)
2	.25	.86	.064	.76	.001	0	.001
	.5	3.5	.26	3.1	.001	.0002	.001
	1.	14.0	1.0	12.	.024	.0004	.036
3	.25	.012	0	.011	.002	0	.002
	.5	.098	.004	.086	.005	.0001	.008
	1.	.78	.029	.69	.008	.0003	.011
4	.25	0	0	0	.128		.175
	.5	.002	0	.002	.263		.054
	1.	.015	.004	.021	.576		.011

*These errors are the position errors caused by errors in the interpolated coefficients for the 2λ short-periodic. The step size is the interval between successive interolation points.

**These errors are the position errors caused by errors in the interpolated coefficients for the 1λ short periodic.

2.1.5.3 Position and Velocity Interpolation

Many orbit determination situations call for infrequent station passes, with high data rate sensors taking large numbers of observations to achieve the desired accuracy. Now each call of the short periodic coefficient interpolator described above requires the computation of six coefficients for each frequency retained in the Fourier series expansion (usually at least five). Then the Fourier series must be summed in order to obtain the short periodics, and finally, the resulting osculating equinoctial elements must be transformed to position and velocity. In high data rate situations, the computational load would grow rapidly. To accomodate such cases more efficiently, L. Early developed low order, short arc interpolators for the osculating position and velocity; P. Cefola developed corresponding interpolators for the partial derivatives of position and velocity with respect to the epoch mean elements. Typical interpolator stepsizes are one or two minutes, with arc lengths up to 9 or 10 minutes. Early used a hermite interpolator for position and a Lagrangian interpolator for velocity; Cefola used a Lagrangian interpolator for the partial derivatives. The variation of the accuracy of the position and velocity interpolator with order and stepsize is shown in Table 2-3. The performance of both interpolators has been assessed in batch differential corrections (DC) orbit determination tests; with their use the Semi-analytical Satellite Theory has exceeded special perturbations Cowell in efficiency.

Table 2-3
Position and Velocity Interpolation Errors

Points	Step (sec)	Δz(m)	Δv_z(mm/sec)
2	60	.72	.074
	120	11.6	.392
	180	59	.833
	240	185	10.6
	480	2650	640
3	60	.002	.043
	120	.092	1.08
	180	.98	7.4
	240	5.1	29
	480	305	880

The reference position and velocity values were generated by the Cowell high precision orbit generator for an AE-C elliptical orbit over a ten-minute interval around perigee, with a 4x4 Earth potential model, sun, moon, and Harris-Priester atmosphere model.

The step size is the interval between successive interpolation points, in seconds.

2.1.6 Summary of Semianalytical Satellite Theory

The salient features of the Semianalytical Satellite Theory under development at CSDL have been discussed. The existing literature gives more details on analytical derivations and on accuracy and efficiency comparisons with special perturbations Cowell. The constraints the theory places on a sequential estimation algorithm have been introduced and will become clearer after the introduction to filtering theory in the next section. The next chapter will use this material as background for the design of a Semianalytical Kalman Filter.

2.2 Introduction to Sequential Estimation Theory

The problem of orbit determination is the accurate and efficient estimation of a satellite ephemeris given observational data. Sequential estimation algorithms are desirable since they make immediate use of new observations, giving real-time availability of the optimal estimate of the ephemeris. Satellite observations are taken at discrete points in time; the Semianalytical Satellite Theory discussed above will be used to propagate the ephemeris estimate from observation time to observation time. A filtering algorithm is needed to specify how to determine a new estimate after receipt of another observation. This section presents results from sequential estimation theory, as background for the design of the complete orbit determination algorithms in the next chapter.

2.2.1 Problem Formulation

Modern estimation theory requires a probabilistic model for the orbit determination problem. The Semianalytical equations of motion (2-9)' are modelled as

$$\dot{\underline{z}}(t) = \underline{f}(\underline{z},t) + \underline{w}(t); \quad \underline{z}(t_0) = \underline{z}_0 \qquad (2\text{-}41)$$

The state vector $\underline{z}(t)$ is the estimated solve-for vector and includes the mean equinoctial elements $\underline{a}(t)$ and other dynamical solve parameters. Thus we can write

$$\underline{z}(t) = \begin{bmatrix} \bar{\underline{a}}(t) \\ \underline{c} \end{bmatrix} \qquad (2\text{-}42)$$

where $\underline{c}$ is the vector of dynamical solve parameters, such as the coefficient of drag. The deterministic force model is represented by the function $\underline{f}(\underline{z},t)$; equation (2-42) implies that $\underline{f}(\underline{z},t)$ depends on the mean element rates $\epsilon\, \underline{A}(\underline{a})$. Notice that the presence of the perturbation parameter ϵ is not of direct significance in the estimation problem. The vector $\underline{w}(t)$ is a Gaussian white noise process. It is a random input used to account for model errors in the dynamics; examples of such errors are given by atmospheric density or solar radiation pressure model errors, geopoten-

tial coefficient errors, and approximations in the analytical development of the equations of motion. The statistics assumed for the process noise $\underline{w}(t)$ and the initial condition $\underline{z}_0$ are

$$
\begin{aligned}
&E\{\underline{w}(t)\} = \underline{0} \\
&E\{\underline{w}(t)\ \underline{w}^T(\tau)\} = Q(t)\ \delta(t-\tau) \qquad (2\text{-}43) \\
&E\{\underline{z}_0\} = \bar{\underline{z}}_0 \\
&E\{(\underline{z}_0 - \bar{\underline{z}}_0)(\underline{z}_0 - \bar{\underline{z}}_0)^T\} = P_0
\end{aligned}
$$

The function $\delta(\cdot)$ is the Dirac delta function and satisfies

$$\delta(t) = 0 \qquad (t \neq 0) \qquad (2\text{-}44)$$

and

$$\int_{-\infty}^{\infty} f(t)\ \delta(t) = f(0) \qquad (2\text{-}45)$$

These properties of the delta function imply

$$\delta(0) \simeq \infty \tag{2-46}$$

so that this function is not well defined in the usual sense.

The notation $E\{\cdot\}$ denotes the expected value of a random variable. For a given random variable $\underline{x} = [x_1,\ldots,x_n]^T$, the associated probability density function is denoted by

$$P_{\underline{X}}(\underline{x}) = P_{X_1,\ldots,X_n}(x_1,\ldots,x_n) \tag{2-47}$$

Using this notation the expected values of $\underline{x}$ and a function $\underline{f}(\underline{x})$ are computed by

$$\bar{\underline{x}} = E\{\underline{x}\} = \int_{-\infty}^{\infty} \underline{x}\, P_{\underline{X}}(\underline{x})\, d\underline{x} \tag{2-48}$$

and

$$\bar{\underline{f}}(\bar{\underline{x}}) = E\{\underline{f}(\underline{x})\} = \int_{-\infty}^{\infty} \underline{f}(\underline{x})\, P_{\underline{X}}(\underline{x})\, d\underline{x} \tag{2-49}$$

The integral notation here is defined

$$\int d\underline{x} = \int dx_1 \ldots \int dx_n \qquad (2\text{-}50)$$

Observations of the satellite ephemeris are modelled by

$$y_k = h(\underline{z}(t_k),t_k) + v_k \qquad (2\text{-}51)$$

for increasing times t_k ($k = 1,2,\ldots$). Here the function $h(\underline{z}(t_k),t_k)$ represents the deterministic model of the mechanism for obtaining the observation y_k of the current satellite state, $\underline{z}(t_k)$. The measurement noise v_k describes all model errors; there are many present in any measurement process. The statistics of the v_k are

$$E\{v_k\} = 0$$

$$E\{v_k v_\ell\} = R_k \delta_{k\ell} \qquad (2\text{-}52)$$

for $k, \ell=1,2,\ldots$ The symbol $\delta_{k\ell}$ is the Kronecker delta, defined by

$$\delta_{k\ell} = \begin{cases} 0, & \text{if } k \neq \ell \\ 1, & \text{if } k = \ell \end{cases} \qquad (2\text{-}53)$$

These statistics imply that the kth measurement y_k is unbiased with variance R_k, and that the errors for different observations are independent.

Equations (2-41) through (2-53) provide a general formulation of the orbit determination problem for application of estimation theoretic results. Cases where the process noise is correlated, the measurement noise is correlated or state-dependent, or the measurements are biased, can all be treated in the above context by appropriate augmentation of the state, $\underline{z}$, and redefinition of the functions $\underline{f}(\underline{z},t)$ and $h(\underline{z},t)$ [20]. Further extensions or a rigorous formulation requires use of the Ito calculus or measure theory.

2.2.2 Optimal Linear Filtering

There are many definitions of an optimal estimate. In the linear case, most of them are equivalent and result in the Kalman Filter. The fundamental criterion for orbit determination applications is the minimum mean square error criterion. With this criterion, the optimal estimate is the conditional mean of the state given the measurements. Let $\underline{z}_k$ be the value of the stochastic process $\underline{z}(t)$ in (2-41) at time $t = t_k$. Let $\underline{Y}_\ell$ be the set of observations y_i in (2-51) up to and including time t_ℓ

$$\underline{Y}_\ell = \{y_1, y_2, \ldots, y_\ell\} \tag{2-54}$$

Use the notation $\hat{\underline{z}}_k^{\ell}$ to represent the estimate of the process at time t_k based on the set of observations $\underline{Y}_{\ell}$. When $k=\ell$, this estimate is the filter solution; when $k>\ell$, the estimate is a prediction, and when $k<\ell$, the estimate is a smoothed estimate. Using this notation, the mean square error of the filtering estimate at time k is

$$J_K = E\{(\underline{z}_k - \hat{\underline{z}}_k^k)^T(\underline{z}_k - \hat{\underline{z}}_k^k)\} \qquad (2\text{-}55)$$

Choosing $\hat{\underline{z}}_k^k$ to minimize the mean square error yields the conditional mean estimate

$$\hat{\underline{z}}_k^k = E_{\underline{Z}_k|\underline{Y}_k}\{\underline{z}_k|\underline{Y}_k\} \qquad (2\text{-}56)$$

When the dynamics and measurement models are linear, equations (2-41) and (2-51) become

$$\dot{\underline{z}}(t) = F(t)\,\underline{z}(t) + \underline{w}(t)\ ;\ \underline{z}(t_0) = \underline{z}_0 \qquad (2\text{-}57)$$

and

$$y_k = H_k\,\underline{z}(t_k) + v_k \qquad (2\text{-}58)$$

The statistics of $\underline{z}_0$, $\underline{w}(t)$ and v_k are given by equations (2-43) and (2-52), respectively.

The Kalman filter gives an optimal estimate of $\underline{z}(t)$. The filter has a natural division into two parts, a prediction algorithm and an update algorithm. These equations are well-known and are summarized below.

The prediction algorithm yields the optimal prediction $\hat{\underline{z}}_k^{k-1}$ and its covariance P_k^{k-1} for use in processing the new observation y_k. The state is predicted by

$$\hat{\underline{z}}_k^{k-1} = \Phi(t_k, t_{k-1})\ \hat{\underline{z}}_{k-1}^{k-1}$$

$$\dot{\Phi}(t, t_{k-1}) = F(t)\ \Phi(t, t_{k-1}) \qquad (2\text{-}59)$$

$$\Phi(t_{k-1}, t_{k-1}) = I$$

The covariance is predicted by

$$P_k^{k-1} = \Phi(t_k, t_{k-1})\ P_{k-1}^{k-1}\ \Phi^T(t_k, t_{k-1}) + \Lambda(t_k, t_{k-1})$$

$$\Lambda(t_k, t_{k-1}) = \int_{t_{k-1}}^{t_k} \Phi(t_k, \tau)\ Q(\tau)\ \Phi^T(t_k, \tau)\ d\tau \qquad (2\text{-}60)$$

Notice that the predictions depend only on the previous filtered estimates. The new filtered estimates similarly depend only on the latest predictions. The update algorithm computes the new filtered estimate and is given by

$$K_k = P_k^{k-1} H_k^T (H_k P_k^{k-1} H_k^T + R_k)^{-1} \qquad (2\text{-}61)$$

$$\hat{\underline{z}}_k^k = \hat{\underline{z}}_k^{k-1} + K_k(y_k - H_k \hat{\underline{z}}_k^{k-1}) \qquad (2\text{-}62)$$

and

$$P_k^k = (I - K_k H_k) P_k^{k-1} \qquad (2\text{-}63)$$

The Kalman Filter equations form the basis of many practical nonlinear estimation algorithms. Three such algorithms are discussed next.

2.2.3 Suboptimal Nonlinear Filters

The above section discusses the Kalman Filter. When all the random variables are Gaussian, it is the optimal solution to the linear filtering problem. In the more general case, where either the initial condition, process noise or measurement noise is not Gaussian, the Kalman Filter is optimal only among estimators with a linear form. Most extensions of the Kalman Filter to nonlinear estima-

tion problems make additional linearizing assumptions, based on a perturbation series expansion of the system equations (2-41) and (2-51). The method and its justification are illustrated by the following scalar example.

Let $h(x)$ be a given differentiable function of the random variable x. Let x have mean $\bar{x}$ and variance σ^2. The Taylor series expansion of $h(x)$ around $\bar{x}$

$$h(x) = h(\bar{x}) + h'(\bar{x})\ (x - \bar{x}) + \frac{1}{2}\, h''(\bar{x})\ (x - \bar{x})^2 + \ldots \qquad (2\text{-}64)$$

can be used to evaluate the expected value of the function $h(x)$. Substitution of (2-64) into the expectation operator and use of its linearity gives

$$E\{h(x)\} = h(\bar{x}) + \frac{1}{2}\, h''(\bar{x})\ \sigma^2 + \frac{1}{6}\, h'''(\bar{x})\ E\{(x - \bar{x})^3\} + \ldots \qquad (2\text{-}65)$$

An additional assumption that x is Gaussian allows further development of (2-65). All odd order terms must vanish, while even order terms can be calculated explicitly in terms of σ^2. The fourth order term [in (2-65)] is $1/8\ h^{(4)}(x)\sigma^4$, as compared with $1/24\ h^{(4)}(x)\ (x-\bar{x})^4$, which is the term in the original expansion (2-64) of $h(x)$. In general, the nth order term in (2-64)

will become nth order in σ when its expected value is computed. Thus the convergence properties of the two series will be similar, with (2-64) faster when $|x-\bar{x}| << \sigma$ and vice versa when $|x-\bar{x}| >> \sigma$. Depending on the magnitude of σ, equation (2-65) can be truncated at first or second order with little accuracy loss.

Suboptimal filters for the nonlinear estimation problem posed in equations (2-41) through (2-53) can be derived by applying the above expansion method to the force model $\underline{f}(\underline{z},t)$ and observation model $h(\underline{z},t)$. When the perturbation series are truncated at first order, either the Extended Kalman Filter (EKF) or the Linearized Kalman Filter (LKF) result. When terms through second order are retained, the result is called a Gaussian Second Order Filter. These filters require the estimation errors to be small. The difference between the filter estimate and the true state will grow unstably due to neglected nonlinearities if the estimation errors ever get too large. Divergence can also result from errors in the force model or observation model. Jazwinski has designed two filters to control filter divergence. One filter [24] adaptively adjusts the process noise covariance to provide feedback on filter gains magnitude; the other [25] actively estimates model errors and subtracts their effects from the filter estimate. Since divergence is not a problem in most orbit determination applications, these two filters are not presented here. Only the extended, linearized, and second order filters are presented here.

2.2.3.1 The EKF

The Extended Kalman Filter results from direct application of the method presented in equations (2-64) and (2-65). Perturbation series truncated at first order are used for both the dynamics and observation models. The expansions are based on the last filter estimate, $\hat{\underline{z}}_{k-1}^{k-1}$; it is tacitly assumed that $\hat{\underline{z}}_{k-1}^{k-1}$ is in fact the mean of the true state. For the state prediction the perturbation equation is

$$\underline{z}(t) = \bar{\underline{z}}(t) + \Delta\underline{z}(t) \tag{2-66}$$

The assumed mean $\bar{\underline{z}}(t)$ obeys

$$\begin{aligned} \dot{\bar{\underline{z}}}(t) &= \underline{f}(\bar{\underline{z}}(t),t) \\ \bar{\underline{z}}(t_{k-1}) &= \hat{\underline{z}}_{k-1}^{k-1} \end{aligned} \tag{2-67}$$

Differentiation of (2-66) gives

$$\dot{\underline{z}}(t) = \dot{\bar{\underline{z}}}(t) + \Delta\dot{\underline{z}}(t) \tag{2-68}$$

while expansion of $f(\underline{z},t)$ in (2-41) yields

$$\dot{\underline{z}}(t) = \underline{f}(\bar{\underline{z}},t) + F(t)\ \Delta\underline{z}(t) + \underline{w}(t) \qquad (2\text{-}69)$$

where

$$F(t) = \left.\frac{\partial f(\underline{z},t)}{\partial \underline{z}}\right|_{\bar{\underline{z}}(t)} \qquad (2\text{-}70)$$

Thus the perturbation $\Delta\underline{z}(t)$ obeys

$$\Delta\dot{\underline{z}}(t) = F(t)\ \Delta\underline{z}(t) + \underline{w}(t) \qquad (2\text{-}71)$$

The solve vector prediction is the conditional mean; thus it is predicted by

$$\hat{\underline{z}}_k^{k-1} = \bar{\underline{z}}(t_k) \qquad (2\text{-}72)$$

The covariance is predicted by application of the usual KF prediction equations to (2-71). The prediction equations for the EKF are

$$\hat{\underline{z}}_k^{k-1} = \underline{\bar{z}}(t_k)$$

$$\dot{\underline{\bar{z}}}(t) = \underline{f}(\underline{\bar{z}}(t),t) \qquad (2\text{-}73)$$

$$\underline{\bar{z}}(t_{k-1}) = \hat{\underline{z}}_{k-1}^{k-1}$$

$$P_k^{k-1} = \Phi(t_k,t_{k-1})\ P_{k-1}^{k-1}\ \Phi^T(t_k,t_{k-1}) + \Lambda(t_k,t_{k-1})$$

$$\dot{\Phi}(t,t_{k-1}) = F(t)\ \Phi(t,t_{k-1})$$

$$\Phi(t_{k-1},t_{k-1}) = I \qquad (2\text{-}74)$$

$$\Lambda(t_k,t_{k-1}) = \int_{t_{k-1}}^{t_k} \Phi(t_k,\tau)\ Q(\tau)\ \Phi^T(t_k,\tau)\ d\tau$$

where F(t) is defined in equation (2-70). The EKF update equations also use the perturbation equation (2-66). The measurement equation (2-51) is expanded to yield

$$y_k = h(\hat{\underline{z}}_k^{k-1},t_k) + H_k\ \underline{\Delta z}(t_k) + v_k \qquad (2\text{-}75)$$

where

$$H_k = \left.\frac{\partial h(\underline{z}_k, t_k)}{\partial \underline{z}_k}\right|_{\underline{z}_k = \hat{\underline{z}}_k^{k-1}} \tag{2-76}$$

Since $\hat{\underline{z}}_k^{k-1}$ is assumed to be the mean of the process, the predicted observation is

$$\hat{y}_k^{k-1} = h(\hat{\underline{z}}_k^{k-1}, t_k) \tag{2-77}$$

The EKF is estimating the correction $\Delta\underline{z}(t_k)$ to be added to $\underline{z}^{k-1}$; this estimate is accomplished by the same update equations as the Kalman Filter algorithm (2-61) to (2-63).

2.2.3.2 The LKF

The Extended Kalman Filter continually updates the integration trajectory in Equation (2-67), used for the dynamics and observation model linearizations, (2-70) and (2-76). The trajectory update is based on the latest state estimate; thus the computations in (2-67), (2-70), and (2-76) must all be done in real time. The Linearized Kalman Filter allows more efficient computation by assuming a global nominal trajectory for the integration (2-67) and linearizations; the filter estimates the nonzero mean correction to this trajectory by the usual Kalman Filter equations. This filter is more attractive for use with Semianalytical Satellite Theory due to the latter's ability to generate long time trajectories (e.g., 1 day or more) very efficiently. The derivation of the LKF is straightforward; only new equations are presented here.

A nominal trajectory for the LKF is generated exactly as it is for the EKF, by

$$\dot{\underline{z}}_N(t) = \underline{f}(\underline{z}_N, t)$$

$$\underline{z}_N(t_0) = \bar{\underline{z}}_0 \tag{2-78}$$

The perturbed system becomes

$$\Delta\dot{\underline{z}}(t) = F_N(t)\,\Delta\underline{z}(t) + \underline{w}(t)$$

$$\Delta y_k = H_{N_k}\,\Delta\underline{z}(t_k) + v_k \tag{2-79}$$

where Δy_k is computed from the real observation y_k by

$$\Delta y_k = y_k - h(\underline{z}_N(t_k), t_k) \tag{2-80}$$

The linear coefficients $F_N(t)$ and H_{N_k} in (2-79) are computed by linearization about the nominal trajectory

$$F_N(t) = \left.\frac{\partial \underline{f}(\underline{z}, t)}{\partial \underline{z}}\right|_{\underline{z} = \underline{z}_N(t)}$$

$$H_{N_k} = \left.\frac{\partial h(\underline{z}_k, t_k)}{\partial \underline{z}_k}\right|_{\underline{z}_k = \underline{z}_N(t_k)} \tag{2-81}$$

The Kalman Filter equations are now applied directly to the system (2-79) to produce the estimate. Since the nominal trajectory is not locally updated, the estimated corrections $\Delta\hat{z}_k^k$ can become quite large; the LKF tends to produce less accurate estimates and to diverge sooner than the EKF. One means of correcting this problem is to use the Second Order Gaussian Filter discussed next.

2.2.3.3 The Second Order Gaussian Filter

The Second Order Gaussian Filter retains terms through second order in the perturbation expansion (2-64). The contributions of the new second order terms are analyzed by assuming a Gaussian probability distribution, giving rise to the filter name. Second order filters tend to have better accuracy and convergence characteristics than either the LKF or EKF, since nonlinearities are accounted for to second order. Second order filters have been derived by Widnall [26] and Athans, et al. [27]; second order analysis of nonlinearities was first done by Denham and Pines [28]. Gelb [29] and Jazwinski [20] contain complete derivations as part of their surveys of nonlinear estimation techniques. In this paper, the Second Order Gaussian Filter is used only for the analysis of the effects of nonlinearities for the SKF; thus only the new equations are presented.

Gelb defines a linear operator (eq. 6.1-25 of Ref 29)

$$\partial^2(g,B) = \text{trace}\left\{\left[\frac{\partial^2 g}{\partial x_p \partial x_q}\right] B\right\} \qquad (2\text{-}82)$$

The arguments are a scalar function $g(\underline{x})$ and a matrix B [$\underline{x}$ is (nx1), B is (nxn)]. Using this operator, a dynamical bias correction term is computed, using B = P, the estimate covariance, and $g = f_i(\underline{z},t)$, the ith component of the force model $\underline{f}(\underline{z},t)$. The ith component of the bias is

$$b_i = \partial^2(f_i,P) \tag{2-83}$$

The EKF prediction equation (2-73) becomes

$$\dot{\bar{\underline{z}}}(t) = \underline{f}(\bar{\underline{z}},t) + \frac{1}{2}\,\underline{b} \tag{2-84}$$

while the LKF prediction equation for $\Delta\underline{z}(t)$ becomes

$$\Delta\dot{\bar{\underline{z}}} = F_N(t)\ \Delta\dot{\bar{\underline{z}}} + \frac{1}{2}\,\underline{b} \tag{2-85}$$

The bias due to an observation nonlinearity is

$$c = \partial^2(h,P) \tag{2-86}$$

The predicted observations are corrected

$$\hat{y}_k^{k-1} = h(\hat{\underline{z}}_k^{k-1}, t_k) + \frac{1}{2} c \qquad (2\text{-}87)$$

for the EKF [see (2-77)], and

$$\Delta y_k = y_k - h(\underline{z}_N(t_k), t_k) - \frac{1}{2} c \qquad (2\text{-}88)$$

for the LKF [see (2-80)].

There is also a second order correction to the predicted measurement covariance used in the Kalman gain computation; this correction effectively augments the measurement noise R_k. The covariance correction is not needed for the analysis of nonlinearities and so is not included here.

2.2.4 Summary of Estimation Theory

Nonlinear estimation theory has been introduced and three estimation algorithms were presented. The LKF appears to have better computational form, but the EKF should perform better in the presence of large nonlinearities. The Second Order Gaussian Filter uses bias correction terms to reduce nonlinear effects; these terms can be used to assess the impact of nonlinearities. The next section uses the discussions of Semianalytical Satellite Theory and Filtering Theory to design a Semianalytical Kalman Filter.

Chapter 3

SEMIANALYTICAL FILTER DESIGN

This chapter discusses the design of two sequential estimation algorithms for use with Semianalytical Satellite Theory. They are analogous to the Linearized Kalman Filter (LKF) and the Extended Kalman Filter (EKF) discussed previously; they are called the Semianalytical Kalman Filter (SKF) and the Extended Semianalytical Kalman Filter (ESKF) respectively.

When Semianalytical Satellite Theory is cast in an orbit determination role, two time frame definitions are important:

1. the integration grid is the time frame used by the integrator and associated short-periodic coefficient interpolators in the software implementation;

2. the observation grid specifies the arrival times of observations and consequently the output times for the satellite position and velocity generated by the integrator.

The Semianalytical Satellite Theory implementation discussed previously makes it clear that the efficient operation of Semianalytical Satellite Theory cannot allow relinearization of the equations of motion within the integration grid. Relinearization should occur only at the boundary of an integration grid; since the integrator is self-starting, it can be relinearized at the cost of one

additional evaluation of the mean element and variational equation force models. The resulting interaction between the filter and the integrator on their respective time frames is shown in Figure 3-1. The relationships shown in Figure 3-1 apply to both the SKF and the ESKF.

It is clear that the SKF can be designed by the straightforward application of LKF ideas with the Semianalytical integrator. The ESKF requires some approximations before EKF concepts are used. Before these designs are presented, the issue of the filter solve vector is discussed.

3.1 Solve-Vector Choice

The choice of the filter solve-vector is not always trivial. For example, for two-body dynamics Keplerian elements would be a much more natural solve vector than position and velocity; this example is striking in that the element choice makes the equations of motion linear.

For more general force models, the dynamics are nonlinear regardless of element choice. The equations of motion and the observation model must then be linearized for application of the LKF or EKF equations. By use of the chain rule and the linearity of the filter equations, it follows immediately that the solve vector choice is mathematically irrelevant to the computation of the filter correction, as long as the nominal trajectory is not updated. When the nominal trajectory is updated, second and higher order terms in the element set transformation cause differences in the updated trajectories.

Figure 3-1. The Interaction of the Filter (Obs Grid) and the Integrator (Integration Grid) when the Integrator is Relinearlized

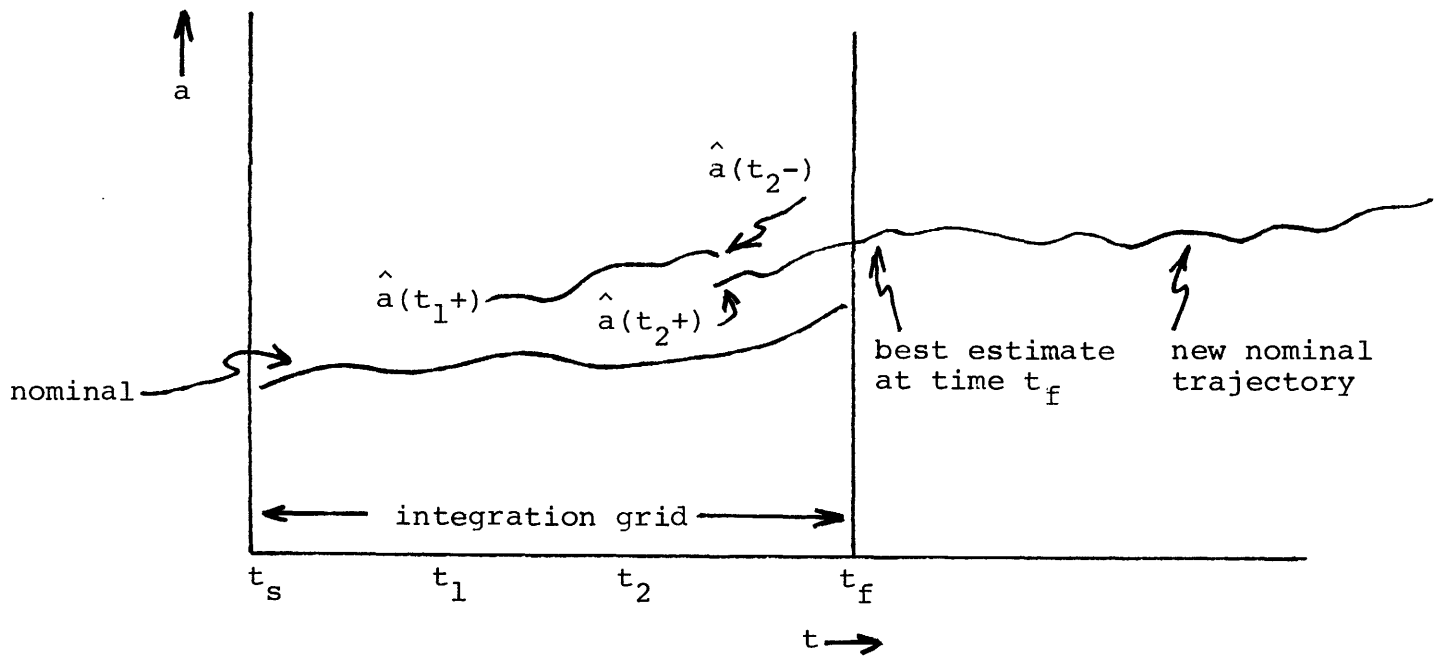

Notes: (i) The integrator generates the nominal trajectory on the integration grid (from t_s to t_f)

(ii) Observations occur at times t_n, (n = 1,2,...); here t_2 is the last observation time in the grid shown

(iii) The filter produces the estimates $\hat{a}(t_n^+)$ as pictured

The Semianalytical Differential Corrections (SDC) software at CSDL can update both the epoch mean position and velocity and the mean equinoctial elements. Generally, no distinct trends have been observed in either SDC accuracy or convergence rate with the choice of update elements.

The equations for the Second Order Gaussian Filter include bias correction terms depending on the second partials of the force model and observation model with respect to the solve vector. These second partials do not transform linearly; application of the chain rule yields a term containing the second partial of the element transformation. For example, the equation

$$\frac{\partial^2 h}{\partial \underline{a}^2} = \left(\frac{\partial \underline{x}}{\partial \underline{a}}\right)^T \left(\frac{\partial^2 h}{\partial \underline{x}^2}\right) \left(\frac{\partial \underline{x}}{\partial \underline{a}}\right) + \left(\frac{\partial h}{\partial \underline{x}}\right) \left(\frac{\partial^2 \underline{x}}{\partial \underline{a}^2}\right) \qquad (3\text{-}1)$$

describes the transformation of the second partial of the observation model with respect to the element sets $\underline{a}$ and $\underline{x}$. Clearly solve vector choice will affect filter performance here, but in a complex and unpredictable way.

The natural solve vector for Semianalytical filters uses the mean equinoctial elements, $\bar{\underline{a}}(t)$, produced by the integrator. Since the SKF and ESKF use linear filter equations and the trajectory will be updated relatively infrequently, this choice should have minimal impact on accuracy. The solve vector may also include dynamic parameters, $\underline{c}$, when they are estimated.

3.2 SKF Design

The SKF algorithm is a direct result of the application of the LKF algorithm to the Semianalytical Satellite Theory. Although conceptually simple, the implementation is more complex due to the interaction of the observation grid and integration grid, as shown in Figure 3-1. The algorithm is detailed explicitly below to emphasize this interaction. The algorithm statement is broken down by operations performed on the integration grid and those performed on the observation grid. The integration grid operations are usually executed much less frequently than the observation grid operations, due to the long integration stepsizes allowed by Semianalytical Satellite Theory. Due to the use of a Runge-Kutta integrator, it suffices to consider only one integration step; all others are processed identically.

3.2.1 Operations on the Integration Grid

1. At time $t = t_0$ update the nominal initial state for the new integration grid with the filter correction from the previous grid

$$\underline{z}_{N_0} = \bar{\underline{z}}_0 + \Delta\hat{\underline{z}}_0^0 \quad \text{where} \quad \underline{z} = \begin{bmatrix} \bar{\underline{a}} \\ \underline{c} \end{bmatrix}$$

Update the initial covariance $P_0 = P_0^0$

Initialize the filter correction and transition matrices

$$\hat{\Delta z}_0 = \underline{0}$$

$$\Phi(t_0,t_0) = I$$

$$\Psi(t_0,t_0) = 0, \text{ save in } \Psi_s$$

$$\Phi^{-1}(t_0,t_0) = I, \text{ save in } \Phi_s$$

and compute force evaluations for the equations of motion and variational equations

$$\dot{\bar{a}}_N(t_0),\ \dot{\Phi}(t_0,t_0),\ \dot{\Psi}(t_0,t_0), \text{ and } \dot{\Phi}^{-1}(t_0,t_0)$$

2. Do the averaged integration until time $t = t_0 + \Delta t$

obtain $\bar{a}_N(t)$, $\Phi(t,t_0)$, $\Psi(t,t_0)$ and

invert $\Phi(t,t_0)$ to get $\Phi^{-1}(t,t_0)$

evaluate the corresponding rates to allow set up of the mean interpolators for

$$\bar{a}_N,\ \Phi,\ \Psi,\ \Phi^{-1}$$

3. Compute short periodics $\varepsilon\underline{C}_\sigma(\bar{\underline{a}}_N)$, $\varepsilon\underline{D}_\sigma(\bar{\underline{a}}_N)$

at time t_0 and t for set up of the short periodic coefficient interpolators

3.2.2 Operations on the Observation Grid

The SKF executes the following steps when a new observation is received.

1. Obtain the new observation, $y(t_i)$, at time $t = t_i$

2. Interpolate for $\bar{\underline{a}}_N(t_i)$, $\Phi(t_i,t_0)$, $\Psi(t_i,t_0)$

we already have $\Phi^{-1}(t_{i-1},t_0)$ in Φ_s

3. Interpolate for short periodic coefficients

$$\varepsilon\underline{C}_\sigma(\bar{\underline{a}}_N(t_i)),\ \varepsilon\underline{D}_\sigma(\bar{\underline{a}}_N(t_i))$$

4. Construct the osculating elements

$$\underline{a}_N(t_i) = \bar{\underline{a}}_N(t_i) + \sum_{\sigma=1}^{N} \varepsilon\underline{C}_\sigma \sin \sigma\bar{\lambda} - \varepsilon\underline{D}_\sigma \cos \sigma\bar{\lambda}$$

transform to cartesian coordinates $\underline{x}_N(t_i)$

5. Compute the nominal observation

$$y_N(t_i) = h(\underline{x}_N(t_i),t_i) = h(\underline{z}_N(t_i),t_i)$$

and the observation residual

$$\Delta y(t_i) = y(t_i) - y_N(t_i)$$

compute the observation partials

$$H_i = \frac{\partial h}{\partial \underline{z}_N}(\underline{z}_N,t_i) = \frac{\partial h}{\partial \underline{a}}\left[I + B_1 \vdots B_4\right]$$

$$B_1 = \frac{\partial \varepsilon \underline{\eta}_1(\bar{\underline{a}}_N)}{\partial \bar{\underline{a}}_N}$$

$$B_4 = \frac{\partial \varepsilon \underline{\eta}_1(\bar{\underline{a}}_N)}{\partial \underline{c}}$$

6. Compute the transition matrix and variational partials

$$\Phi(t_i,t_{i-1}) = \Phi(t_i,t_0)\,\Phi_s$$

$$\Psi(t_i,t_{i-1}) = \Psi(t_i,t_0) - \Phi(t_i,t_{i-1})\,\Psi_s$$

using $\Phi_s = \Phi^{-1}(t_{i-1},t_0)$, and $\Psi_s = \Psi(t_{i-1},t_0)$

7. Obtain predicted solve vector and covariance

$$\Delta\hat{\underline{a}}_i^{i-1} = \Phi(t_i,t_{i-1})\,\Delta\hat{\underline{a}}_{i-1}^{i-1} + \Psi(t_i,t_{i-1})\,\Delta\hat{\underline{c}}_{i-1}^{i-1}$$

$$\underline{\Delta c}_i^{\hat{}\,i-1} = \underline{\Delta c}_{i-1}^{\hat{}\,i-1}$$

$$P_i^{i-1} = \begin{bmatrix} \Phi(t_i,t_{i-1}) & \Psi(t_i,t_{i-1}) \\ 0 & I \end{bmatrix} P_{i-1}^{i-1} \begin{bmatrix} \Phi(t_i,t_{i-1}) & \Psi(t_i,t_{i-1}) \\ 0 & I \end{bmatrix}^T$$

$$+ \Lambda(t_i,t_{i-1})$$

$$\Lambda(t_i,t_{i-1}) = Q \cdot (t_i - t_{i-1})$$

8. Complete the update phase of the filter.

Calculate the gain $K_i = \dfrac{P_i^{i-1} H_i^T}{(H_i P_i^{i-1} H_i^T + R)}$

update the state $\underline{\Delta z}_i^{\hat{}\,i} = \underline{\Delta z}_i^{\hat{}\,i-1} + K_i [\Delta y(t_i) - H_i \underline{\Delta z}_i^{\hat{}\,i-1}]$

update the covariance $P_i^i = (I - K_i H_i) P_i^{i-1}$

9. Interpolate for the transition matrix inverse and save for next observation

$$\Phi_s = \Phi^{-1}(t_i,t_0) \quad \text{and}$$

$$\Psi_s = \Psi(t_i,t_0)$$

The SKF continues with step one until the integration grid boundary is crossed; then the integration grid algorithm is repeated. When $t_i = t_{i-1}$, only steps 1, 5, 7 and 8

must be executed. Since the SKF does not update the nominal trajectory within the integration grid, the solve vector corrections estimated by the filter can become large enough to cause filter divergence due to model nonlinearities. This tendency is reduced for the ESKF algorithm presented next.

3.3 ESKF Design

The ESKF is motivated by the desire to reduce the impact of observation nonlinearities, and is allowed by the approximately linear nature of the Semianalytical dynamics. The mean elements obey the equation of motion (2-9)'

$$\dot{\bar{\underline{a}}} = \bar{n}\, \underline{e}_6 + \varepsilon\, \underline{A}(\bar{\underline{a}}) \; ; \; \bar{\underline{a}}(t_0) = \bar{\underline{a}} \qquad (3\text{-}2)$$

Thus, to zeroth order

$$\bar{\underline{a}}(t) = \bar{n}\, \underline{e}_6\, \Delta t + \bar{\underline{a}}_0 \qquad (3\text{-}3)$$

The zeroth order state partials are

$$\frac{\partial \bar{\underline{a}}(t)}{\partial \bar{\underline{a}}_0} = I + \underline{e}_6\, \underline{e}_1^T\, \frac{\bar{n}}{\bar{a}}\, \Delta t \qquad (3\text{-}4)$$

The mean motion, $\bar{n}$, is small for most satellites. The semimajor axis, $\bar{a}$, further attenuates the second term, so, especially for small time differences Δt, the mean equinoctial elements $\underline{\bar{a}}(t)$ exhibit linear behavior. Now if equation (3-2) is linear, then the estimate $\underline{\bar{a}}(t_k)$ is propagated optimally by either the original KF prediction equations or the LKF prediction equations. That is, optimal prediction, analogous to EKF prediction, is accomplished by the LKF prediction equations.

This argument can be made more explicit as follows. Let $\underline{z}_N(t_{i-1})$ be the a priori nominal state at time t_{i-1} and let $\Delta\hat{\underline{z}}_{i-1}^{i-1}$ be the Kalman Filter correction after a measurement at time t_{i-1}. An EKF would use the new state

$$\underline{\bar{z}}(t_{i-1}) = \underline{z}_N(t_{i-1}) + \Delta\hat{\underline{z}}_{i-1}^{i-1} \tag{3-5}$$

as the initial condition for the state propagation equations and a corresponding relinearization of the filter equations. When the dynamics are linear, this new initial condition results in a predicted state at time t_i

$$\hat{\underline{z}}_i^i = \underline{\bar{z}}(t_i) = \Phi(t_i,t_{i-1})\ \underline{\bar{z}}(t_{i-1}) \tag{3-6}$$

Substitution of (3-5) and use of the notational definitions gives

$$\hat{\underline{z}}_i = \Phi(t_i,t_{i-1})\ \underline{z}_N(t_{i-1}) + \Phi(t_i,t_{i-1})\ \Delta\hat{\underline{z}}_{i-1}$$

$$= \underline{z}_N(t_i) + \Delta\hat{\underline{z}}_i^{i-1} \qquad (3\text{-}7)$$

Equation (3-7) states the desired result explicitly: optimal EKF prediction can be accomplished by adding the LKF-predicted filter correction to the nominal trajectory when the dynamics are linear.

The ESKF design assumes that the semianalytical dynamics (3-2) are linear. This assumption is investigated in Section 3.4 below. The above argument indicates that the only application of EKF concepts lies in the measurement update computations. The measurement linearization matrix H_K is computed based on the nominal trajectory; the predicted observation, however, is based on the state predicted by (3-7). Computation of an observation based on the mean equinoctial elements generated by the Semianalytical integrator requires three transformations:

1. computation of short periodic functions and osculating equinoctial elements;

2. computation of the osculating position and velocity; and

3. computation of the resulting observation.

The state prediction in Equation (3-7) is implemented in mean equinoctial elements. The resulting observation computation can be written

$$\hat{\underline{y}}_i = h[\underline{x}(\bar{\underline{a}}_N(t_i) + \Delta\hat{\bar{\underline{a}}}_i^{i-1} + \varepsilon\underline{n}(\bar{\underline{a}}_N(t_i) + \Delta\hat{\bar{\underline{a}}}_i^{i-1}))] \quad (3\text{-}8)$$

Clearly exact application of EKF predicted observation concepts requires explicit recomputation of the short periodic functions, precluding the use of either the coefficient or position and velocity interpolators. More efficient implementations of (3-8) allowing use of these interpolators can be obtained by successive linearization of the arguments of $\underline{h}(\underline{x})$. For use with just the short periodic coefficient interpolator, the following computations are optimal for accuracy and efficiency.

$$\text{(i)} \quad \hat{\underline{a}}_i = \bar{\underline{a}}_N(t_i) + (I + B_1)\,\Delta\hat{\bar{\underline{a}}}_i^{i-1} + \varepsilon\underline{n}(\bar{\underline{a}}_N(t_i))$$

$$\text{(ii)} \quad \hat{\underline{x}}_i = \underline{x}(\hat{\underline{a}}_i) \quad (3\text{-}9)$$

$$\text{(iii)} \quad \hat{\underline{y}}_i = h(\hat{\underline{x}}_i)$$

Recall that the B_1 matrix is defined in (2-33) as the partial of the short periodics with respect to the mean elements. When the position and velocity short arc interpolator is used, the following computations implement the ESKF predicted observation calculation.

$$
\begin{aligned}
&\text{(i)} \quad \underline{a}_N(t_i) = \bar{\underline{a}}_N(t_i) + \varepsilon \underline{n}(\bar{\underline{a}}_N(t_i)) \\
&\text{(ii)} \quad \underline{x}_N(t_i) = \underline{x}(\underline{a}_N(t_i)) \\
&\text{(iii)} \quad \hat{\underline{x}}_i = \underline{x}_N(t_i) + \frac{\partial \underline{x}(\underline{a}_N)}{\partial \underline{a}_N} [I + B_1] \Delta \hat{\bar{\underline{a}}}_i^{i-1} \\
&\text{(iv)} \quad \hat{y}_i = h(\hat{x}_i)
\end{aligned}
\tag{3-10}
$$

Green [13] proposed using (3-9) (i) and (ii) for generating the filter's state history output, but not for use in computing the predicted observation. Green's semianalytical estimation algorithm is quite similar to the SKF. An algorithmic flow for the ESKF employing equations (3-9) follows; an algorithm using (3-10) is quite similar.

3.3.1 Operations on the Integration Grid

These operations are identical to those for the SKF, due to the use of the assumed linearity of the Semianalytic dynamics.

3.3.2 Operations on the Observation Grid

The ESKF performs the following steps in processing a new observation.

1. Obtain the new observation, $y(t_i)$, at time $t = t_i$

2. Interpolate for $\bar{\underline{a}}_N(t_i)$, $\Phi(t_i,t_0)$, $\Psi(t_i,t_0)$

we already have $\Phi^{-1}(t_{i-1},t_0)$ in Φ_s

3. Interpolate for short periodic coefficients

$$\underline{\varepsilon C}_\sigma(\bar{\underline{a}}_N(t_i)),\quad \underline{\varepsilon D}_\sigma(\bar{\underline{a}}_N(t_i))$$

compute the short periodic functions

$$\underline{\varepsilon\eta}(\bar{\underline{a}}_N) = \sum_{\sigma=1}^{N} \underline{\varepsilon C}_\sigma \sin \sigma\bar{\lambda} - \underline{\varepsilon D}_\sigma \cos \sigma\bar{\lambda}$$

4. Compute the transition matrices

$$\Phi(t_i,t_{i-1}) = \Phi(t_i,t_0)\ \Phi_s$$

$$\Psi(t_i,t_{i-1}) = \Psi(t_i,t_0) - \Phi(t_i,t_{i-1})\ \Psi_s$$

5. Predict the filter corrections

$$\hat{\Delta\bar{\underline{a}}}_i^{i-1} = \Phi(t_i,t_{i-1})\ \hat{\Delta\bar{\underline{a}}}_{i-1}^{i-1} + \Psi(t_i,t_{i-1})\ \hat{\Delta\underline{c}}_{i-1}^{i-1}$$

$$\hat{\Delta\underline{c}}_i^{i-1} = \hat{\Delta\underline{c}}_{i-1}^{i-1}$$

6. Compute the predicted osculating elements

$$\hat{\underline{a}}(t_i) = \bar{\underline{a}}_N(t_i) + \hat{\Delta\bar{\underline{a}}}_i^{i-1} + \underline{\varepsilon\eta}(\bar{\underline{a}}_N) + B_1\ \hat{\Delta\bar{\underline{a}}}_i^{i-1}$$

transform to cartesian elements $\hat{\underline{x}}(t_i)$

7. Compute the predicted observation

$$\hat{y}(t_i) = h(\hat{\underline{x}}(t_i), t_i)$$

and the observation residual

$$\Delta y(t_i) = y(t_i) - \hat{y}(t_i)$$

compute the observation partials

$$H_i = \frac{\partial h}{\partial \underline{z}_N}(\underline{z}_N, t_i) = \frac{\partial h}{\partial \underline{a}_N}\left[I + B_1 \mid B_4\right]$$

$$B_1 = \frac{\partial \underline{\epsilon\eta}_1(\bar{\underline{a}}_N)}{\partial \bar{\underline{a}}_N}$$

$$B_4 = \frac{\partial \underline{\epsilon\eta}_1(\bar{\underline{a}}_N)}{\partial \underline{c}}$$

8. Predict the filter covariance

$$P_i^{i-1} = \begin{bmatrix} \Phi(t_i, t_{i-1}) & \Psi(t_i, t_{i-1}) \\ 0 & I \end{bmatrix} P_{i-1}^{i-1} \begin{bmatrix} \Phi(t_i, t_{i-1}) & \Psi(t_i, t_{i-1}) \\ 0 & I \end{bmatrix}^T$$

$$+ \Lambda(t_i, t_{i-1})$$

$$\Lambda(t_i, t_{i-1}) = Q \cdot (t_i - t_{i-1})$$

9. Complete the update phase of the filter.

Calculate the gain $K_i = \dfrac{P_i^{i-1} H_i^T}{(H_i P_i^{i-1} H_i^T + R)}$

update the state $\hat{\Delta z}_i^i = \hat{\Delta z}_i^{i-1} + K_i \Delta y(t_i)$

update the covariance $P_i^i = (I - K_i H_i)\ P_i^{i-1}$

10. Interpolate for the transition matrix and inverse and save for next observation

$$\Phi_s = \Phi^{-1}(t_i, t_0)$$

$$\Psi_s = \Psi(t_i, t_0)$$

The ESKF continues with step 1 until all observations have been processed or the integration grid boundary is crossed. When the boundary is crossed, processing continues as indicated previously. When two observations come at the same time, $t_i = t_{i-1}$, then only steps 1, 6, 7, and 9 must be executed for the second observation.

3.4 Verification of SKF and ESKF Design Assumptions

Several assumptions have been made in the design of the SKF and ESKF algorithms. One not commented on previously is the computation of the process noise contribution to the predicted covariance (see SKF, step 7, and ESKF, step 8). The process noise term is assumed to grow linearly in time. This assumption and the nonlinearities in the observation and dynamics models are tested below.

3.4.1 The Process Noise Test

The SKF and ESKF model the process noise contribution to the predicted covariance as being linear in time. This follows the assumption used in the Goddard Trajectory

Determination System, Research and Development version (RD GTDS) software [3], which served as the testbed for SKF and ESKF development. The equation for Kalman Filter covariance prediction (2-60) derives the process noise term as

$$\Lambda(t,t_0) = \int_{t_0}^{t} \Phi(t,\tau)\, Q(\tau)\, \Phi^T(t,\tau)\, d\tau \qquad (3\text{-}11)$$

where Q(t) is the process noise strength at time t

$$E\{\underline{w}(t)\, \underline{w}^T(\tau)\} = Q(t)\, \delta(t - \tau) \qquad (3\text{-}12)$$

and $\Phi(t,\tau)$ is the system state transition matrix. If Q(t) is a constant matrix and $\Phi(t,\tau)$ is the identity matrix, then equation (3-11) reduces to the GTDS assumption

$$\Lambda(t,t_0) = Q \cdot (t - t_0) \qquad (3\text{-}13)$$

Shaver [30] computed the state transition matrix for mean equinoctial elements explicitly, including two body and oblateness effects. His state transition matrix has the form

$$\Phi(t,t_0) \simeq A(t,t_0) + \varepsilon B(t,t_0) \qquad (3\text{-}14)$$

The matrix A has order 1 constant and sinusoidal elements; the matrix εB has a secular growth in $(t-t_0)$. Equation (3-14) leads to a process noise covariance form

$$\Lambda(t,t_0) \approx C_1(t - t_0) + \varepsilon C_2(t - t_0)^2 + \ldots \quad (3\text{-}15)$$

This result validates the GTDS approach for small $(t-t_0)$. Equation (3-13) was verified by numerical test for large time intervals using the low altitude satellite described below. The state transition matrix included J_2 and drag. The exact equation (3-11) was integrated by the trapezoidal rule, so quadratic terms in $\Lambda(t,t_0)$ were exactly computed. The value used for Q is shown in Table 3-1 as is the value of $\Lambda(t,t_0)$ after 16 hours. Clearly the main diagonal terms behave linearly in time; notice, however, that the model (3-13) does not account for cross correlations that develop in the exact equation (3-11). In actual filter tests, the model (3-13) has performed adequately. Observe that the same methodologies apply for choosing the process noise strength, Q, under both (3-11) and (3-13).

3.4.2 Evalution of Dynamical Nonlinearities

The Second Order Gaussian Equations specify bias correction terms for the dynamics and measurement models. The filter prediction equation is

Table 3-1

Process Noise Covariance Test Results

satellite: WNMTST (see Table 4-3)

process noise strength

$$Q = \text{diag}\left[10^{-10}, 10^{-16}, 10^{-16}, 10^{-17}, 10^{-17}, 10^{-13}, 10^{-8}\right]$$

process noise covariance contribution

at time t = 16 hours = 57600. seconds

$$\Lambda(t,0) = \begin{bmatrix} 0.58D\text{-}05 & 0.13D\text{-}10 & -0.81D\text{-}10 & 0.14D\text{-}10 & -0.14D\text{-}10 & -0.38D\text{-}07 & 0.0 \\ 0.13D\text{-}10 & 0.56D\text{-}11 & 0.13D\text{-}14 & -0.41D\text{-}15 & -0.22D\text{-}14 & -0.58D\text{-}13 & 0.0 \\ -0.81D\text{-}10 & 0.13D\text{-}14 & 0.57D\text{-}11 & -0.60D\text{-}14 & 0.58D\text{-}14 & 0.31D\text{-}12 & 0.0 \\ 0.14D\text{-}10 & -0.41D\text{-}15 & -0.60D\text{-}14 & 0.60D\text{-}12 & -0.82D\text{-}15 & -0.15D\text{-}12 & 0.0 \\ -0.14D\text{-}10 & -0.22D\text{-}14 & 0.58D\text{-}14 & -0.82D\text{-}15 & 0.55D\text{-}12 & 0.91D\text{-}13 & 0.0 \\ -0.38D\text{-}07 & -0.58D\text{-}13 & 0.31D\text{-}12 & -0.15D\text{-}12 & 0.91D\text{-}13 & 0.61D\text{-}08 & 0.0 \\ 0.0 & 0.0 & 0.0 & 0.0 & 0.0 & 0.0 & 0.58D\text{-}03 \end{bmatrix}$$

Note: $\underline{z} = \begin{bmatrix} \bar{a} \\ C_D \end{bmatrix}$ so that Drag process noise is included. The value of Q is similar to those employed in test cases below. Notice the strong correlation between a and λ, predictable from equation (3-4).

$$\Delta\dot{\underline{z}}(t) = F(t)\ \Delta\underline{z}(t) + \underline{b} \qquad (3\text{-}16)$$

where the vector $\underline{b}$ accounts for the dynamical nonlinearities causing a bias in the filter estimate; the ith component of $\underline{b}$ is given by

$$b_i = \frac{1}{2}\ tr\left\{\frac{\partial^2 f_i}{\partial \underline{z}^2}_N P\right\} \qquad (3\text{-}17)$$

The other terms in equations (3-16) and (3-17) are defined by

$\Delta\underline{z}$ = estimated filter solve vector

f_i = ith component of $\underline{f}(z,t)$

$\underline{f}(\underline{z},t)$ = system dynamics force model

$\underline{z}_N$ = nominal system state

$$F(t) = \frac{\partial \underline{f}(\underline{z},t)}{\partial \underline{z}}\Bigg|_{\underline{z} = \underline{z}_N}$$

P = covariance matrix of $\Delta\underline{z}$

The bias correction vector provides an increment to the filter estimate $\Delta\underline{z}$ given by

$$\delta\underline{z}(t) = \int_{t_0}^{t} \Phi(t,\tau)\, \underline{b}(\tau)\, d\tau \qquad (3\text{-}18)$$

The matrix Φ is the system state transition matrix. Equation (3-18) was integrated by Euler's method for 11 hours; the variational equation force model included the oblateness effects. The matrix F(t) was computed analytically. Second partials of the force model were computed by finite differencing F(t); the accuracy of the numerical derivatives was verified by the equality of off-diagonal terms, i.e.

$$\frac{\partial^2 f_i}{\partial z_m \partial z_n} = \frac{\partial^2 f_i}{\partial z_n \partial z_m} \qquad (3\text{-}19)$$

indicating that the analytical and finite differenced partials had the same accuracy. The results are shown in Table 3-2. The perturbation $\delta\underline{z}$ had fairly regular growth in time, finally reaching the value shown after 11 hours. Since magnitude of the $\delta\underline{z}$ correction is much smaller than typical filtering corrections, it is concluded that the dynamical nonlinearities have negligible impact. This conclusion supports the design assumptions of the ESKF.

Table 3-2

Results of the Dynamical Nonlinearity Test

satellite: WNMTST (see Table 4-3)

state covariance:

$$P_0 = \text{diag}\,[10^{-6}, 10^{-12}, 10^{-12}, 10^{-12}, 10^{-12}, 10^{-10}]$$

Nonlinearity bias correction:

at time t = 11 hours

$$\underline{\delta z}(t) = \left[\begin{array}{cccccc} -0.126D\text{-}03 & 0.134D\text{-}16 & -0.167D\text{-}14 & -0.725D\text{-}15 & 0.772D\text{-}15 & 0.258D\text{-}12 \end{array}\right]$$

Note: $\underline{P}_o$ implies

$$\underline{\Delta z} \approx [10^{-3}, 10^{-6}, 10^{-6}, 10^{-6}, 10^{-6}, 10^{-5}]^T ;$$

clearly $\Delta z_i >> \delta z_i$. These results are linear in $\underline{P}_o$, implying validity for all scalings of $\underline{P}_o$.

3.4.3 Evaluation of Measurement Nonlinearities

The analysis of observation model nonlinarities is essential to the design of the ESKF. Any nonlinearities in the observation model result directly in filter biases. The Second Order Gaussian Filter update equations approximate this bias as

$$c = \frac{1}{2} \operatorname{tr}\{\frac{\partial^2 y}{\partial \underline{z}_N^2} P\} \tag{3-20}$$

where c is the bias, y is the observation, $\underline{z}_N$ is the nominal filter state, and P is the filter covariance. This bias can be expanded explicitly in terms of the computational method used by Semianalytical Satellite Theory for obtaining predicted observations.

Semianalytical Satellite theory computes an observation by the following sequence of calculations

$$\text{(i)} \quad \underline{a} = \bar{\underline{a}} + \varepsilon \underline{\eta}(\bar{\underline{a}})$$

$$\text{(ii)} \quad \underline{x} = T(\underline{a}) \quad ; \quad \underline{x} = \begin{bmatrix} \underline{r} \\ \underline{v} \end{bmatrix}$$

$$\text{(iii)} \quad \underline{x}_{LT} = D\,\underline{x} - \underline{R} \; ; \; \underline{x}_{LT} = \begin{bmatrix} \underline{r}_{LT} \\ \underline{v}_{LT} \end{bmatrix}$$

$$\text{(iv)} \quad y = h(\underline{x}_{LT})$$

The transformation in (iii) accounts for the transformation from inertial position and velocity, $\underline{x}$ (in 1950 coordinates), to earth-fixed coordinates, and from there to the local tangent frame at the observation station location, $\underline{R}$. The transformations (i) and (ii) have been discussed above; the observation model (iv) depends on the current observation type.

First and second partials of the observation model can be computed by application of the chain rule to transformations (i) - (iv). The second order partials are desired for analysis of the bias correction term (3-20). Three terms will arise naturally in the chain rule expansion of the second order partials; the terms will contain the second partials of one of the nonlinear transformations (i), (ii), or (iv). The transformation (iii) is linear, so has vanishing second partials. Writing

$$c = \frac{1}{2} \operatorname{tr}\{(A + B + C)\underline{P}\} \tag{3-21}$$

the three terms A, B, and C become

$$A = \left[D\left(\frac{\partial \underline{x}}{\partial \underline{a}}\right)(I + B_1)\right]^T \frac{\partial^2 y}{\partial \underline{x}_{LT}^2} \left[D\left(\frac{\partial \underline{x}}{\partial \underline{a}}\right)(I + B_1)\right] \tag{3-22}$$

$$B = \frac{\partial y}{\partial \underline{x}_{LT}} D\left[\frac{\partial^2 \underline{x}}{\partial \underline{a}^2}\right] : (I + B_1) : (I + B_1) \tag{3-23}$$

$$C = \frac{\partial \underline{y}}{\partial \underline{x}_{LT}} D \frac{\partial \underline{x}}{\partial \underline{a}} \frac{\partial B_1}{\partial \underline{a}} \qquad (3\text{-}24)$$

The quantity $\partial^2 \underline{x}/\partial \underline{a}^2$ is a third order tensor; the two multiplications by $(I + B_1)$ result from the application of the chain rule in each of the partials with respect to $\underline{a}$. The quantity $\partial B_1/\partial \underline{a}$ is similarly third order.

The relative magnitudes of the three terms A, B, and C were evaluated in a station pass assuming range observations were taken. Analytical implementations already existed in the Semianalytical Satellite Theory in the CSDL version of RD GTDS for the equinoctial-to-cartesian partials, the D matrix, the J_2-short periodic partials (B_1 matrix), and the range obs partials. Analytical second order range partials were implemented. Only the second order partials in B and C remained to be implemented; they were implemented by finite differences operating on the first order analytic partials. Accuracy was verified by the equality of off-diagonal terms. Table 3-3 gives two printouts of the A, B, and C matrices and their sum T; the first printout is at the start of the pass, the second is at the middle. These printouts show that A and B usually have the same order of magnitude; C is several orders of magnitude smaller than A or B and so can be neglected. Thus an extended-type algorithm should include the nonlinear effects due to the observation type and the equinoctial-to-cartesian element transformation but can neglect nonlinearities in the short periodics. One will expect an ESKF algorithm employing (3-9) to perform better than an algorithm using (3-10).

Table 3-3

Results of the Observation Nonlinearity Test

satellite: WNMTST (see Table 4-3)

station: MALABO
height -4.0 (km)
latitude 23° 1' 12"
longitude 279° 18' 50.4"

station pass interval 03:46:00.0 to 03:56:00.0

observation type: range

```
**********************************************************************************
DATE   JUNE  8, 1979    3HRS    46MINS     6.379SECS  (JULIAN DATE = 2444032.6570)
ELAPSED TIME FROM EPOCH =    0 DAYS    0 HRS     2 MINS     0.000 SECS
FLIGHT CENTRAL BODY IS EARTH


1 1 A, B, C, T =    0.29686D-03    0.90076D-07    0.29792D-07    0.29698D-03
1 2 A, B, C, T =    0.27434D+01   -0.56327D+00    0.21417D-02    0.21822D+01
1 3 A, B, C, T =   -0.27774D+00    0.15515D+01   -0.58208D-03    0.12731D+01
1 4 A, B, C, T =    0.43601D+00   -0.35249D+00   -0.17951D-03    0.83333D-01
1 5 A, B, C, T =   -0.35314D+00    0.28674D+00   -0.46305D-04   -0.66453D-01
1 6 A, B, C, T =    0.85239D+00   -0.78716D+00   -0.13383D-02    0.63884D-01
2 1 A, B, C, T =    0.27434D+01   -0.56327D+00    0.21417D-02    0.21822D+01
2 2 A, B, C, T =    0.30409D+05    0.45815D+03    0.0            0.30867D+05
2 3 A, B, C, T =   -0.93771D+04    0.20354D+04    0.0           -0.73416D+04
2 4 A, B, C, T =    0.11809D+05   -0.68729D+04   -0.11615D+02    0.49246D+04
2 5 A, B, C, T =   -0.12191D+05    0.24895D+04   -0.31671D+01   -0.97044D+04
2 6 A, B, C, T =    0.12034D+05    0.26453D+04   -0.22426D+01    0.14677D+05
3 1 A, B, C, T =   -0.27774D+00    0.15515D+01   -0.58208D-03    0.12731D+01
3 2 A, B, C, T =   -0.93771D+04    0.20354D+04    0.0           -0.73416D+04
3 3 A, B, C, T =    0.94314D+04   -0.65575D+04    0.0            0.28739D+04
3 4 A, B, C, T =   -0.10885D+05    0.52039D+04    0.15331D+02   -0.56657D+04
3 5 A, B, C, T =    0.12353D+05   -0.47529D+02    0.39168D+01    0.12309D+05
3 6 A, B, C, T =   -0.63957D+04    0.57419D+04    0.35563D+02   -0.61822D+03
4 1 A, B, C, T =    0.43601D+00   -0.35249D+00   -0.17951D-03    0.83333D-01
4 2 A, B, C, T =    0.11809D+05   -0.68729D+04   -0.11615D+02    0.49246D+04
4 3 A, B, C, T =   -0.10885D+05    0.52039D+04    0.15331D+02   -0.56657D+04
4 4 A, B, C, T =    0.12609D+05   -0.78083D+04   -0.12843D+02    0.47876D+04
4 5 A, B, C, T =   -0.14252D+05    0.33203D+04   -0.16251D+01   -0.10933D+05
4 6 A, B, C, T =    0.76470D+04   -0.39844D+04   -0.12911D+02    0.36497D+04
5 1 A, B, C, T =   -0.35314D+00    0.28674D+00   -0.46305D-04   -0.66453D-01
5 2 A, B, C, T =   -0.12191D+05    0.24895D+04   -0.31671D+01   -0.97044D+04
5 3 A, B, C, T =    0.12353D+05   -0.47529D+02    0.39168D+01    0.12309D+05
5 4 A, B, C, T =   -0.14252D+05    0.33203D+04   -0.16251D+01   -0.10933D+05
5 5 A, B, C, T =    0.16179D+05    0.13603D+04   -0.47395D+00    0.17539D+05
5 6 A, B, C, T =   -0.83522D+04    0.68918D+03    0.38840D+01   -0.76591D+04
6 1 A, B, C, T =    0.85239D+00   -0.78716D+00   -0.13383D-02    0.63884D-01
6 2 A, B, C, T =    0.12034D+05    0.26453D+04   -0.22426D+01    0.14677D+05
6 3 A, B, C, T =   -0.63957D+04    0.57419D+04    0.35563D+02   -0.61822D+03
6 4 A, B, C, T =    0.76470D+04   -0.39844D+04   -0.12911D+02    0.36497D+04
6 5 A, B, C, T =   -0.83522D+04    0.68918D+03    0.38840D+01   -0.76591D+04
6 6 A, B, C, T =    0.58645D+04   -0.31301D+04   -0.22752D+02    0.27117D+04
```

```
**********************************************************************************************
DATE   JUNE  8, 1979  3HRS    51MINS     6.379SECS  (JULIAN DATE = 2444032.6605)
ELAPSED TIME FROM EPOCH =    0 DAYS     0 HRS      7 MINS      0.000 SECS
FLIGHT CENTRAL BODY IS EARTH


1 1 A, B, C, T =    0.47344D-03   -0.51138D-07    0.17688D-06    0.47356D-03
1 2 A, B, C, T =    0.33541D+01    0.41502D+00    0.21231D-03    0.37794D+01
1 3 A, B, C, T =    0.33240D+00    0.51436D+00   -0.17738D-02    0.84499D+00
1 4 A, B, C, T =   -0.34728D+00    0.13163D+00   -0.37617D-03   -0.21603D+00
1 5 A, B, C, T =    0.14505D+01   -0.54619D+00    0.68648D-03    0.90498D+00
1 6 A, B, C, T =    0.26513D+00   -0.19353D+00   -0.12860D-02    0.70315D-01
2 1 A, B, C, T =    0.33641D+01    0.41502D+00    0.21231D-03    0.37794D+01
2 2 A, B, C, T =    0.36618D+05   -0.38230D+03    0.0            0.36236D+05
2 3 A, B, C, T =   -0.35923D+05    0.17402D+04    0.0           -0.34082D+05
2 4 A, B, C, T =    0.13155D+05   -0.38052D+04    0.28024D+01    0.93523D+04
2 5 A, B, C, T =   -0.71647D+04   -0.29369D+04   -0.14688D+01   -0.10103D+05
2 6 A, B, C, T =    0.21797D+05    0.51528D+02    0.68982D+01    0.21855D+05
3 1 A, B, C, T =    0.33240D+00    0.51436D+00   -0.17738D-02    0.84499D+00
3 2 A, B, C, T =   -0.35823D+05    0.17402D+04    0.0           -0.34082D+05
3 3 A, B, C, T =    0.11492D+06   -0.72760D+04    0.0            0.10764D+06
3 4 A, B, C, T =   -0.47165D+05    0.14303D+05    0.53273D+01   -0.32856D+05
3 5 A, B, C, T =    0.53494D+05   -0.31861D+04   -0.19475D+01    0.50306D+05
3 6 A, B, C, T =   -0.59622D+05    0.40269D+04    0.83306D+00   -0.55594D+05
4 1 A, B, C, T =   -0.34728D+00    0.13163D+00   -0.37617D-03   -0.21603D+00
4 2 A, B, C, T =    0.13155D+05   -0.38052D+04    0.28024D+01    0.93523D+04
4 3 A, B, C, T =   -0.47165D+05    0.14303D+05    0.53273D+01   -0.32856D+05
4 4 A, B, C, T =    0.19452D+05   -0.52793D+04   -0.95117D+01    0.14163D+05
4 5 A, B, C, T =   -0.22533D+05    0.32226D+04   -0.36945D+01   -0.19314D+05
4 6 A, B, C, T =    0.24275D+05   -0.73390D+04   -0.89310D+01    0.16928D+05
5 1 A, B, C, T =    0.14505D+01   -0.54619D+00    0.68648D-03    0.90498D+00
5 2 A, B, C, T =   -0.71647D+04   -0.29369D+04   -0.14688D+01   -0.10103D+05
5 3 A, B, C, T =    0.53494D+05   -0.31861D+04   -0.19475D+01    0.50306D+05
5 4 A, B, C, T =   -0.22533D+05    0.32226D+04   -0.36945D+01   -0.19314D+05
5 5 A, B, C, T =    0.28454D+05   -0.56649D+04   -0.28009D+00    0.22789D+05
5 6 A, B, C, T =   -0.26553D+05    0.11571D+04   -0.13156D+01   -0.25397D+05
6 1 A, B, C, T =    0.26513D+00   -0.19353D+00   -0.12860D-02    0.70315D-01
6 2 A, B, C, T =    0.21797D+05    0.51528D+02    0.68982D+01    0.21855D+05
6 3 A, B, C, T =   -0.59622D+05    0.40269D+04    0.83306D+00   -0.55594D+05
6 4 A, B, C, T =    0.24275D+05   -0.73390D+04   -0.89310D+01    0.16928D+05
6 5 A, B, C, T =   -0.26553D+05    0.11571D+04   -0.13156D+01   -0.25397D+05
6 6 A, B, C, T =    0.31339D+05   -0.38226D+04   -0.11940D+02    0.27503D+05
```

3.5 Summary

This chapter presented the design of two sequential semianalytical orbit determination algorithms, the SKF and the ESKF. Preliminary numerical tests verified the assumptions made. The next chapter presents results from simulation test cases.

Chapter 4
SIMULATION TEST CASES

This chapter discusses the results from two simulated-data test cases. The Semianalytical Kalman Filter (SKF) and Extended Semianalytical Kalman Filter (ESKF) designed in this thesis are compared with the Linearized Kalman Filter (LKF) and Extended Kalman Filter (EKF) previously implemented in the Research and Development version of the Goddard Trajectory Determination System (RD GTDS). All filters are compared against the performance baselines provided by the application of batch estimation algorithms to the same observational data.

The question of test uniformity is fundamental to performance comparisons between different filters. The validity of performance comparisons can be questioned on two bases:

1. The estimation problem is stochastically formulated, meaning that all results are randomly distributed; Monte Carlo testing is usually required to achieve a high degree of confidence in the results.

2. The particular filters compared here estimate intrinsically different quantities; the SKF and ESKF estimate mean equinoctial elements, while the LKF and EKF estimate osculating position and velocity. Thus different input parameters are required by the different filter types. The impact of any resulting changes in performance must be carefully addressed.

The section on test case philosophy below addresses this question in detail. The two test cases are then discussed, with important points summarized at the end of the chapter.

4.1 Test Case Philosophy

The RD GTDS software package provides a natural structure for implementing the simulated-data test cases discussed in this chapter. This package has five basic capabilities important for this discussion.

1. EPHEM: The EPHEM program allows the propagation of an ephemeris from a given set of initial conditions, using one of a large variety of satellite theories and force models. The capabilities for high precision Cowell numerical integration and semianalytical ephemeris propagation are important here.

2. DATASIM: The DATASIM program can simulate a wide variety of observation types from a specified tracking station network. The capability to simulate range, range-rate, azimuth, and elevation observations from a C-band tracking station network, with random errors included, was used here.

3. EARLYORB: The EARLYORB program provides initial estimates of a satellite orbit using just a few observation sets. The algorithms used are similar to Gauss' method; typical errors are on the order of 50 kilometers in the initial position and velocity.

4. DC and FILTER: RD GTDS implements both batch differential corrections (DC) estimators and sequential filtering algorithms (FILTER). Both capabilities have been extended to allow the use of Semianalytical Satellite Theory as the ephemeris generator. The resulting DC algorithm is called the Semianalytical DC (SDC). The DC algorithm employing the special perturbations high precision numerical integrator is called the Cowell DC (CDC). The FILTER algorithm abbreviations are defined above.

5. COMPARE: The COMPARE program allows the point-by-point comparison of the time histories of two ephemerides. The comparison of an estimated ephemeris with the simulation truth ephemeris provides a measure of estimator accuracy.

Each simulated-data test case required defining a truth ephemeris, simulating C-band observations, and processing the observations with the various filters. The first test case was directed primarily toward software verification and included only these steps. The second test case investigated input parameter selection and performance for a difficult filter convergence problem; the EARLYORB program was used to provide the initial orbital estimate, while DC runs and the COMPARE program gave performance baselines and performance measures, respectively. The EPHEM program with the Cowell integrator was used to generate the truth ephemeris -- high precision Cowell integration provides a generally accepted high accuracy standard for ephemeris prediction.

Valid performance comparisons can be achieved either by comparing estimator performances for corresponding input parameter choices, or by comparing the optimal performance of each algorithm over all possible choices of the input parameters. Both of these approaches are used within this chapter. The input parameters to be selected are the initial orbital elements, the a priori covariance of these elements, the process noise model, and the force model used in the equations of motion and the variational equations.

The CDC, LKF, and EKF all estimate the osculating position and velocity. These estimators can be initialized with the Cowell truth initial elements for software validation tests, or with the EARLYORB elements when initial errors are desired. The SDC, SKF, and ESKF, on the other hand, all estimate mean equinoctial elements. The mean equinoctial elements corresponding to a given osculating initial position and velocity can be obtained in two ways.

1. A Precise Conversion of Elements (PCE) procedure consists of solving for epoch mean elements with a SDC, using exact osculating position and velocity measurements taken at a uniformly high data rate as the input observations. An EPHEM run using the high precision Cowell integrator is required to generate the position and velocity measurements. This initialization procedure has been used before with excellent results [12], [13], [18]. It gives highly accurate mean elements, especially appropriate for generating a Semianalytical truth ephemeris corresponding to the simulation Cowell truth ephemeris.

2. An Epoch Point Conversion (EPC) procedure inverts the near identity transformation (2-6) relating the mean and osculating equinoctial elements. Walter [31] proved that the near identity transformation is a contraction mapping, ensuring the convergence of the successive substitutions iteration

$$\underline{\bar{a}}_{k+1} = \underline{a} - \epsilon \underline{\eta}(\underline{\bar{a}}_k) \qquad (4\text{-}1)$$

This iteration has been programmed using Zeis' [16] explicit J_2-short periodic expressions, which are zeroth order in the eccentricity. The converged mean elements cannot be expected to be highly accurate, due to the short periodic model truncation. They are adequate, however, for the conversion of osculating EARLYORB elements to corresponding mean initial elements.

When corresponding mean equinoctial and osculating position and velocity initial covariances are desired, the usual transformation equation for covariance applies. The result is

$$\underline{P}_x(t_o) = \left[\frac{\partial \underline{x}(t_o)}{\partial \underline{\bar{a}}(t_o)}\right] \underline{P}_a(t_o) \left[\frac{\partial \underline{x}(t_o)}{\partial \underline{\bar{a}}(t_o)}\right]^T \qquad (4\text{-}2)$$

Here $\underline{P}_x$ and $\underline{P}_a$ are the initial osculating position and velocity covariance matrix and mean equinoctial covariance matrix, respectively. The required partial derivatives are discussed in Section 2.4. Corresponding process noise covariances can be obtained in a similar fashion, as discussed in Appendix A.

Highly accurate orbit determination usually requires as complete a force model for the equations of motion as possible. Semianalytical Satellite Theory allows great flexibility in force model truncations without accuracy loss, based on order-of-magnitude considerations. Truncation decisions are typically based on assumptions like the small eccentricity approximation, fourier series coefficient attenuation, and perturbation magnitude. When the performance impact of force model truncations is assessed, only the technical description of the force models is given. Consult the references [13], [15], [18], [19] for further clarification. May [32] investigated the variational equation force model accuracy necessary for good DC convergence. Any variational equation force model simplification achievable is highly desirable, since the number of variational derivatives (36) makes their integration quite costly. She found that inclusion of the J_2 perturbation was usually sufficient for good convergence and accuracy. The filter tests here use only the J_2 and drag perturbations in the variational equations; the validity of this model is confirmed by the overall filter performance.

Relative filter performance was assessed in three ways. Efficiency was measured by the CPU time required for the observation processing. Predictive orbit determination

accuracy, which measures the accuracy of the filter estimate without input observations, was computed by comparing a 24 hour prediction of the final filter estimate with the simulation truth ephemeris. The filter convergence and definitive orbit determination accuracy were measured by the history of the magnitude of the position error during the observation span.

The results presented in this chapter represent a single Monte Carlo trial. Since complete Monte Carlo testing requires a large number of trials to achieve high confidence in the results, such testing was ruled out by the consequent cost. Rather, an EARLYORB initial estimate was used to give realistic initial errors. The consequence of this economical approach is the need for a word of caution; the results are promising, but further testing and experience are required.

4.2 Test Case One: FILTEST 1

This test case was used to verify the software implementations of the SKF, EKF, and LKF. The satellite observed is a low altitude satellte; only J_2 was included in the force model. C-band range and range rate observations were taken; no random errors were added to the observations. The LKF and EKF both used the truth initial conditions and dynamical model. These initial conditions and model are presented in Table 4-1. Table 4-2 shows the corresponding initial conditions and force model for the semianalytical truth ephemeris, also used by the SKF. This truth was generated by an SDC run; the errors from the Cowell truth averaged about 10 centimeters in position error and 5 millimeters per second in velocity error.

Table 4-1
FILTEST 1 Truth Model

Initial Conditions:

epoch = March 21, 1979
a = 6673.0 km
e = 0.01
i = 65.0 deg
Ω = 0.0 deg
ω = 0.0 deg
M = 0.0 deg

Dynamical model:

J_2 only in the equations of motion and variational equations

Observations:

range and range rate (C-band), no errors
1 day span

Truth Integrator:

12th order Cowell/Adams Predictor-Corrector

Step Size:

50.0 sec.

EKF/LKF Integrator:

4th order Runge-Kutta Fehlberg

Step Size:

10.0 sec.

Table 4-2
FILTEST 1 Semianalytical Truth Model

Initial Conditions:

epoch = March 21, 1979
a = 6664.673 km
e = 0.0093
i = 64.9835 deg
Ω = 0.0 deg
ω = 360.9999 deg
M = 0.0001 deg

Integrator Step Size: 43200.0 sec.

Force Model:

AOG: J_2, J_2^2 e^0

SPG: J_2, J_2^2 e^0

APG: J_2

SPPG: J_2 e^0

The final estimation errors for all filters from their respective truth ephemerides were less than 10 centimeters maximum in total position error. The SKF tests all used the short periodic coefficient interpolator and the state transition matrix interpolator. One run also used the local position and velocity interpolator and others tested the end-of-integration grid relinearization. All tests were positive. These results verify the software implementations of the SKF, EKF, and LKF. The ESKF was developed later; its implementation was verified by similar tests.

4.3 Test Case Two: WNMTST

A critical test of a filter's performance is its transient response to the initial conditions. The transient response is especially important for the nonlinear estimation problem because filter estimates diverge if the required corrections are too large. This test case is posed as a rigorous test of the model accuracy of the Semianalytical Satellite Theory in the presence of large initial condition errors by including a (21x21) gravity field and atmospheric drag in the force model. The next section gives the complete problem statement. Then the performance properties of each of the SKF, ESKF, LKF, and EKF are described, following with a section comparing the filters' performance with the SDC and CDC baselines.

4.3.1 Test Case Formulation

This test case was formulated along the lines discussed in Section 4.1. The complete description of the truth model is given in Table 4-3. The truth trajectory in osculating

Table 4-3
Test Case Two Truth Model

satellite: WNMTST

epoch: June 8, 1979, 3 hrs, 44 min, 6.4 sec

reference frame: 1950

coordinates:
$a = 7016.7363$ (km)
$e = 0.0535784$
$i = 97.8520$ (deg)
$\Omega = 224.4888$ (deg)
$\omega = 127.3311$ (deg)
$M = 237.6709$ (deg)

drag coefficient: $C_D = 2.0$

area: $A = 1.0$ (m^2)

mass: $m = 217.$ (kg)

density model: 1964 Harris-Priester atmosphere
($F_{10.7}$=150)

gravity field: 21 x 21 (GEM-9)

integrator: 12th order Cowell/Adams predictor-corrector

stepsize: 30.0 (sec)

position and velocity was generated by the high precision Cowell integrator implemented in the GTDS testbed. The GTDS DATASIM program was used to generate simulated observations; observation types and statistics, and the resulting observation history are summarized in Table 4-4. There are several interesting facets of this orbit determination problem.

First, the observations are extremely accurate; Denham and Pines [28] argue that the effects of observation model nonlinearities become more significant for more accurate observations. Thus the situation is favorable for extended filters; linearized filters might be expected to diverge.

Second, both stations are at approximately the same latitude; since the orbit is nearly polar this means that both stations will observe the same relative point in the orbit but at different times. This creates an interesting problem in observation geometry for the estimator; the eccentricity and the argument of perigee may be hard to estimate.

Finally, only 333 observations (approximately 20 minutes total observation time) are taken of the satellite during its passage of two stations. The resulting estimate accuracies will be an interesting indication of the rate of filter convergence.

A Semianalytical truth ephemeris was generated from the Cowell truth ephemeris using a PCE. The PCE elements and their generating Semianalytical model corresponding to the osculating model of Table 4-3 are shown in Table 4-5. The resulting mean-plus-short periodics trajectory is compared

Table 4-4
Test Case Two Observation Data

Station 1:

AMOSQ

TRANSMITTER : TYPE-C-BAND FREQUENCY-2200.000 MH.

	HEIGHT	LATITUDE				LONGITUDE			
COORDINATES	3.048 KM	20	42	0.0	(DDD MM SS.SSS)	203	42	0.0	(DDD MM SS.SSS)
ERROR	0.0 M	0	0	0.0	(MM SS.SSS)	0	0	0.0	(MM SS.SSS)

MINIMUM ELEVATION ANGLE IS 5.000DEGREES

observation type (C band)	Statistics (standard dev)	
Range	0.1	(m)
Azimuth	0.003	(deg)
Elevation	0.003	(deg)

Station 2:

MALABQ

TRANSMITTER : TYPE-C-BAND FREQUENCY-2200.000 MH.

	HEIGHT	LATITUDE				LONGITUDE			
COORDINATES	-0.004 KM	28	1	12.000	(DDD MM SS.SSS)	279	18	50.400	(DDD MM SS.SSS)
ERROR	0.0 M	0	0	0.0	(MM SS.SSS)	0	0	0.0	(MM SS.SSS)

MINIMUM ELEVATION ANGLE IS 5.000DEGREES

observation type (C band)	Statistics (standard dev)	
Range	2.0	(m)
Azimuth	0.000556	(deg)
Elevation	0.000556	(deg)

Station Pass History

REV NUM	0	1	2	3
START	790608	790608	790608	790608
	20637	34406	52136	65905
A AOS				790603
				70110
O LOS				790608
S				70930
Q ELMAX				15
AOSL				790608
				203558
M AOS		790608		
A		34600		
L LOS		790608		
A		35550		
B ELMAX		23		
Q AOSL		790608		
		222315		

AOS = ACQUISITION OF SIGNAL
LOS = LOSS OF SIGNAL

ELMAX = MAXIMUM ELEVATION ANGLE THIS PASS
AOSL = LOCAL TIME OF AOS

Total observation time: 3 hrs, 23 min from the start of obs by MALABQ until the completion of obs by AMOSQ

Table 4-5
Filter Test Case Two Semianalytical Truth Model

satellite: WNMTST

epoch: June 8, 1979, 3 hrs., 44 min., 6.4 sec.

reference frame: 1950

coordinates:

Mean Equinoctial	Mean Keplerian
a = 7008.0073 km	a = 7008.0073 km
h = -0.0073252	e = 0.05381336
k = 0.0533125	i = 97.858667 deg
p = -.08041503	Ω = 224.43964 deg
q = -0.8136052	ω = 127.68685 deg
λ = 229.48174 deg	M = 237.30524 deg

drag coefficient = C_D = 2.0

area: a = 1.0 (m^2)

mass: m = 217. (kg)

density model: 1964 Harris-Priester atmosphere ($F_{10.7}$=150)

gravity field:
- 21x21 (Gem-9) averaged potential
- AOG resonance (15,15) - (21,15) shallow
  - second order J_2 and Drag and coupling
  - zonal short periodics (21x0)
  - sixth order e
  - m-daily short periodics (21x21)
- SPG sixth order e
  - tesseral short periodics (21x19)
  - sixth order e

integrator: 4th order Runge-Kutta

stepsize: 43200. (sec) = 1/2 day

to the Cowell truth in Figures 4-1 through 4-3. The quadratic growth in the errors is due to slight initial condition errors. The excellence of the Semianaytical model is shown by the small magnitude of the errors during the fit span from 0 to 5 hours. The position error RMS during the fit span is 5.6 meters, while the velocity error RMS is 4.7 millimeters per second.

The EARLYORB program was used to generate approximate orbital elements for filter initialization. The LKF and EKF used these elements directly; corresponding mean elements for SKF and ESKF initialization were generated by PCE applied to the osculating EARLYORB elements and by EPC using the iteration (4-1). The EPC converged in five iterations to elements consistent to 10 decimal places. Clearly the errors from the PCE elements are small. All of these element sets are shown in Table 4-6. The perturbations of the osculating and PCE mean EARLYORB elements from the true elements are also given. The initial error in both the osculating elements and the mean elements is about 50 kilometers. These initial errors provide a good initial error for testing filter convergence.

4.3.2 SKF Properties

This section presents results from an investigation of the effects of four variables on SKF performance. The variables that were investigated are:

1. force model selection for the equations of motion and the variational equations;

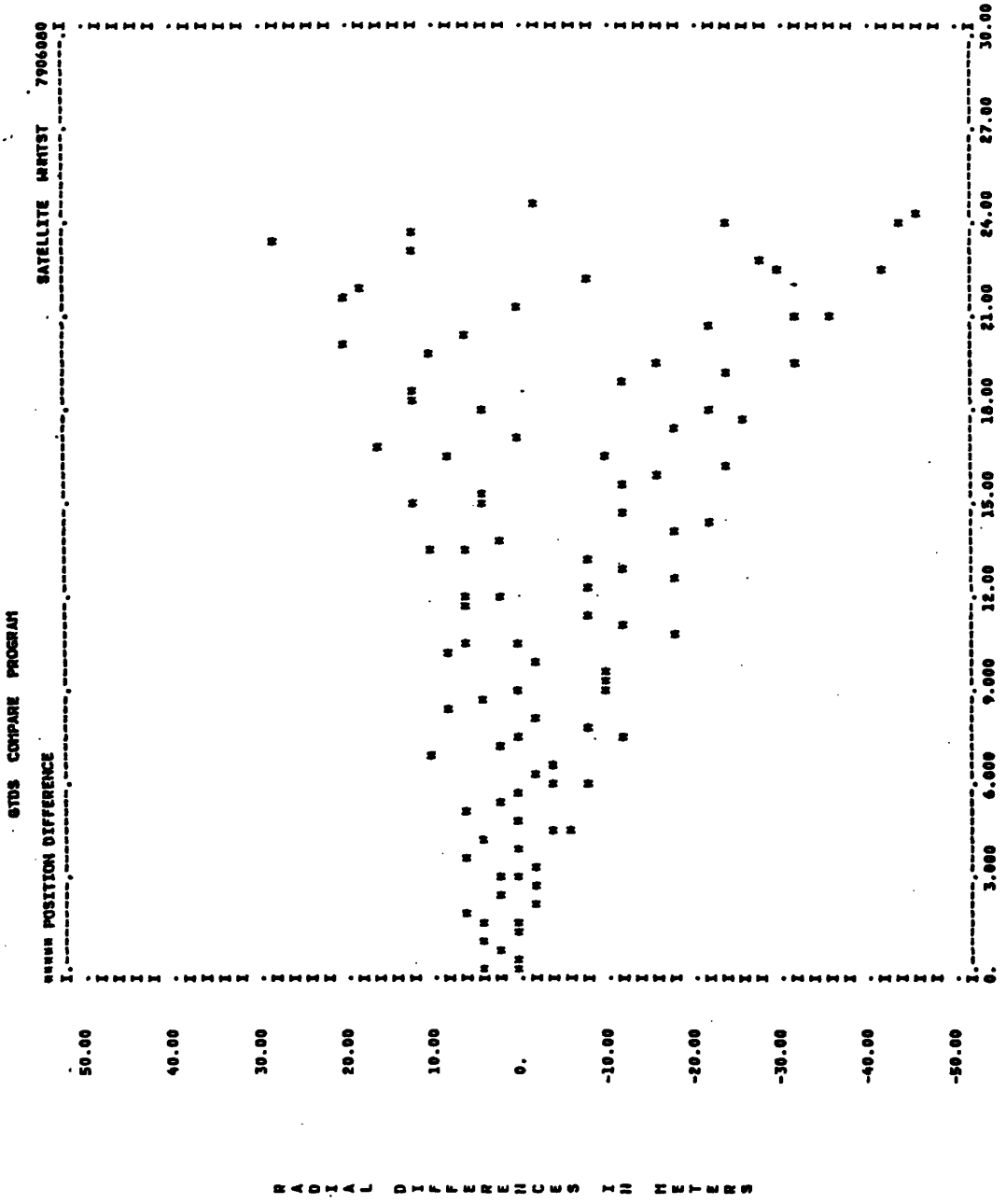

Figure 4-1. Semianalytical Truth Radial Track Error

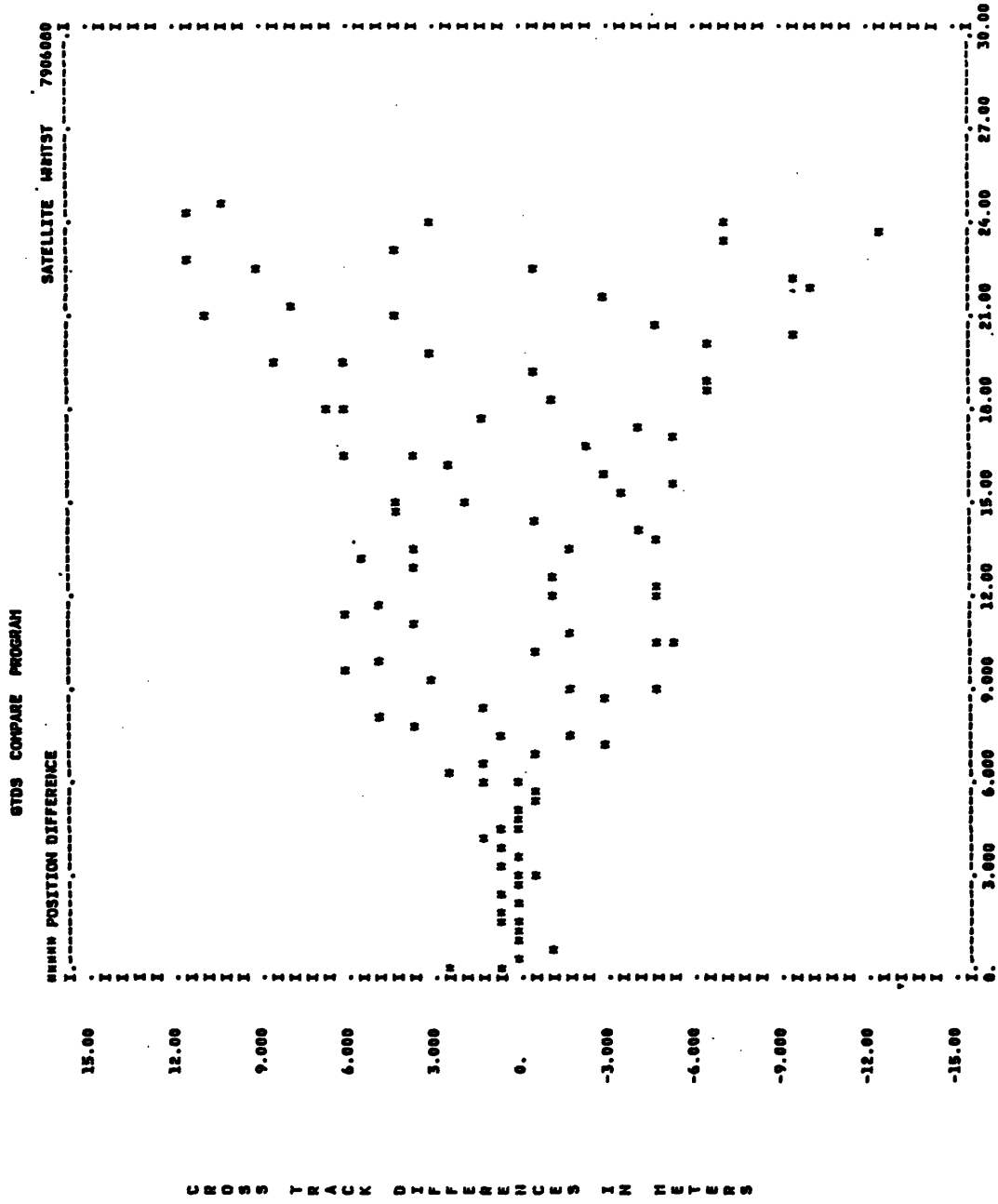

Figure 4-2. Semianalytical Truth Cross Track Error

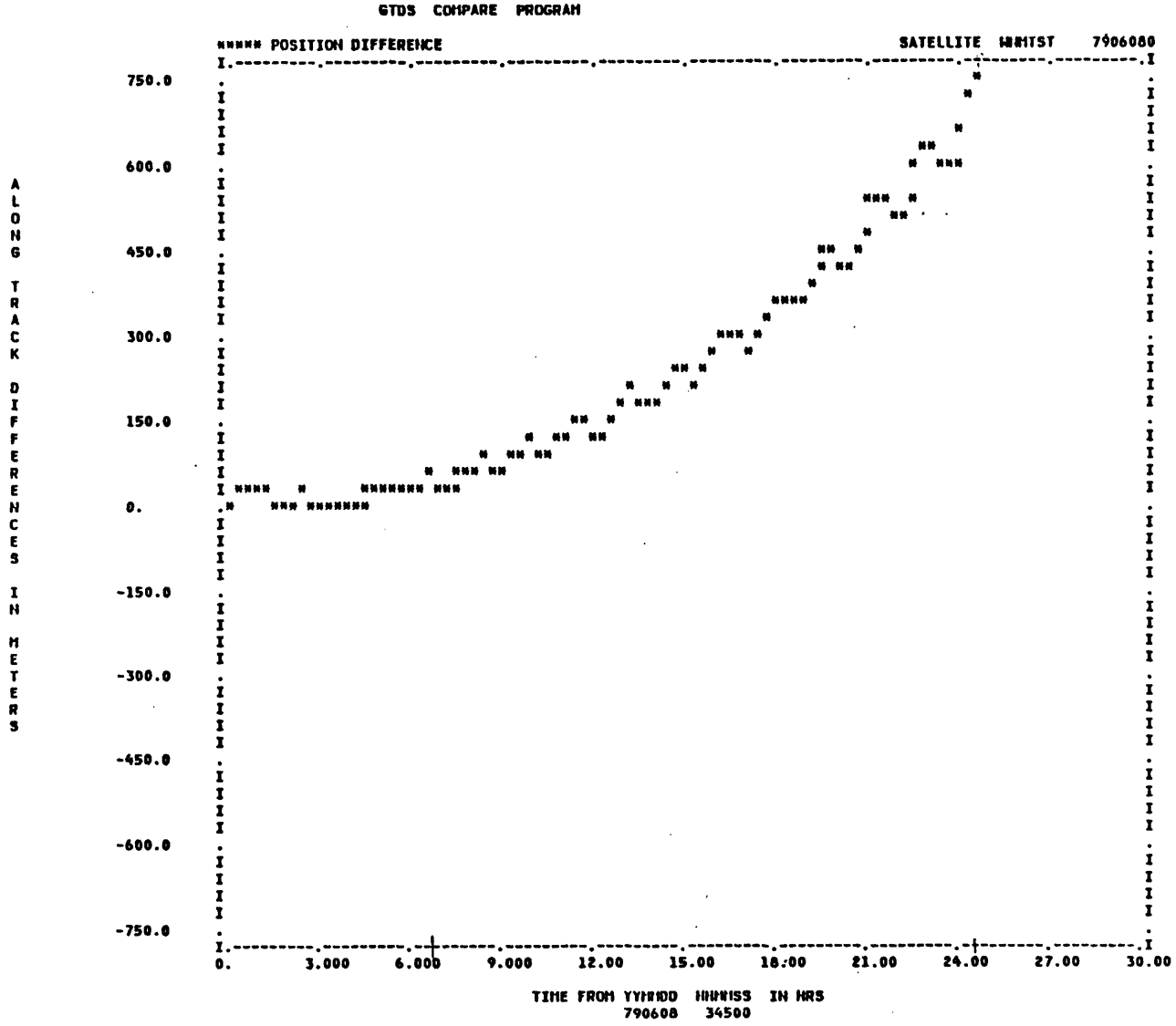

Figure 4-3. Semianalytical Truth Along Track Error

Table 4-6
Osculating and Mean Early Orbit Elements and Initial Perturbations

Early Orbit Keplerian Elements

	Osculating	PCE Mean	EPC Mean
a	7004.285	7005.566	7005.173
e	0.054123	0.054359	0.054302
i	97.9693	97.9766	97.9646
Ω	224.848	224.849	224.847
ω	127.380	127.730	127.824
M	237.566	237.207	237.114

Osculating and Mean Perturbations

	Osculating Cartesian		Mean Equinoctial
Δx	32.86 (km)	Δa	2.44 (km)
Δy	33.71 (km)	Δh	0.3038E-3
Δz	12.36 (km)	Δk	0.5920E-3
ΔVx	23.26 (m/s)	Δp	0.68E-2
ΔVy	0.47 (m/s)	Δq	0.337E-2
ΔVz	3.34 (m/s)	$\Delta \lambda$	0.529E-2
$\|\|\underline{\Delta r}\|\|$	48.67 (km)	$\|\|\underline{\Delta r}\|\|$	48.55 (km)
$\|\|\underline{\Delta v}\|\|$	23.50 (m/s)	$\|\|\underline{\Delta v}\|\|$	22.21 (m/s)

2. selection of the process noise covariance and the initial state covariance;

3. trajectory update considerations for the nominal trajectory used in the SKF; and

4. mean state initialization by PCE and EPC.

The filtering issues (1) to (4) above provide a natural test grid for exploring the properties of the SKF. Two options are presented for each issue or consideration. With a total of four questions to be examined, the resulting grid has sixteen points. The tests reported have essentially diagonalized the grid, providing insight into the interaction of each of the issues. The options available are summarized in Table 4-7 in the context of the list of issues.

The force model issue explores the effect of one force model truncation on filtering accuracy. The process noise options test the sensitivity of the SKF to the process noise strength. The relinearization of the SKF nominal trajectory after a station pass causes the SKF to look more like an EKF. The relinearization option was implemented by changing the integration grid length. Additional confirmation of the approximate EPC procedure (4-1) is given by performance measurements in actual runs.

Seven SKF runs tested various combinations of these options. The options used for each run and the resulting performance are given in Table 4-8. The final estimate of each SKF run was used as the initial condition for a 24-hour predicted ephemeris. The RMS values given in Table 4-8 are

Table 4-7
Issues and Options Investigated for the SKF

Issue	Option 1	Option 2	Comments
1. Force Model	AOG: (21x21), resonance Drag 2nd order: J_2-J_2 J_2-Drag, Drag-J_2 Drag-Drag SPG: zonals (21x0) (e_0-e_6) m-dailies (21x21) (e_0-e_6) tesserals (21x19) (e_0-e_6)	AOG: (21x21), resonance Drag 2nd order: J_2-J_2 Drag-J_2 SPG: zonals (21x0) (e_0-e_6) m-dailies (21x21) (e_0-e_6) tesserals (21x19) (e_0-e_1)	Option 1 is the same as the PCE truth, Table 4-5; Option 2 is much more efficient
2. Process Noise Strength	$Q_1 = \text{diag}[10^{-18}, 10^{-24}, 10^{-24}, 10^{-22}, 10^{-22}, 10^{-22}]$	$Q_2 = \text{diag}[10^{-10}, 10^{-12}, 10^{-12}, 10^{-14}, 10^{-14}, 10^{-12}]$	all runs used $P_0 = [1.0, 10^{-8}, 4\times10^{-8}, 4\times10^{-6}, 10^{-6}, 4\times10^{-6}]$
3. Trajectory Updates	Relinearize after each station pass	Relinearize after processing all the observations	Integrator step sizes Option 1:3100 sec Option 2:6200 sec
4. Mean State Initialization	PCE EARLYORB	EPC EARLYORB	see Table 4-5 for these elements

Table 4-3
SKF Test Grid Runs and Performance

TEST RUNS	A	B*	C*	D	E	F	G
1 Force Model	2	1	1	2	2	2	1
2 Process Noise	1	2	2	2	1	2	2
3 Trajectory Upd.	1	1	1	1	2	2	1
4 Early Orbit	1	1	1	1	1	1	2
PERFORMANCE (km)							
Radial RMS	2.6	.25	.3	.24	2.7	.19	.3
Cross RMS	3.6	.21	.3	.22	3.2	.37	.3
Along RMS	21.6	7.2	7.3	7.0	19.2	1.14	9.0
Total RMS	22.0	7.2	7.3	7.0	19.7	1.22	9.0

* Run B used the coefficient interpolator only; Run C used the position and velocity interpolator (step = 100 sec) as well as the coefficient interpolator.

the root mean squared residuals of these predicted ephemerides from the Cowell Truth ephemeris of Table 4-3. The results shown support the following statements:

1. use of the position and velocity interpolator does not seriously impact SKF performance (the observed RMS increase is probably accentuated by the highly accurate observations) [B, C];

2. the truncated force model does not seriously impact SKF performance [B, D];

3. SKF accuracy is very sensitive to the process noise strength choice [A, D and E, F];

4. more frequent trajectory updates in a convergence test do not necessarily speed convergence or improve accuracy [A, E and D, F];

5. The EPC mean EARLYORB procedure does not seriously impact SKF performance [B, G].

The letters in brackets reference the runs in Table 4-8 supporting the statement. The results in Table 4-8 are consistent with filter histories of the various runs. This means that the filter runs have converged, so the results shown are not especially dependent on the particular filter output estimate used to generate the predicted ephemeris.

The changes in performance in the sequence of runs A, D, and F is remarkable. The performance in each case is dominated by the along track error. The performance improvements from run A to D to F correspond directly to

decreases in the error of the final semimajor axis estimate from 130 meters to 70 meters to 7 meters. Figures 4-4 through 4-8 show plots comparing runs D and F. Figure 4-4 shows the along track prediction error for run F; it contains a .5 kilometer amplitude error at the orbital frequency. This error is due to coupling between the semimajor axis and the error in the satellite angle. Figures 4-5 and 4-6 show the semimajor axis filtering histories for runs F and D, respectively; the variable DA plots the error while PA is a 3σ standard deviation bound. Figure 4-6 graphically shows the bias in the final semimajor axis estimate of run D. Both figures otherwise show very similar behavior. Figures 4-7 and 4-8 show the filter histories of the total estimate position error DR, with the 3σ bound PR also plotted. Once again, the SKF runs D and F show very similar behavior, including similar final position errors of about 300 meters. Both show final standard deviations of about 10 meters. It is interesting to note the error transient in Figure 4-8 for run D: at 11800 seconds a spike occurs indicating a position error of about 1.1 kilometers. The transient occurs at the start of the new station pass, after a 3 hour outage. Any such similar transient for run F has been overwritten by the 3σ standard deviation history. The presence of such a transient is consistent with the apparent divergence of these SKF runs; the actual errors are 30 times their standard deviations. Note that this divergence is probably only apparent; additional observations should serve to make the errors and their standard deviations consistent. Two final conclusions are drawn:

1. An adequate process noise model for the linearization errors due to initial condition errors would

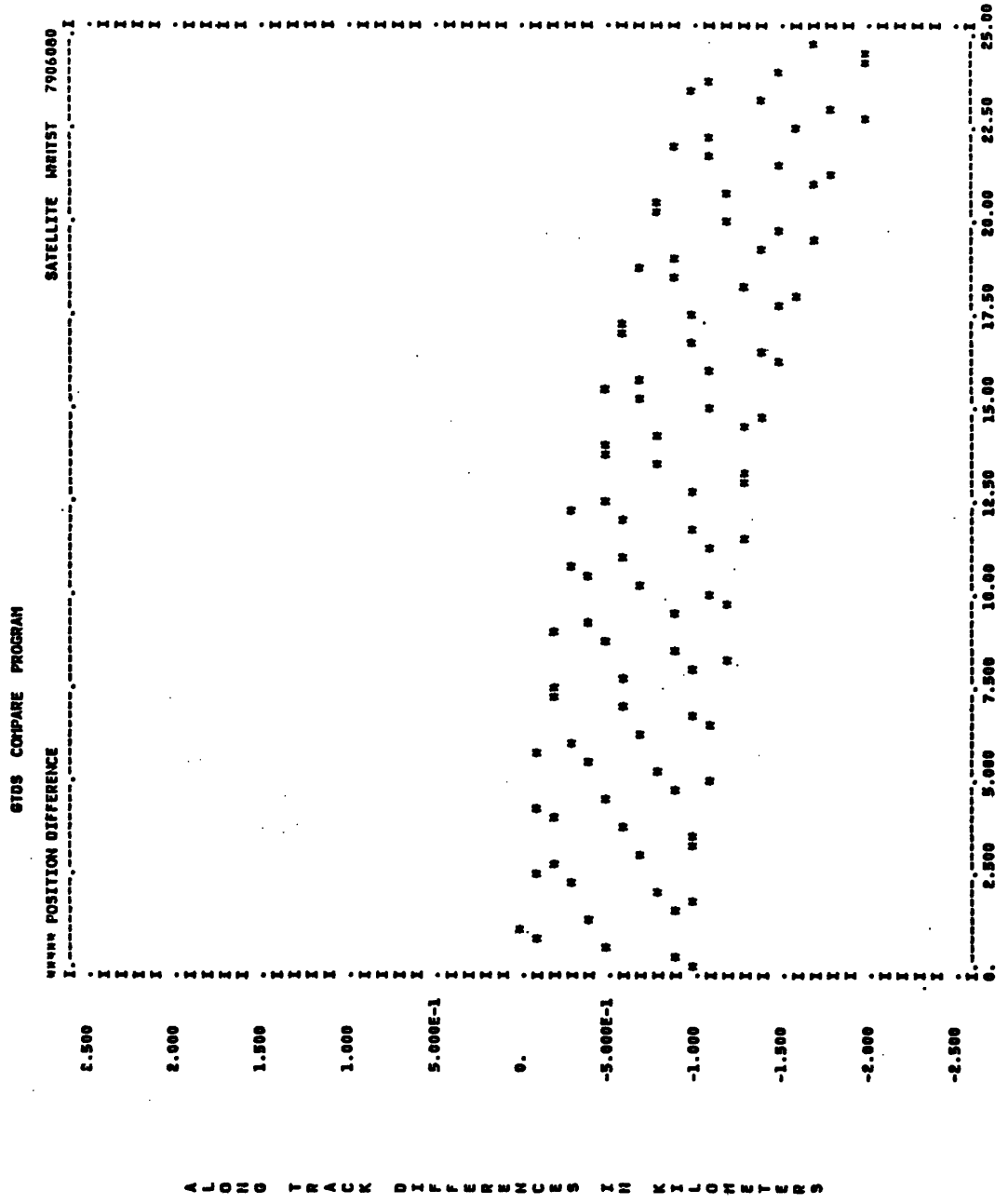

Figure 4-4. SKF Along Track Prediction Error, Run F

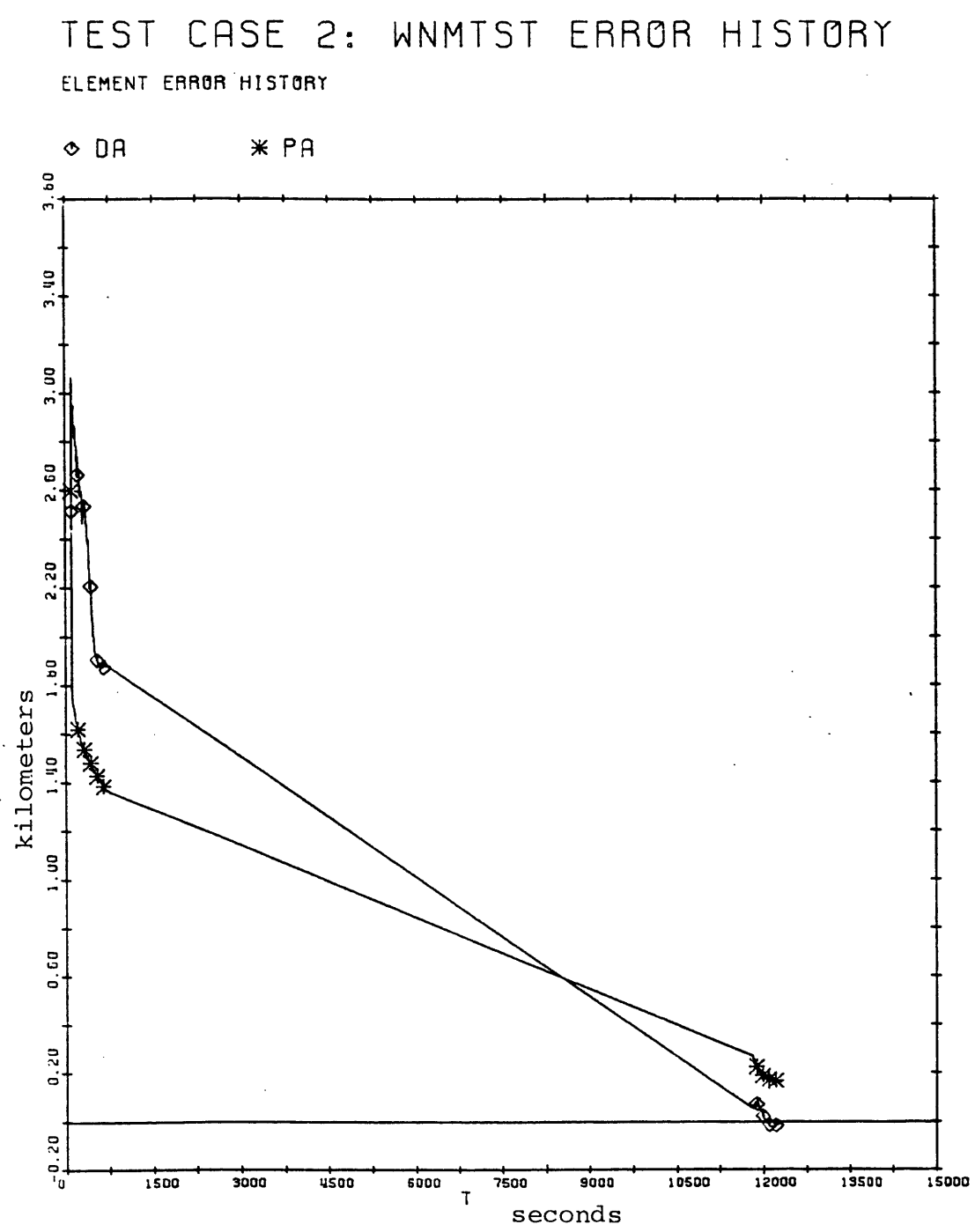

Figure 4-5. SKF Semimajor Axis Error History, Run F

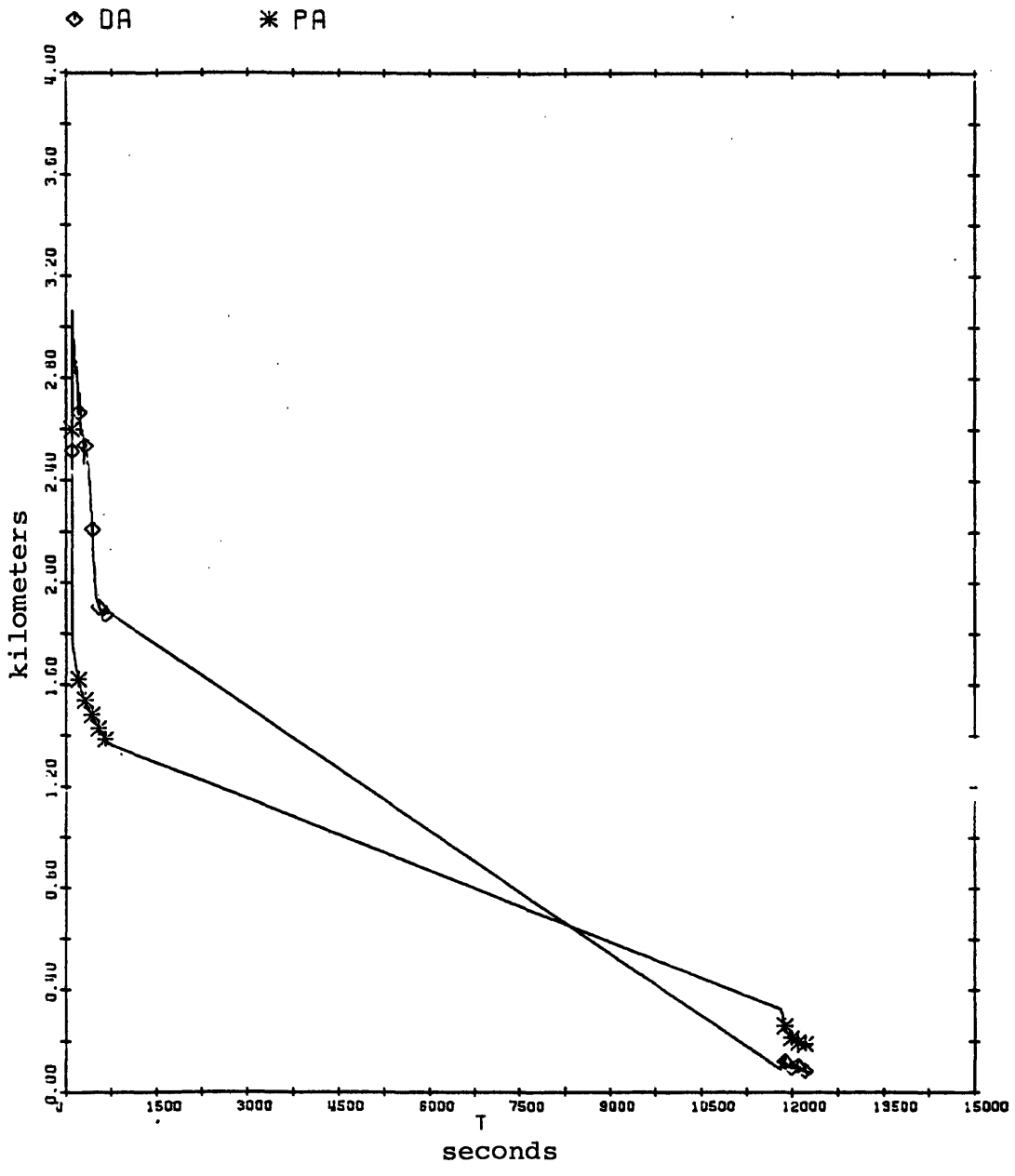

Figure 4-6. SKF Semimajor Axis Error History, Run D

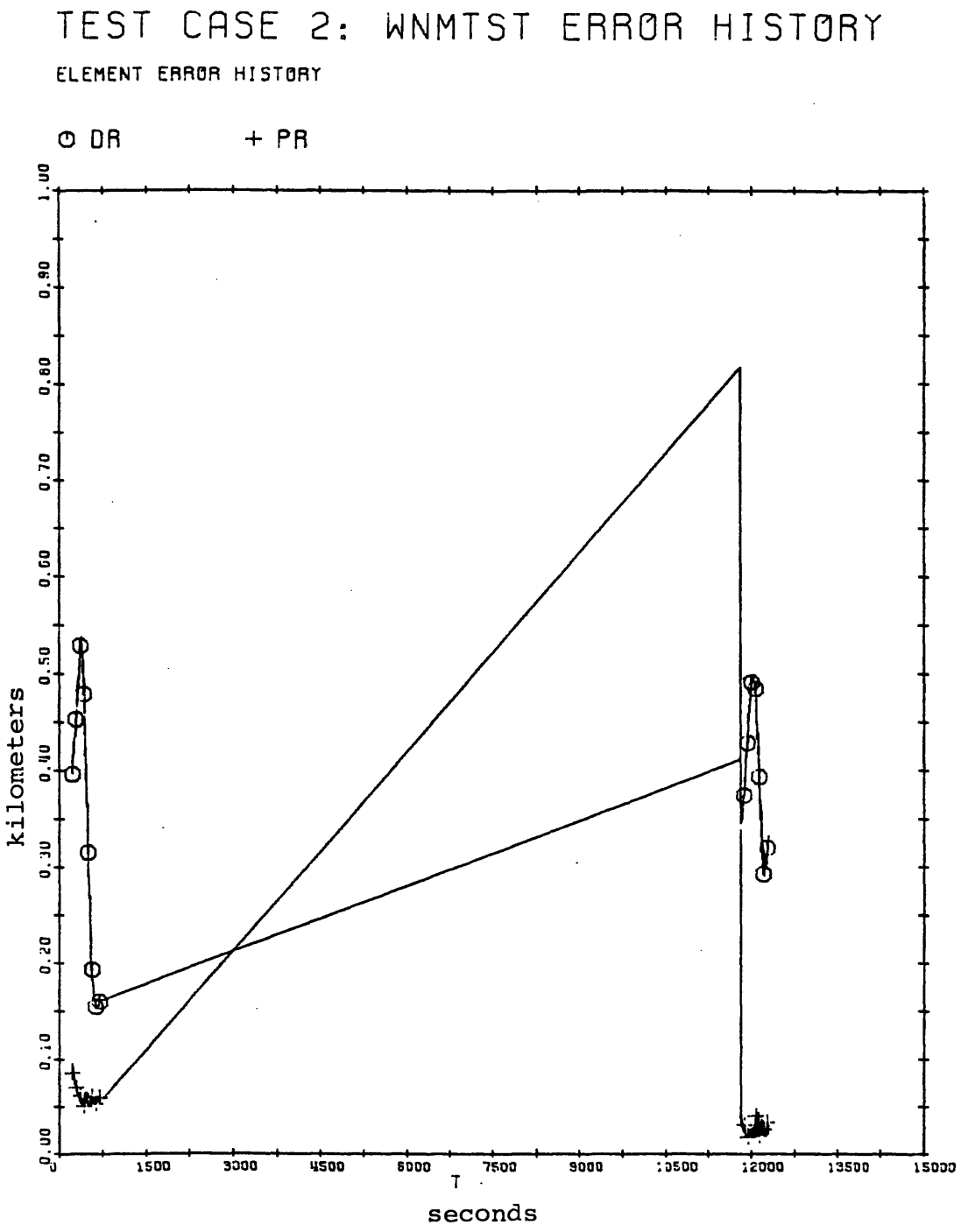

Figure 4-7. SKF Position Error History, Run F

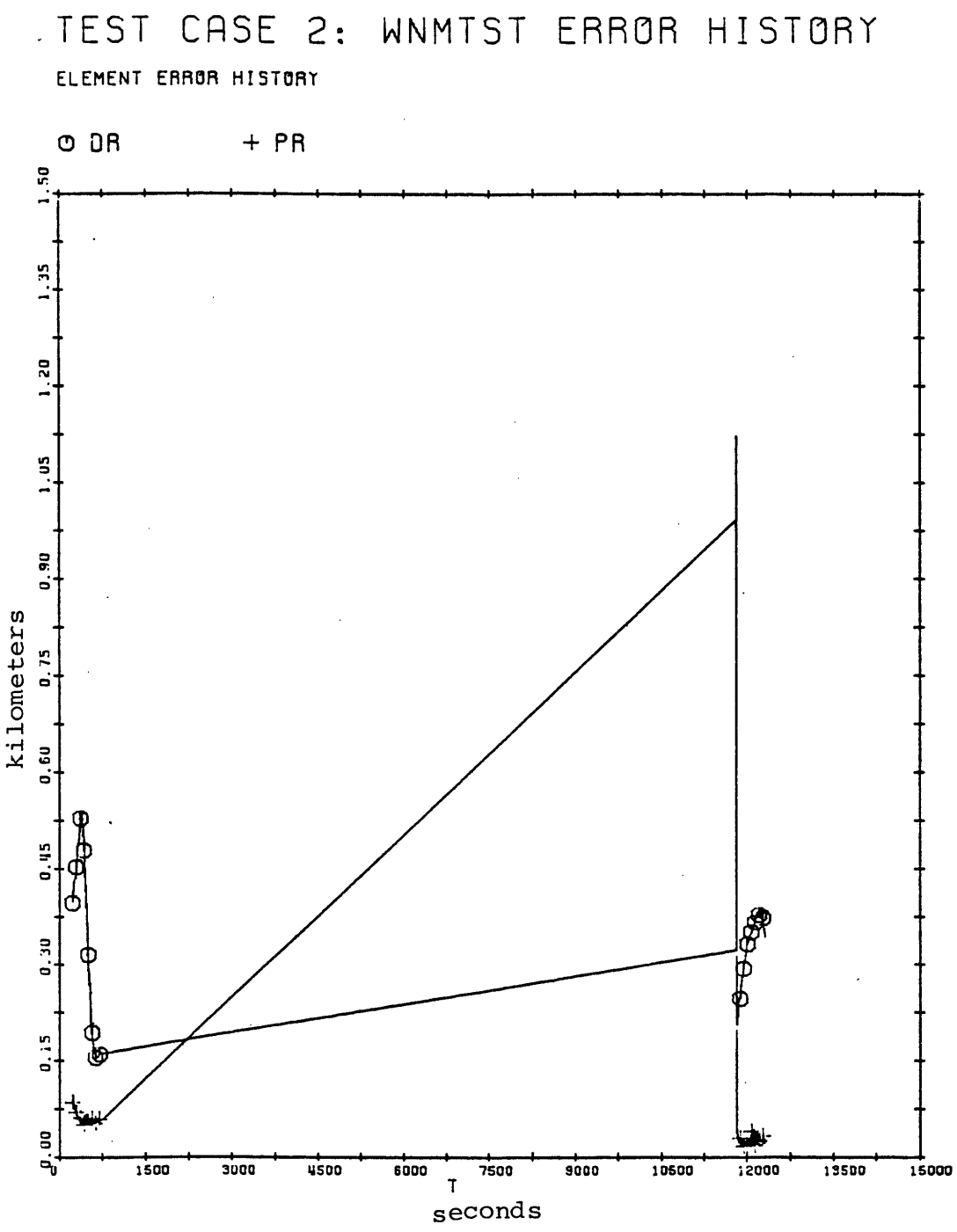

Figure 4-8. SKF Position Error History, Run D

help prevent such apparent divergence. The discussion in Appendix A provides one approach. Jazwinski's [24] Adaptive Noise filter gives another possibility.

2. In the same vein, filters using global linearizations without further compensation are likely to suffer convergence problems. This can be taken as directly motivating the development of the ESKF.

4.3.3 ESKF Properties

This section describes a series of tests investigating the performance impact of five input parameters. Three of the parameters were held in common with the SKF investigation above. Process noise sensitivity was not investigated; all ESKF runs used process noise option 2 from Table 4-7. The two new input parameters and the motivation for their consideration are:

(i) ESKF interpolator implementation: In the discussion of the ESKF design, two implementations were presented for use according to the interpolator structures being accomodated. Equation (3-9) applies to the case where only the short periodic coefficient interpolator is used; equation (3-10) is employed when the short-arc interpolator for osculating position and velocity is also being used. These are options 1 and 2, respectively.

(ii) B_1 matrix computation: Both equations (3-9) and (3-10) assume that the B_1 matrix (i.e., the short periodic function state partials

matrix) is being computed. This corresponds to the linearization of the short periodic functions about the nominal trajectory. Experience [19] with the SDC has shown that the B_1 matrix is not important to SDC estimation accuracy or convergence. The SKF tests above did not employ the B_1 matrix. A decision to truncate the B_1 matrix for the ESKF is not simple: if the state correction $\Delta\underline{a}$ becomes large enough, a significant estimate bias will be introduced by its neglect. Option 1 neglects B_1 computation; option 2 includes the B_1 matrix due to the J_2 perturbation, computed analytically to zeroth order in the eccentricity.

Table 4-9 summarizes the input parameters investigated for the ESKF. Table 4-10 presents the test results. All of ESKF test runs show a marked improvement over corresponding SKF runs. This data supports the following statements:

1. The approximate EPC procedure does not seriously impact ESKF performance [A, B];

2. The truncated force model does not seriously impact ESKF performance [A, C];

3. More frequent nominal trajectory updating and relinearization does not necessarily improve ESKF performance [C, D and F, G];

4. The computation of the B_1 matrix can improve (significantly) ESKF accuracy [C, F] ([D, G]);

Table 4-9
Summary of ESKF Test Options

Input Parameter	Option 1	Option 2	Comments
1. Force Model	full	truncated	see Table 4-7
2. Trajectory Updates	update after each station pass	update at the end of the observation span	see Table 4-7
3. Mean EARLYORB init.	PCE	EPC	see Table 4-7
4. ESKF* mode	PV interp. off	PV interp. on	pv off: (3-9) pv on: (3-10)
5. Short periodic partials computation	neglect the B_1 matrix	compute the B_1 matrix	B_1 is computed analytically including J_2 at e^0

* When used, the position and velocity interpolator had a step size of 120 seconds for a total span of 4 minutes.

Table 4-10
ESKF Parameter Test Results

Input Parameter	Test Runs*						
	A	B	C	D	E	F	G
1. force model	1	1	2	2	2	2	2
2. trajectory updates	1	1	1	2	1	1	2
3. mean init.	1	2	1	1	1	1	1
4. ESKF mode	1	1	1	1	2	1	1
5. B_1 matrix	1	1	1	1	1	2	2
Performance**							
Radial RMS	.197	.213	.183	.196	.231	.166	.174
Cross RMS	.020	.024	.019	.013	.026	.016	.019
Along RMS	.930	.336	1.153	1.345	.559	1.185	.500

* all test runs used covariance parameters

$P_o = \text{diag}[1.0, 10^{-8}.10^{-8}, 10^{-6}, 10^{-6}, 10^{-6}]$

$Q = \text{diag}[10^{-10}, 10^{-12}, 10^{-12}, 10^{-14}, 10^{-14}, 10^{-12}]$

** performance is measured by computing the root mean squared residuals of the differences between the Cowell truth ephemeris of Table 4-3 and a 24 hour predicted ephemeris based on the final filter estimate.

5. The ESKF using the position and velocity interpolator can produce satisfactory predictions.

The data in Table 4-10 is limited in depth; quite clearly only very conservative conclusions can be drawn from these results. And yet, even in this light, statement (5) above is startlingly conservative. The reason for this lies in the limitations of the prediction error RMS performance measure used in Table 4-10.

Figures 4-9, 4-10, and 4-11 show the dominant along track prediction errors for runs A, E, and G, respectively. Each of the ESKF runs uses the same strategy to reduce the prediction RMS: the along track error is biased such that the RMS is reduced by the distribution of initial errors in the mean semimajor axis and the mean-mean longitude. In all cases, both the semimajor axis estimate and the mean longitude estimate are too large. The increased semimajor axis causes a decrease in the mean motion, implying slower growth in the too-large mean longitude. Thus the mean longitude error will cross zero within the predict span, causing the reduction in the along track RMS. Table 4-11 summarizes the final estimation errors in the osculating Keplerian elements for each of the runs A, E, and G. Note the generally superior accuracy of run G.

The inadequacy of the prediction error RMS performance measure alone is indicated by the filter history plots in Figures 4-12 to 4-14. These figures show plots of the position error history for runs A, E, and G respectively. Notice that run G produces the smallest position errors, followed by run A and run E. The histories for runs A and G are essentially the same; both ESKF runs produce meter-level

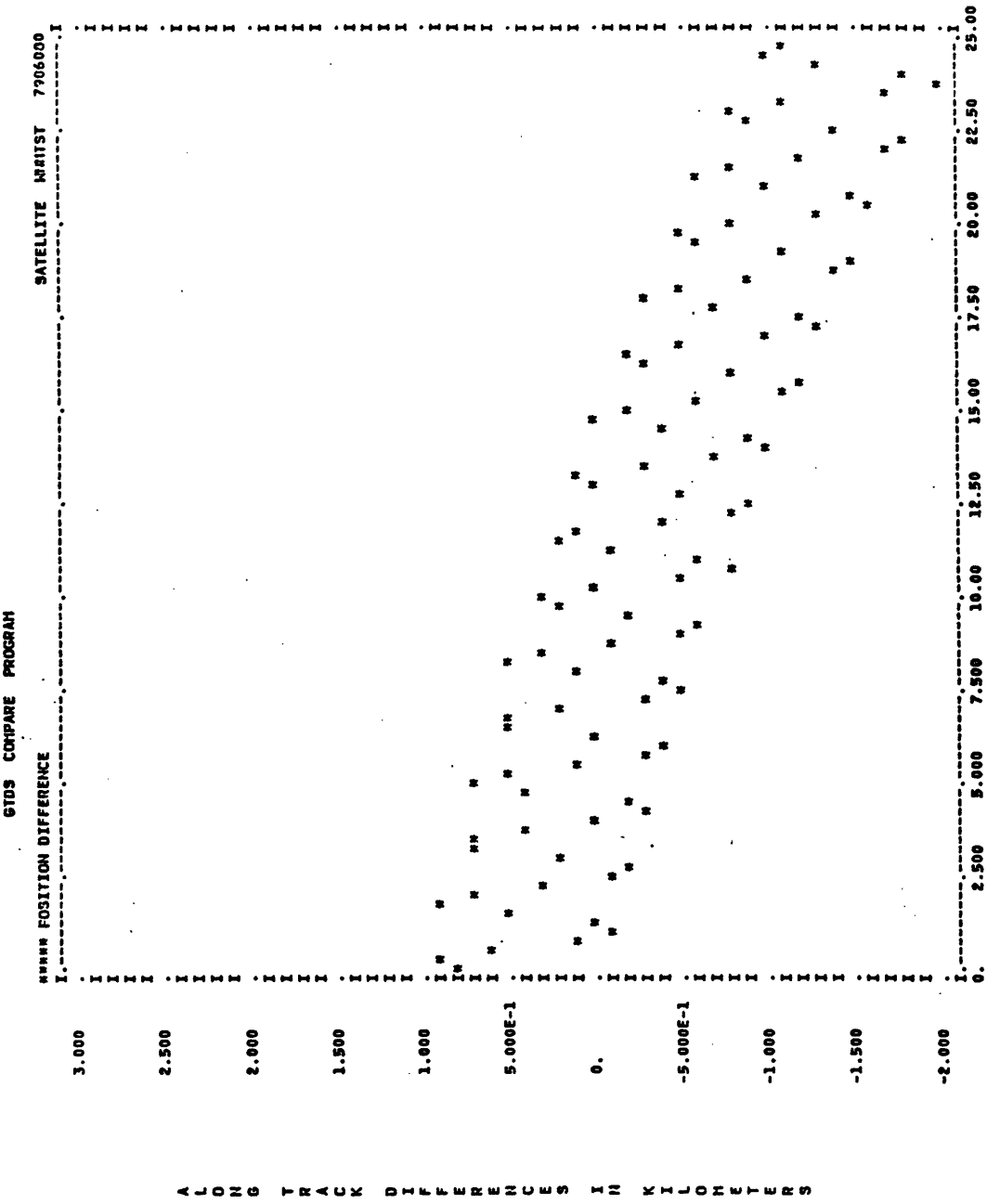

Figure 4-9. ESKF Along Track Prediction Error, Run A

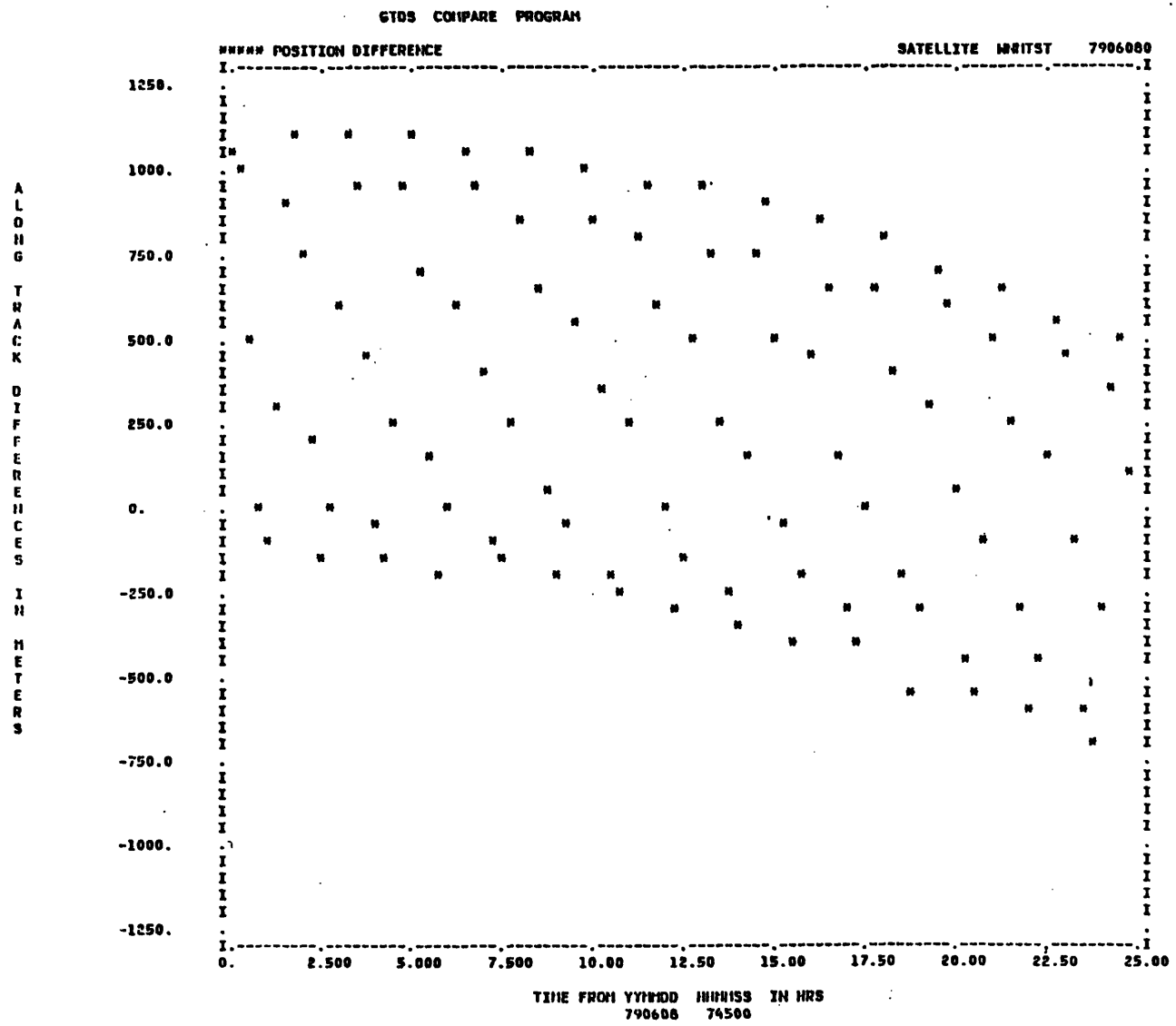

Figure 4-10. ESKF Along Track Prediction Error, Run E

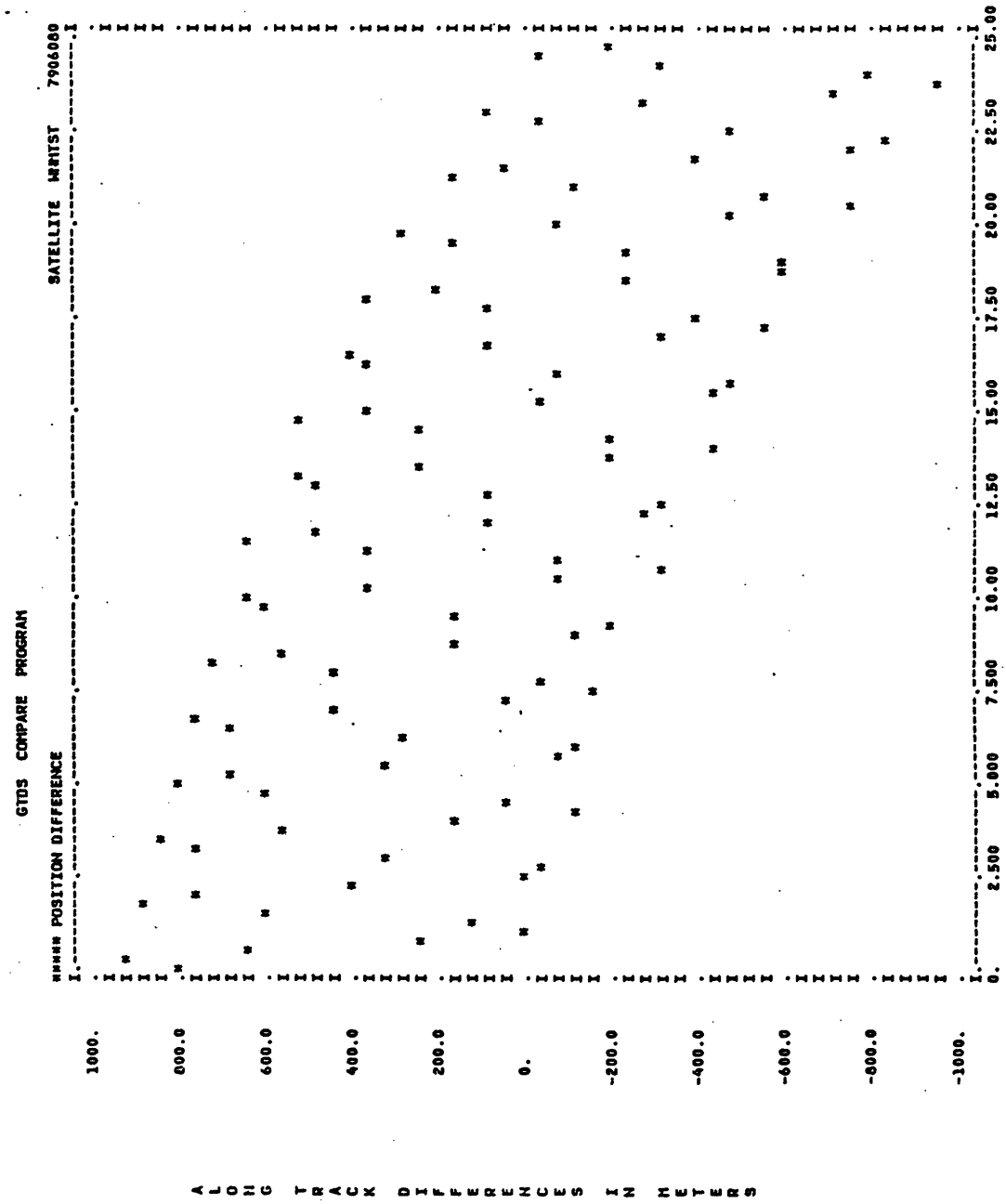

Figure 4-11. ESKF Along Track Prediction Error, Run G

Table 4-11
Final Keplerian Element ESKF Estimation Errors

Element	Run		
	A	E	G
a*	9.0	0.5	2.7
e	3.6×10^{-5}	4.2×10^{-5}	3.3×10^{-5}
i**	2.2	3.4	2.9
Ω**	2.7	3.5	1.9
ω**	-54.0	+220.0	-88.0
M**	-12.0	-290.0	+20.0
$\bar{a}$*	8.0	0.8	1.5

* units are meters

** units are microradians

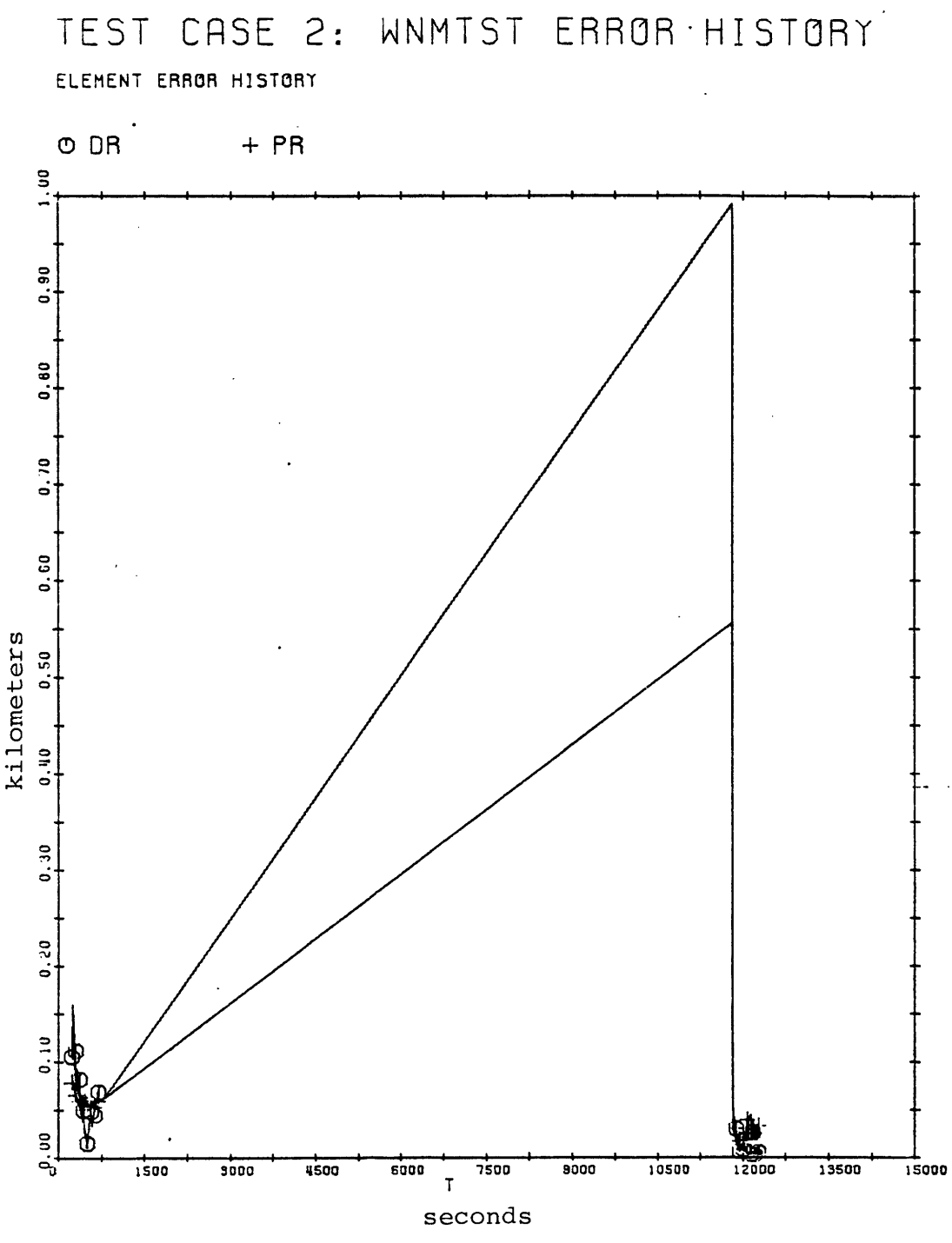

Figure 4-12. ESKF Position Error History, Run A

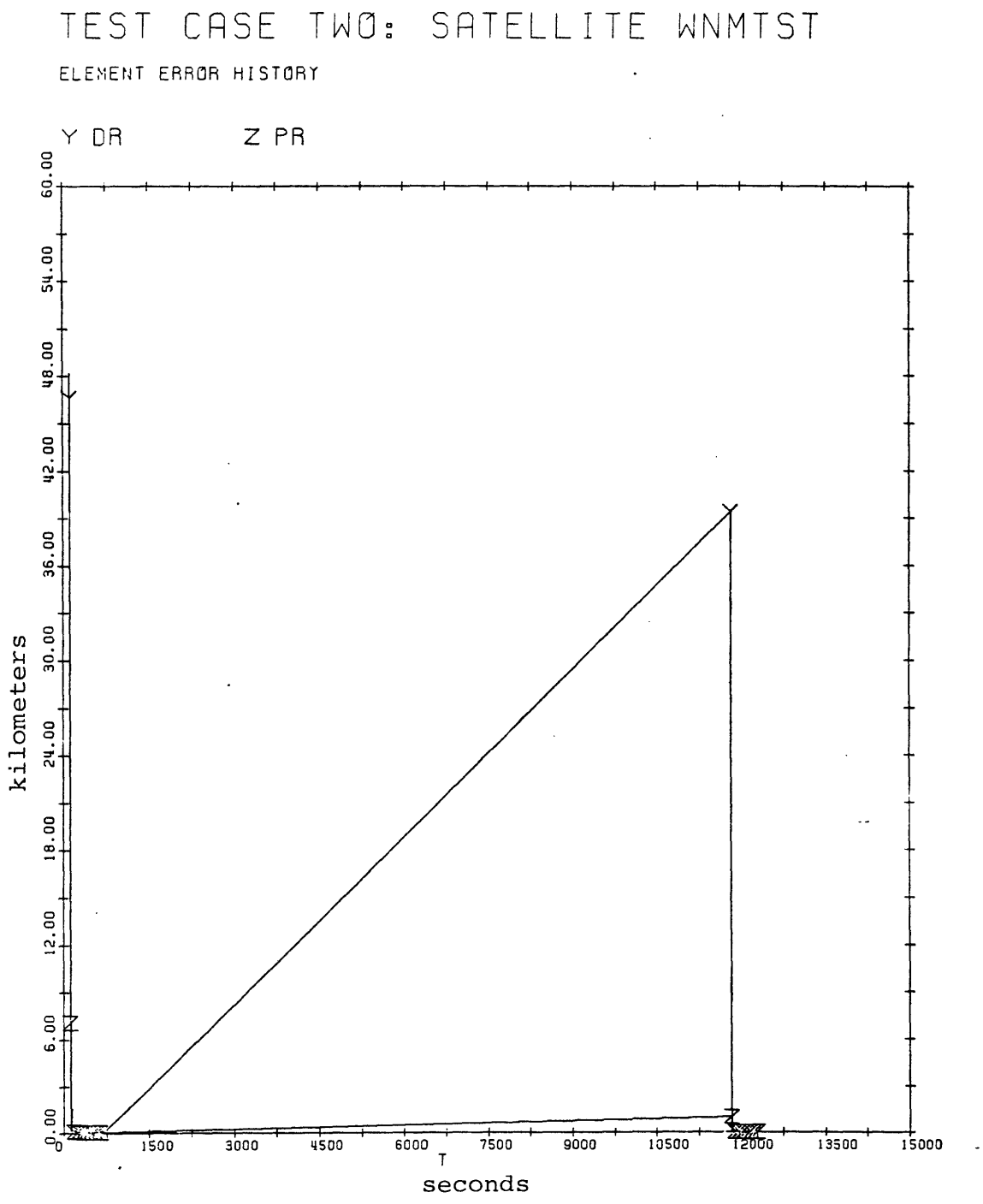

Figure 4-13. ESKF Position Error History, Run E

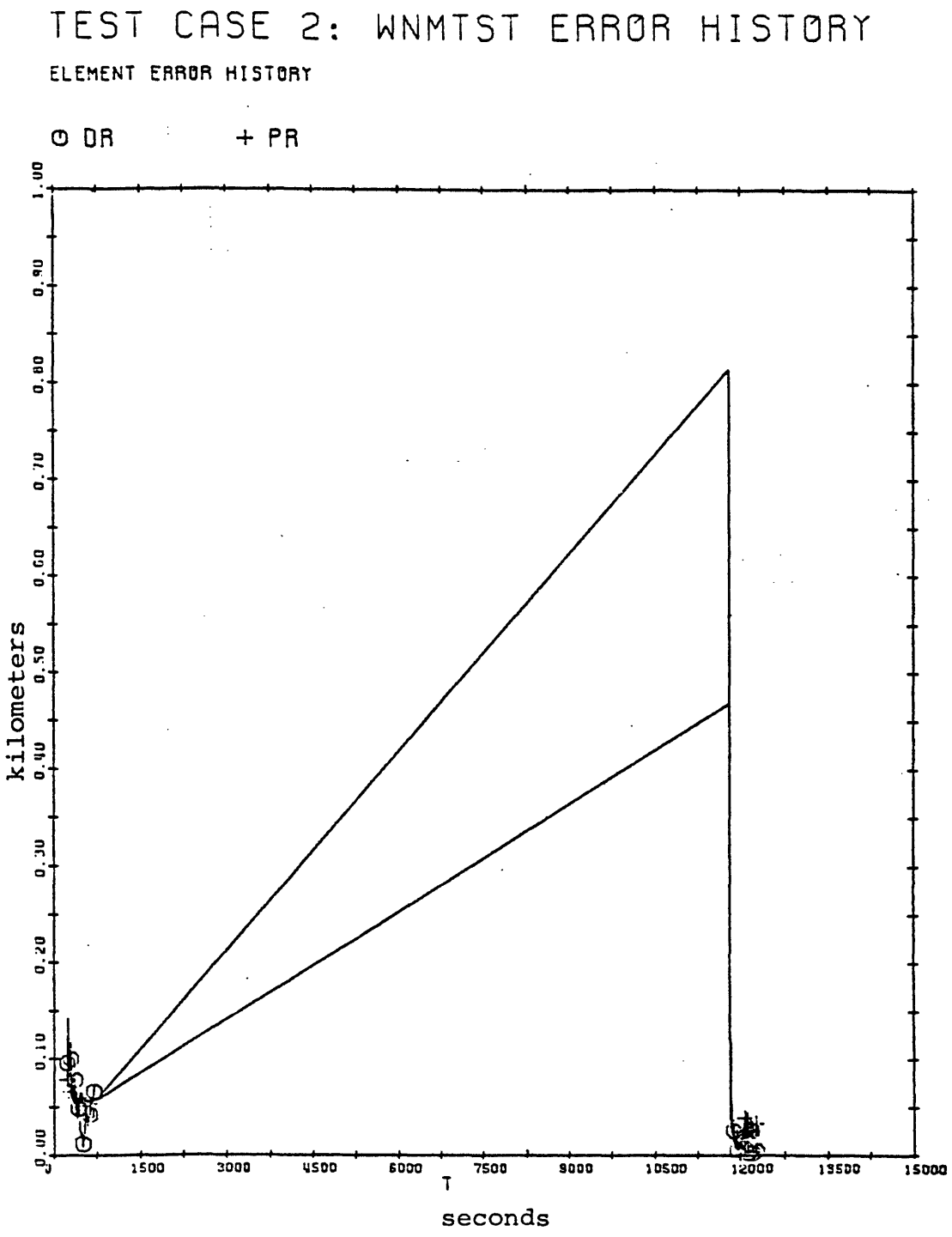

Figure 4-14. ESKF Position Error History, Run G

accuracy in their final estimates. The position error history of run E is fundamentally different. Estimate transients of several kilometers occur during both tracking station passes and the final estimate is only accurate to within 200 meters. This degraded performance probably results from the additional linearization of the two body element transform from equinoctial variables to position and velocity. Certainly the results of the observation model nonlinearity test of Section 3.4.3 indicate that the element transformation nonlinearities are often of the same order of magnitude as the observation model nonlinearities. Thus care must be exercised in the use of the position and velocity interpolator with the ESKF.

The significant results of this section are:

1. The ESKF results in greatly improved performance over comparable SKF runs, both in the filter error history and in the prediction RMS; the fact that ESKF performance does not change greatly with parameter variations is also important;

2. Calculation of the B_1 matrix can be important for ESKF accuracy;

3. The coefficient-interpolator-only ESKF algorithm gives much better performance than the position and velocity interpolator version.

4.3.4 LKF Properties

The LKF runs discussed here required making choices for three input parameters. The first two are typical estimation parameters. They are

(1) covariance parameter selection, and
(2) coefficient of drag estimation.

All LKF runs used the same a priori covariance; it was selected to be consistent with the initial condition errors and has value

$$P_o = \text{diag}[100.,100.,100.,10^{-6},10^{-6},10^{-6}]$$

Many values for the process noise strength were tested in a trial and error search for the best value. All choices were diagonal and used the same variance for all position coordinates and all velocity coordinates respectively. A process noise choice

$$Q = \text{diag}[10^{-r},10^{-r},10^{-r},10^{-s},10^{-s},10^{-s}]$$

is denoted by Q = [r,s] in the presentation of results below. If r=0 then the corresponding elements in Q are replaced by zero.

Several of the runs tested the impact of coefficient of drag estimation. While accurate drag coefficient estimation cannot usually be achieved over observation spans as short as that of this test case, the presence of the additional estimation variable does sometimes allow performance improvements.

The last input parameter tested allows the LKF to emulate SKF end-of-integration grid trajectory updating. The two options here allow relinearization after a station pass and global linearization over the observation span, respectively.

The LKF test run parameter choices and the corresponding RMS prediction errors are shown in Table 4-12. These results support the following statements.

1. Coefficient of Drag estimation for this short-arc problem does not significantly help or hurt performance [A, B and D, E].

2. The dependence of LKF performance on the process noise strength selected is complex and interesting. Runs [H, I] and [D, F] indicate that process noise should be modelled for position as well as velocity, contrary to its interpretation as an unmodelled acceleration. Runs [A, C] contradict this; the interesting thing about run A is that the large value of position process noise caused such an increase in the semimajor axis variance during the data outage between station passes that the LKF thought the orbit was hyperbolic at the start of the second pass. The changes in performance from run J to H to E to B as the process noise scaling changes are also interesting: performance is not a monotonic nor a convex function of the scaling.

3. Short-arc or station-pass relinearization may improve the performance of the LKF.

Table 4-12
LKF Parameter Test Results

Input Parameter	Test Runs*									
	A	B	C	D	E	F	G	H	I	J
1 Process Noise**	[3,7]	[3,7]	[0,7]	[6,10]	[6,10]	[0,10]	[0,10]	[10,14]	[0,14]	[13,22]
2 Drag solve	No	Yes	No	No	Yes	No	No	Yes	No	Yes
3 Trajectory update	Yes	Yes	Yes	Yes	Yes	Yes	No	Yes	Yes	Yes
Performance										
Radial RMS	55.3	55.4	3.52	3.66	3.67	5.62	29.7	5.51	6.58	2.79
Cross RMS	3.32	3.32	0.06	0.74	0.74	0.17	0.73	2.21	2.23	0.39
Along RMS	694.6	694.1	106.3	112.4	112.5	165.0	490.5	160.0	162.5	31.8

* $P_0 = \text{diag}[100.,100.,100.,10^{-6},10^{-6},10^{-6}]$

** $Q = [r,s]$ means $Q = \text{diag}[10^{-r},10^{-r},10^{-r},10^{-s},10^{-s},10^{-s}]$

unless r=0, which means $Q = \text{diag}[0,0,0,10^{-s},10^{-s},10^{-s}]$

Figure 4-15 shows the position error history of a typical LKF run (D). Two transients of about 50 kilometers magnitude each are shown. The first corresponds to the initial condition error; the second results from the data outage between station passes.

The results of the testing of the LKF are best described by two additional conclusions.

1. The global linearization of the satellite dynamics used by the LKF is not appropriate when convergence in the presence of large initial errors is required. This is consistent with the common preference for the EKF over the LKF.

2. Improvements must be made in process noise modelling for convergence situations. Essentially this is advocating the use of the Gaussian Second Order Filter when there are large initial errors. This filter augments the predicted measurement covariance with a process noise-like term. This correction term depends on the estimate covariance and measures the probable linearization error.

4.3.5 EKF Properties

This section presents the results of an investigation of the effects of the a priori covariance and process noise strength selection on EKF performance. The coefficient of drag was estimated in all the tests, based on LKF experience.

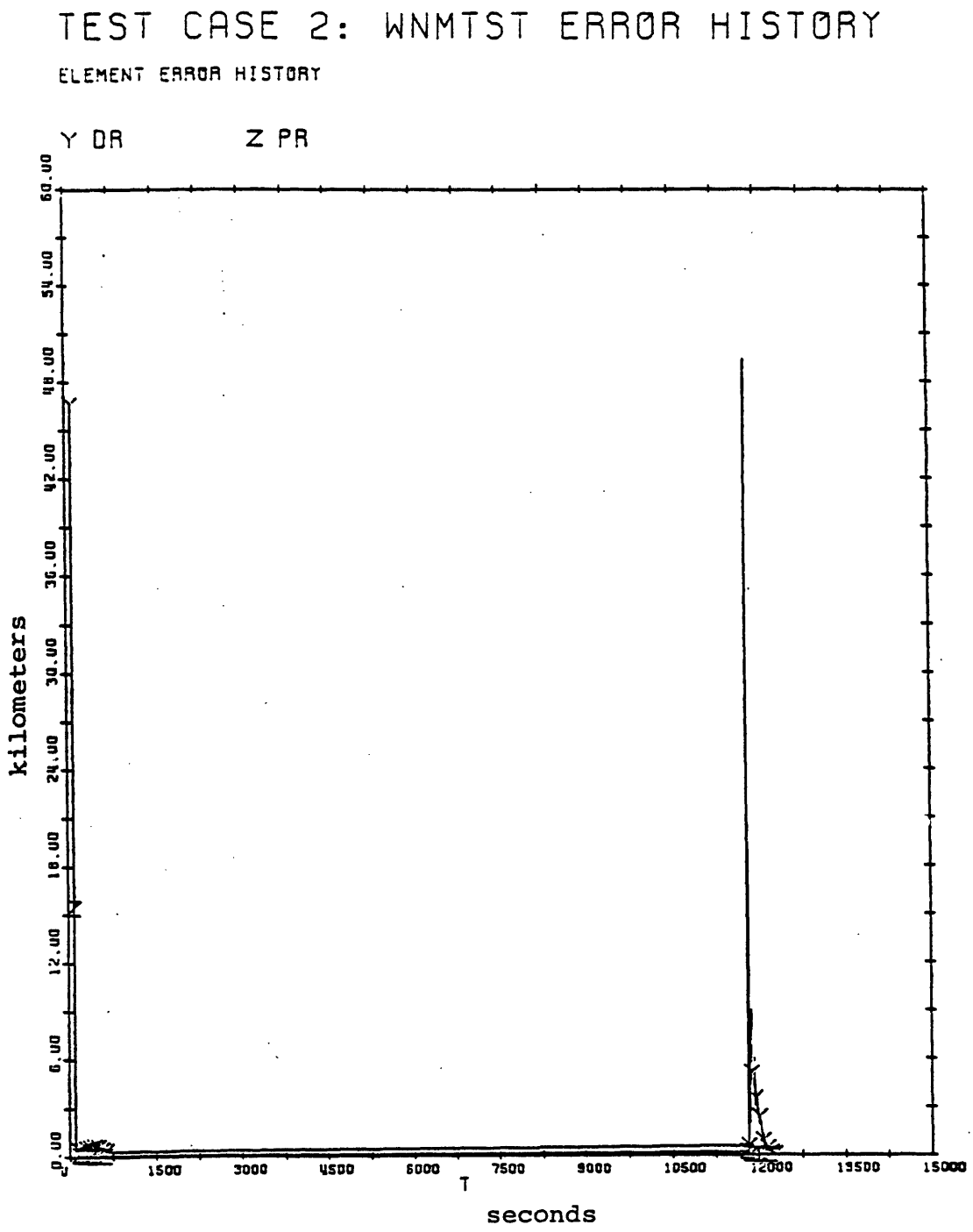

Figure 4-15. LKF Position Error History, Run D

The initial EKF runs showed the same poor (or worse) RMS prediction performance as corresponding LKF runs. This inability to select a process noise strength by trial and error for good performance led directly to the development and implementation of the process noise covariance transformation equations discussed in Appendix A. A utility routine for transforming a mean equinoctial a priori covariance to a corresponding position and velocity covariance was also implemented.

A total of eight EKF tests were conducted. The a priori covariance used was either the same as for the LKF (Option 1),

$$P_1 = \text{diag}[100.,100.,100.,10^{-6},10^{-6},10^{-6}]$$

or the transform of the SKF/ESKF a priori covariance (Option 2), given in equinoctial coordinates as

$$P_2 = \text{diag}[1.0,10^{-8},10^{-8},10^{-6},10^{-6},10^{-6}]$$

The process noise used was either one of a series of diagonal trials or else the transform of the second SKF process noise option. As in the LKF discussion above, the symbol [r,s] is used to denote a diagonal process noise

$$Q_1 = \text{diag}[10^{-r},10^{-r},10^{-r},10^{-s},10^{-s},10^{-s}]$$

Recall that the process noise strength used as Option 2 of the SKF tests is

$$Q_2 = [10^{-10}, 10^{-12}, 10^{-12}, 10^{-14}, 10^{-14}, 10^{-12}]$$

Note that this value of process noise was also used in all of the ESKF runs.

The options used for each of the eight EKF tests and the resulting performances are presented in Table 4-13.

These results support the following statements:

1. The dependence of EKF performance on the proces noise strength used is complex and unpredictable. This is probably due to the time varying nature of the linearization error being poorly modelled by a constant process noise strength. A Gaussian Second Order Filter would probably reduce this problem.

2. A process noise strength giving acceptable RMS prediction performance was selected [run F].

3. The transformation of the a priori covariance and the process noise strength from equinoctial coordinates to position and velocity coordinates gives acceptable RMS prediction performance. Both transformations appear to be required for best performance [runs G, H].

Table 4-13
EKF Parameter Test Results

Input Parameter	Test Runs							
	A	B	C	D	E	F	G	H
A Priori Covariance	1	1	1	1	1	1	1	2
Process Noise	off	[18,22]	[0,18]	[0,14]	[10,14]	[0,10]	SKF	SKF
Performance								
Radial RMS	2.2	5.3	2.2	10.2	11.5	0.31	3.0	0.99
Cross RMS	2.5	2.6	2.5	8.3	7.7	0.03	0.4	0.02
Along RMS	58.6	132.4	58.1	268.1	248.9	9.47	84.8	28.4

Notes: (i) the coefficient of Drag was estimated in all runs;

C_{D_o} = 2.0 (true value) $\sigma_c^2 = 10^{-6}$

(ii) A priori Covariance:

Option 1 = same as LKF

Option 2 = transform of SKF

(iii) Q ≃ SKF means option 2, the transformed process noise

Q ≃ [r,s] means Q = diag $[10^{-r}, 10^{-r}, 10^{-r}, 10^{-s}, 10^{-s}, 10^{-s}]$

unless r = 0, which means

Q = diag $[0, 0, 0, 10^{-s}, 10^{-s}, 10^{-s}]$

The EKF achieved best performance in runs F and H. Since these runs used very different methods for a priori covariance initialization and process noise calculation, a detailed comparison of their performance is of interest. Figures 4-16 and 4-17 show their dominant along track prediction errors. The growth of the along-track error for run H is much larger than for run F. This is due to the final semi major axis errors of 295 meters and 95 meters, respectively. The final errors in all of the Keplerian elements for runs F and H are shown in Table 4-14. These errors are consistent with the element errors for both runs over the last fifty observations; they are insensitive to the final filter output time.

The filtering histories for the semimajor axis and position errors for runs F and H are shown in Figures 4-18 through 4-21. The difference between the respective plots is striking. The plots for run F show apparent divergence and large errors for much of the observation span, with good convergence only in the latter part of the second station pass. The plots for run H show good convergence throughout the observation span, although the semimajor axis plot shows explicitly the final bias reported in Table 4-14. Both runs have similar position errors for the last fifty observations of the second pass: about 10 meters for run F and 5 meters for run H. It is interesting to observe how similar the semimajor axis and position error histories for run H are to the corresponding histories for the SKF and ESKF; this provides a good verification of the transformation method.

There are two explanations for the difference in the filtering histories for runs F and H. The first is a restatement of statement (1) above: a time varying process

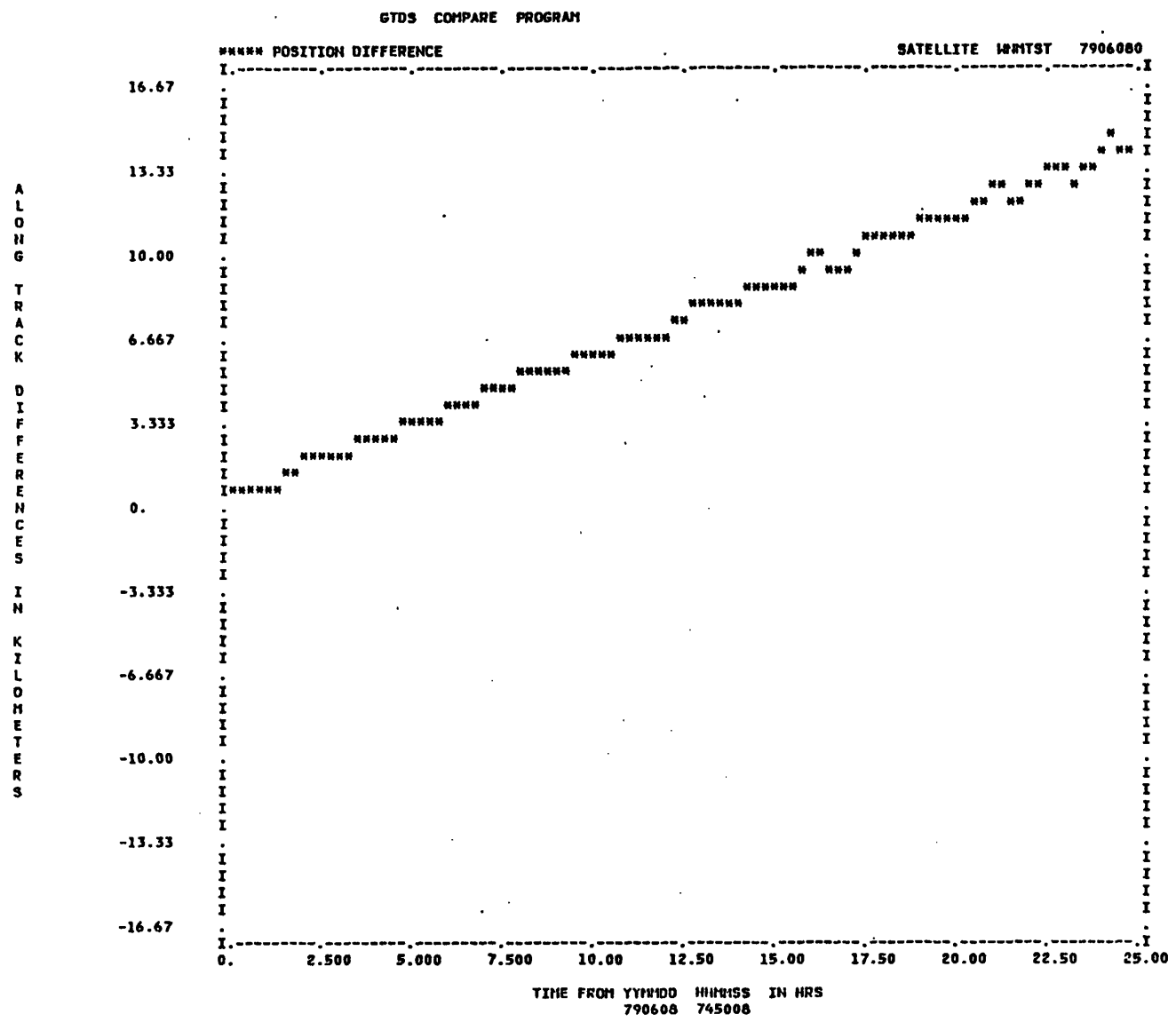

Figure 4-16. EKF Along Track Prediction Error, Run F

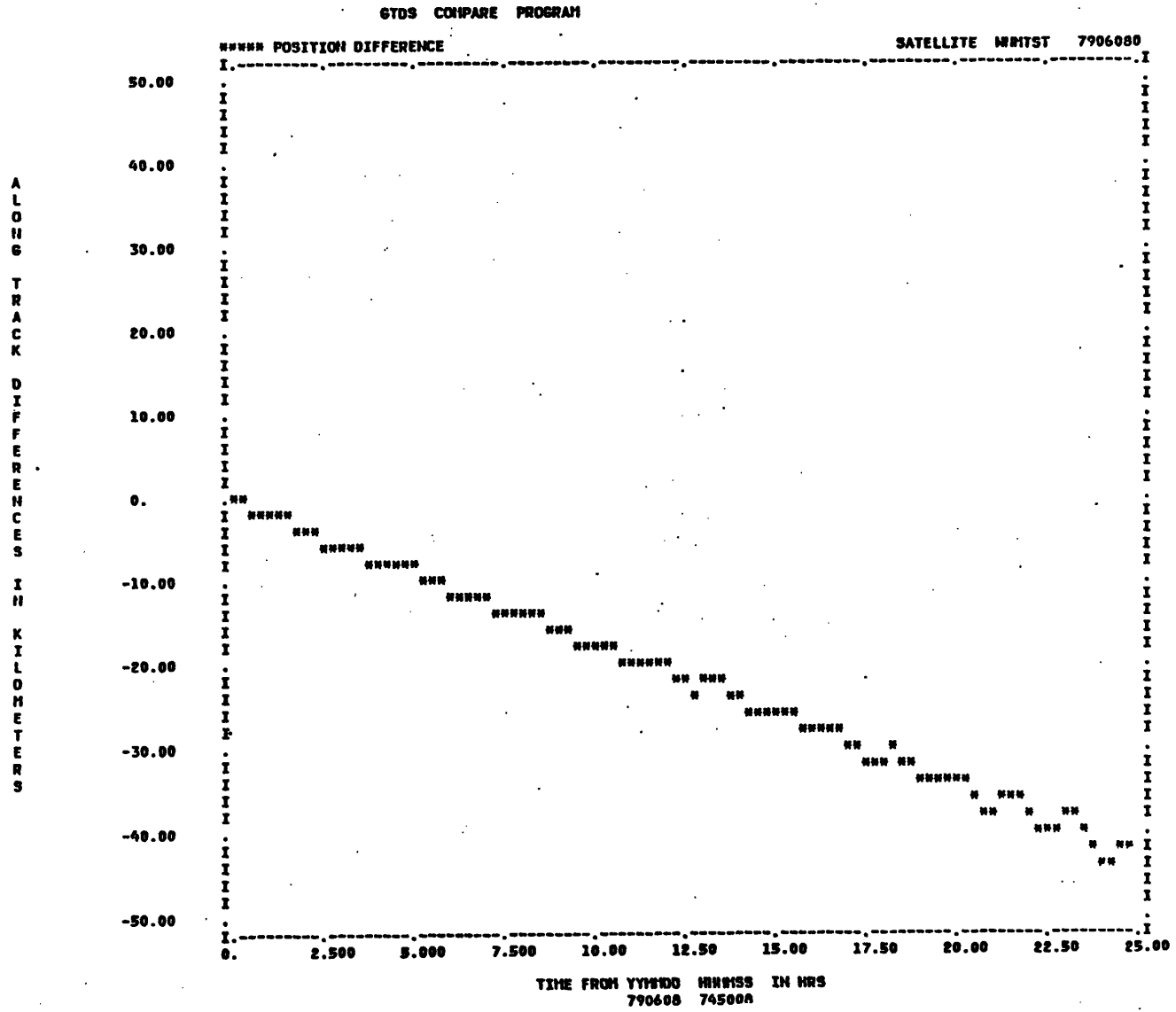

Figure 4-17. EKF Along Track Prediction Error, Run H

Table 4-14
Final Keplerian Element EKF Estimation Errors

Element	Run	
	F	H
a*	96.0	-295.0
e	-7.8E-6	-2.4E-5
i**	5.4	-2.7
Ω**	3.3	-2.0
ω**	-250.0	720.
M**	+240.0	-567.

* units are meters
** units are microradians

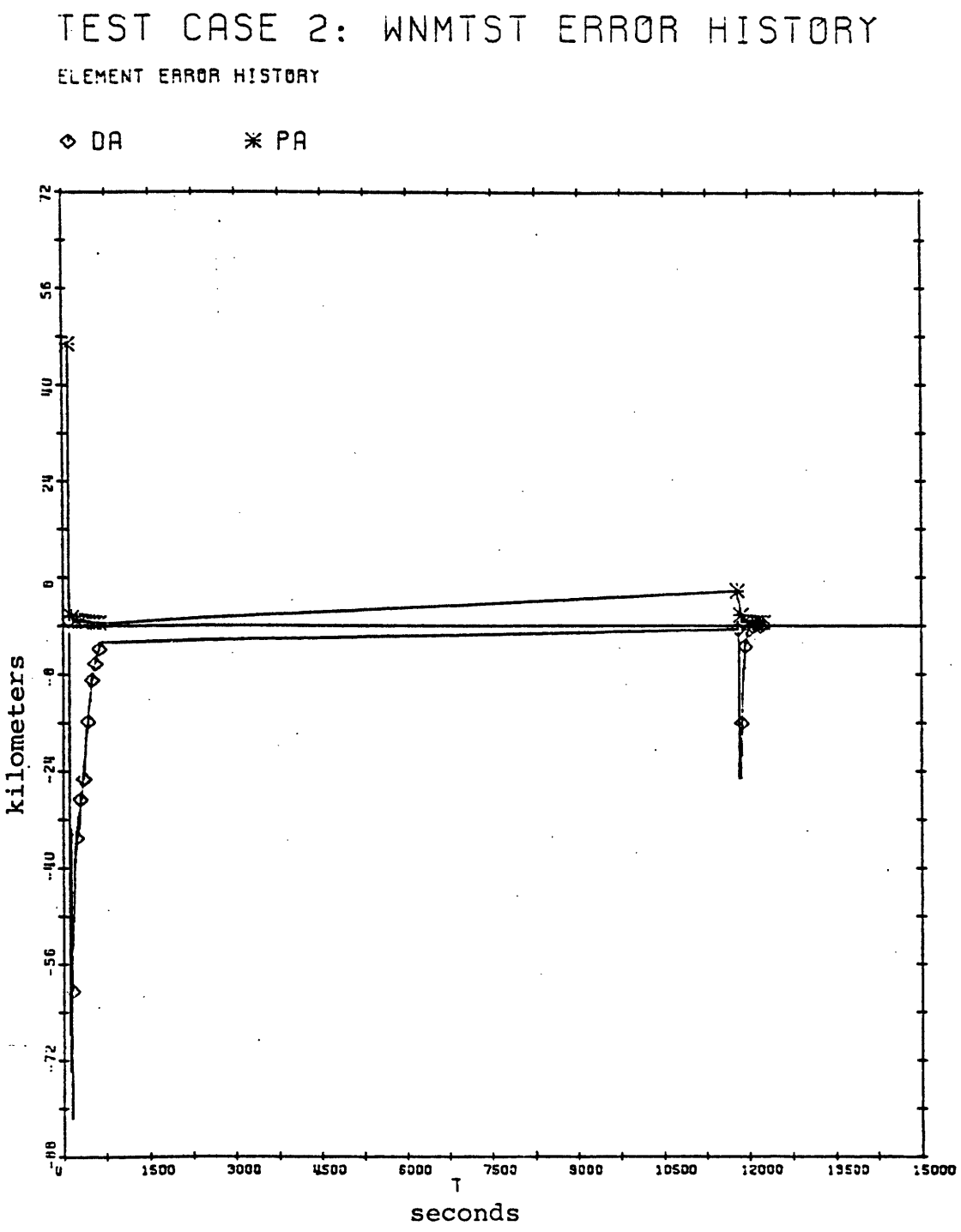

Figure 4-18. EKF Semimajor Axis History, Run F

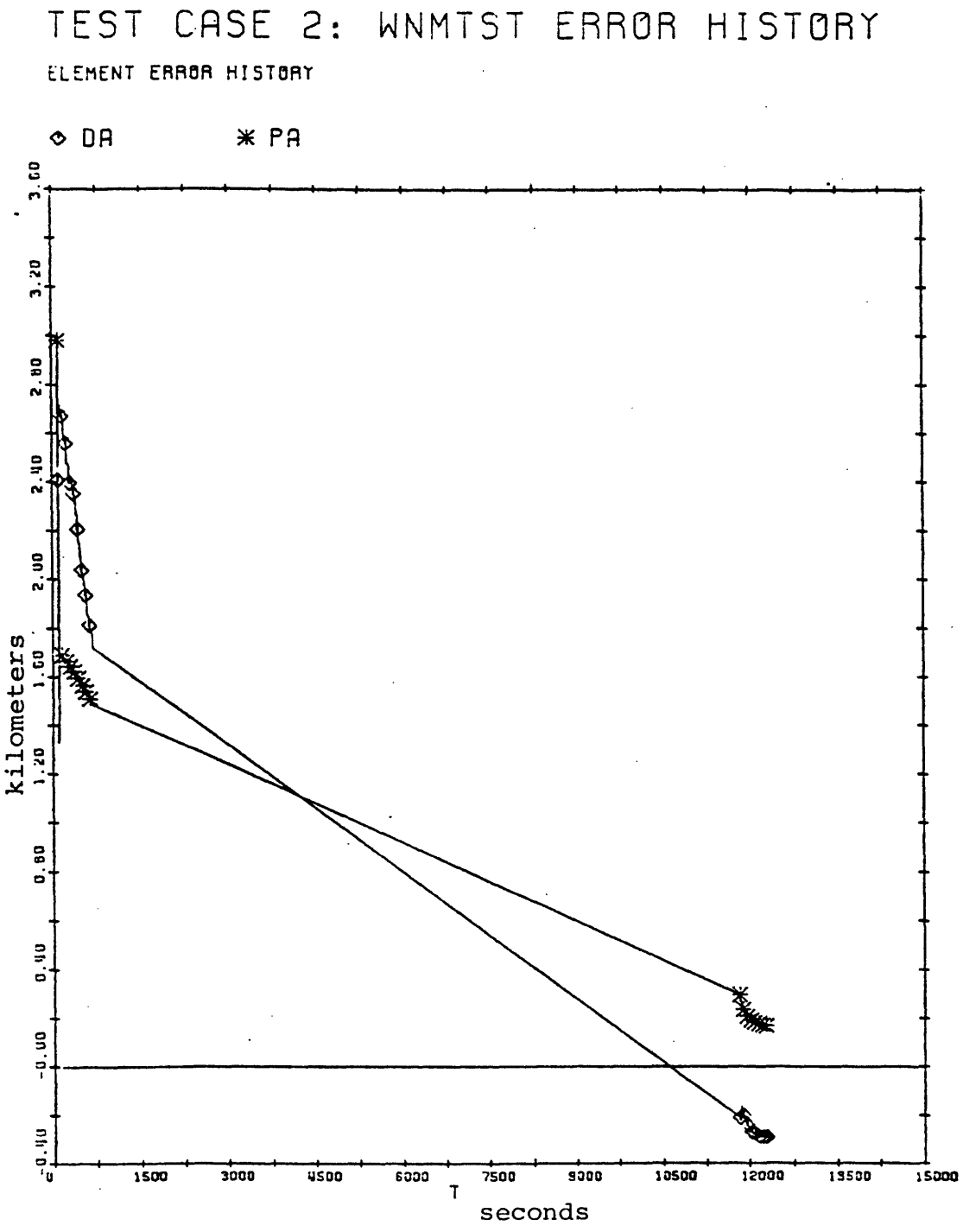

Figure 4-19. EKF Semimajor Axis Error History, Run H

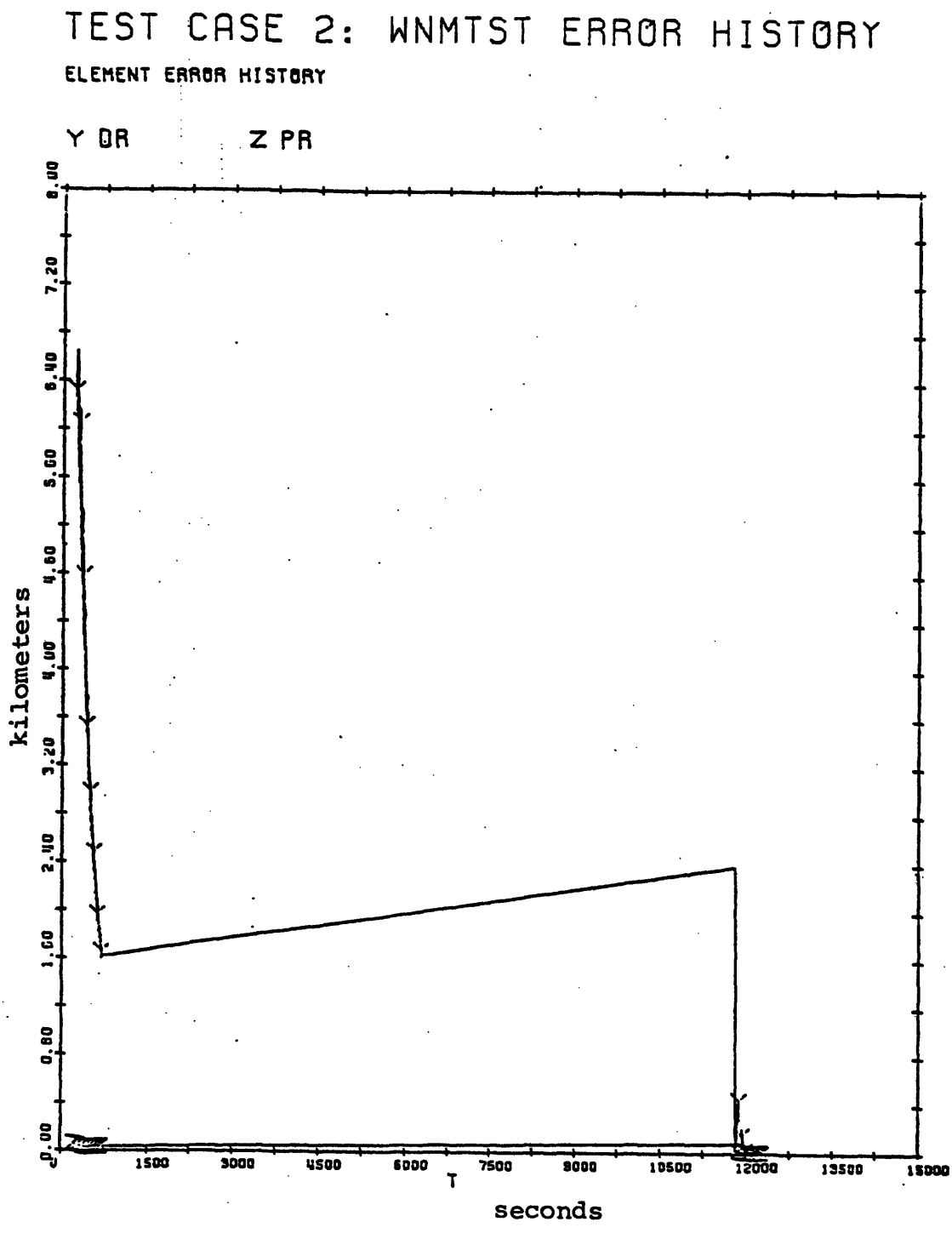

Figure 4-20. EKF Position Error History, Run F

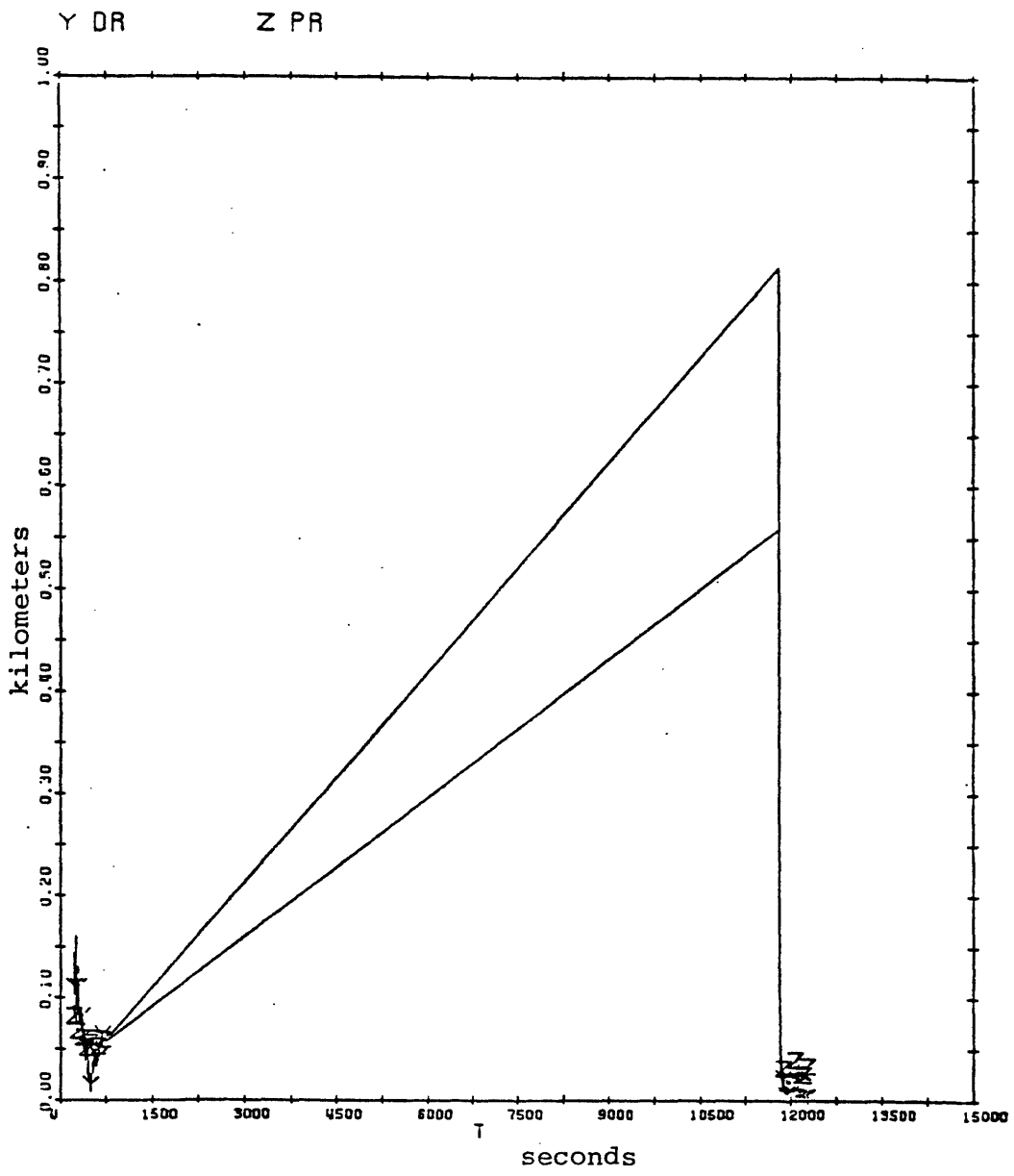

Figure 4-21. EKF Position Error History, Run H

noise is required to account the EKF linearization error. The process noise of run F probably strikes a balance between a value representative of the convergence requirement of the first station pass and the steady state requirement of the latter part of the second station pass. The second explanation has to do with the geometry of the process noise variables: the geometry of equinoctial variables is uniformly valid throughout a satellite's orbit, while the geometry of inertial position and velocity coordinates changes with the time varying constraint imposed by the current satellite location within the orbit. Both explanations are needed to account for the differences between runs F and H.

4.3.6 Test Case Two Performance Summary

This section summarizes the results of the previous four sections and provides efficiency estimates and comparisons with CDC and SDC baselines.

The DC runs were subjected to a slightly more strenuous test case. In addition to the initial condition errors given by use of the appropriate EARLYORB elements, the SDC and CDC were required to estimate the coefficient of drag, starting with an initial estimate of 2.1 as compared to the truth value of 2.0. Both runs converged to a final estimate of 2.08, illustrating the difficulty in short arc estimation of the drag coefficient. Two factors allow comparison of these DC results with the filter tests. First, both DC estimates give respectable predictions against the Cowell Truth. And second, the drag coefficient estimate varies over a range well including the true value over the course

of the five iterations required for convergence. Thus the final drag coefficient estimate apparently gives the best fit.

Table 4-15 lists the results of the best filter run from each of the sections above for comparison with the other filters and with CDC and SDC. The runs are identified by the appropriate letter from each section; two runs are listed for the EKF, reflecting the two essentially different methods for process noise and a priori covariance choice. These results indicate that the SKF and ESKF have converged faster than the LKF and EKF for this test case.

The results of timing tests are given in Table 4-16. The times recorded are the CPU times required for processing the observations from the two station passes. These timing estimates should be conservative for two reasons:

1. The observation span was very short, only 3.5 hours, compared with typically allowable integration grid lengths of up to 1 day; since much of the cost of semianalytical ephemeris generation is due to integration grid force evaluations and short periodic coefficient computations, any increase in grid length will further increase the timing advantage of the SKF and ESKF.

2. The complexity of a semianalytical force evaluation allows more room for efficiency gains by model truncation or code optimization than does a comparable Cowell force evaluation. Most of the present code for semianalytical satellite theory in the RD GTDS testbed was implemented primarily

Table 4-15
Test Case Two Performance Summary

Performance	Test Runs						
	CDC	SDC	SKF (F)	ESKF (G)	LKF (J)	EKF (F)	EKF (H)
Radial RMS	.030	.051	.185	.174	2.79	.313	.986
Cross RMS	.005	.007	.371	.019	.885	.033	.015
Along RMS	.725	.367	1.145	.500	31.9	9.47	28.4

Table 4-16
Test Case Two Timing Estimates

Filter Run	CPU Execution Time*
SKF B	0:30.97
SKF C	0:29.33
SKF D	0:15.49
ESKF G	0:17.58
LKF H	0:38.69
EKF F	0:40.90

* units are minutes:seconds

to verify accuracy, and not to achieve operational system efficiency. A preliminary indication of this is given by the two force model options tested for the SKF. The timing impact of the position and velocity interpolator for the SKF and B_1 matrix calculation for the ESKF are also given.

The results of this test case give a very promising indication of SKF and ESKF performance. Further testing is required.

4.4 Conclusions

This chapter accomplished several important tasks:

1. A survey of the problems involved in SKF and ESKF testing and performance evaluation was presented, and a resulting test methodology was detailed;

2. Results indicating successful software validation were presented;

3. The transformation equations for the a priori covariance and process noise were verified to result in corresponding filter histories when employed;

4. The ESKF was shown to achieve position estimates with accuracy equal to that of the conventional EKF for the test case considered.

The principal simulated data test case discussed in this chapter was a short-arc case measuring the convergence properties of the SKF and ESKF. Of greater importance in many applications is the steady state filtering accuracy in the presence of real world errors. The real data test case of the next chapter provides an excellent test of this issue.

Chapter 5
THE REAL DATA TEST CASE

This chapter presents the results from the application of the EKF and the ESKF to the real observational data of a low altitude earth satellite. The data had been obtained previously from the Aerospace Defense Command (ADCOM) for use in orbit determination studies at CSDL. This test case is used to discuss the effects of model errors on steady state filter performance.

The organization of this chapter is similar to that employed in Chapter 4. The formulation of the test case is described first, including some interesting results on the GEM 9 gravity field employed by GTDS. The second section discusses the actual filter results; only the EKF and ESKF are examined, based on the results from Chapter 4. The final section summarizes the important results.

5.1 Test Case Formulation

Nine days of ADCOM tracking data provided the basis for the filter tests presented in this chapter. The data represents the tracking history for Space Vehicle 10299 (SV10299) in the ADCOM catalog over the time period from August 30, 1977 to September 7, 1977. ADCOM provided CSDL with the observational data, a tracking network description, and a history of geomagnetic and solar activity for use in orbit determination tests. P. Cefola [19] conducted a series of batch estimation tests using this data, comparing SDC and CDC performance. The filter test case formulated here was based on his experience.

The data employed did not include a satellite description or satellite initial conditions. In addition to addressing these two issues, this test case formulation section discusses the modelling of the drag and gravitational forces, the observational data, and the question of filter performance measurement.

Some knowledge of the satellite is required in order to estimate its aerodynamic characteristics for correct drag force modelling. The satellite can be tentatively identified as the COSMOS 947 satellite, based on its orbital characteristics [19]. Confirmation is offered by the fact that reasonable drag coefficient estimates result when the COSMOS 947 mass and area data [40] are used.

The results from Chapter 4 indicate that the RD GTDS EARLYORB program gives satisfactory initial conditions for EKF tests, and that the simple EPC iteration (4-1) provides an adequate set of corresponding mean elements for ESKF initialization. The osculating EARLYORB elements and the corresponding mean EPC elements used for this test case are shown in Table 5-1. Once again the EPC procedure converged very quickly. This table also presents the estimated errors in the Early Orbit elements, computed as the difference between the EARLYORB-based elements and the best CDC and SDC estimates generated during Cefola's work. Notice that both the initial position errors and the semimajor axis error are quite large, so that this test case will provide another interesting convergence problem. The estimated errors in the Early Orbit mean equinoctial elements resulted in the choice of a mean equinoctial a priori covariance for use in the ESKF tests. The covariance transformation equation

Table 5-1
Osculating and Mean Filter Initial Conditions

Early Orbit Keplerian Elements

	Osculating	EPC Mean
a	6630.816	6622.458 (km)
e	0.008686	0.008572
i	72.826	72.837 (deg)
Ω	126.216	126.211 (deg)
ω	71.332	67.393 (deg)
M	96.966	100.432 (deg)

Truth Minus Early Orbit Perturbations

	Osculating		Mean
Δx	15.33 (km)	Δa	13.36 (km)
Δy	39.70 (km)	Δh	0.0002
Δz	38.76 (km)	Δk	0.0013
ΔVx	43.6 (m/s)	Δp	0.0048
ΔVy	4.5 (m/s)	Δq	0.0035
ΔVz	2.2 (m/s)	$\Delta \lambda$	0.0032 (rad)
$\|\|\Delta \underline{r}\|\|$	57.5 (km)	$\|\|\Delta \underline{r}\|\|$	57.4 (km)

Mean Equinoctial A Priori Covariance

$$\underline{P}_0 = \text{diag}\left[100, 10^{-7}, 10^{-7}, 10^{-6}, 10^{-6}, 10^{-6}\right]$$

Position and Velocity Transformed Covariance

11 12 13	0.577872937D+02	-0.247811762D+02	0.271083238D+02
14 15 16	-0.910724194D-02	-0.113578011D-01	0.330172395D-01
22 23 24	0.935358494D+02	0.233366991D+02	0.361921129D-01
25 26 33	-0.266885691D-01	-0.429364632D-01	0.128902932D+03
34 35 36	0.694130954D-01	-0.926367328D-01	0.359536922D-01
44 45 46	0.111007468D-03	-0.140631562D-04	0.258469178D-04
55 56 66	0.100737766D-03	-0.383030973D-05	0.495533978D-04

(4-2) was used to compute the corresponding osculating position and velocity a priori covariance for use with the EKF. These covariances are listed in Table 5-1.

The many filter tests presented in Chapter 4 indicate that the correct choice of a process noise model is essential for filter performance. The desire to relate the process noise model of this test case to the probable real-world force model errors led to the derivation and application of the algorithms presented in Appendix A. The calculations detailed there led to a process noise strength of

$$Q = \text{diag}\,[2E\text{-}3, 2E\text{-}16, 2E\text{-}16, 2E\text{-}17, 2E\text{-}17, 3E\text{-}16]$$

for use with the ESKF. The process noise used with the EKF was obtained by use of the transformation equations (A-18).

RD GTDS contains two density model options: either the Jacchia 1971 Density Model or the 1964 Harris-Priester Atmosphere Density Model can be used. Based on operational considerations [41], the simpler Harris-Priester Density Model was selected.

The Harris-Priester Density Model uses different density tables according to the current value of the mean solar radiation flux, $\bar{F}_{10.7}$. Table 5-2 presents values for the solar radiation flux and the daily average value of the geomagnetic index, A_p, for each day between August 30, 1977 and September 4, 1977. Evidently there were only small variations in either parameter, so only small changes

Table 5-2
Solar Radiation Flux and Geomagnetic Index History

Day in 1977	$F_{10.7}$	A_p
Aug 30	85.5	4.9
Aug 31	84.7	6.0
Sept 1	83.1	4.1
Sept 2	84.2	4.1
Sept 3	87.2	8.4
Sept 4	84.2	8.0

in the atmospheric density profile should have occurred during the tracking period of interest. Notice, however, that the average geomagnetic index does increase in the second three day span, reflecting a small geomagnetic storm and an accompanying increase in the atmospheric density. The Harris-Priester density table for $\bar{F}_{10.7}=100$ was used. The difference between the tabular value for the solar radiation flux and the actual values was one motivation for estimating the coefficient of drag; uncertainties in the satellite's mass and aerodynamic area provided another. The filter tests used an initial value of 2.0 for the coefficient of drag and an a priori variance of 0.333, reflecting the approximately 20% uncertainty in the drag force model.

All of the filter tests used the GEM 9 Gravity Model [36], which is the most recent gravity model available in the CSDL version of RD GTDS. A truncated version of this gravity model was used, with only terms through eighth degree and order retained. The gravity model was truncated for two reasons:

1. Most of the tracking data was not of very high accuracy, and so did not warrant using a very high precision force model; and

2. Batch estimation tests [19] indicated that use of the truncated field gave better predictions than when the full (21x21) field was used.

The filter test force models also included the third body gravitational forces due to the moon and the sun. Solar radiation pressure was neglected due to the low altitude of the satellite.

Each filter test processed the observations recorded on August 30, 1977. A total of ten radar stations tracked the satellite that day, taking 576 observations. Range, azimuth, elevation, and range rate observations were taken. The observations were usually not of very high quality. Typical standard deviations for the observations were: between 30. meters and 1.5 kilometers for range, between 0.01 degrees and 0.04 degrees for azimuth and elevation, and between 1.0 meters per second and 10.0 meters per second for the range-rate observations. Table 5-3 gives an explicit account of each satellite station pass, listing the orbit it occured in, the average satellite true anomaly during the pass, the elapsed time since the last station pass, and the number of observations taken during the current pass. This data will be important for analyzing the filter performance results presented below.

In Chapter 4, filter performance was measured by comparing a filtered ephemeris with the simulation truth ephemeris. In a real data orbit determination problem, the truth ephemeris is the actual satellite position and velocity history, which is unknown. A truth ephemeris was defined for this real data test case by using the converged ephemeris estimated by a long arc CDC. A consistency check for this ephemeris was provided by the corresponding SDC converged ephemeris. The CDC and SDC used the three days of tracking data from August 30, 1977 through September 1, 1977. Table 5-4 summarizes the truth model used by the CDC for generating the real data truth ephemeris. The corresponding SDC truth model is given in Table 5-5. The Semi-analytical truth ephemeris agrees excellently with the

Table 5-3
Real Data Observation History
Satellite SV10299 epoch 30 August 1977 0:0:0.0 hours

Orbit	Station	True* Anomaly	Data** Outage	Number of Observations	Orbit	Station	True* Anomaly	Data** Outage	Number of Observations
1	ASCQ	128	---	8	11	NAVQ	327	0:01	6
1	CBDF	355	0:54	124	11	THUF	15	0:10	36
1	ANTQ	95	0:22	12	12	NAVQ	328	1:18	6
2	CLET	35	1:11	36	12	THUF	27	0:12	36
2	NAVQ	82	0:11	6	13	THUF	33	1:30	20
2	EGLQ	87	0:09	33	13	FYLQ	62	0:06	36
3	NAVQ	82	1:27	3	14	THUF	35	1:22	28
4	CLET	51	1:20	28	15	CLET	353	1:21	24
7	CBDF	70	4:33	4	15	THUF	42	0:08	28
8	FLYT	355	1:14	12	16	ASCQ	136	0:22	12
9	FLYF	7	1:32	12	16	CLET	24	0:59	32
11	EGLQ	321	2:48	9	16	THUF	50	0:04	32

* Angles are in degrees
** Times are hours and minutes

Table 5-4
Real Data Test Case Truth Model

satellite: SV10299

epoch: August 30, 1977, 0 hrs., 0 min., 0 sec.

reference frame: Mean of 1950

coordinates:

Position and Velocity		Keplerian	
x	= 3544.2402 (km)	a	= 6644.2294 (km)
y	= -5517.4040 (km)	e	= 0.009311916
z	= 1140.6632 (km)	i	= 72.982366 (deg)
Vx	= 2.655753 (km/sec)	Ω	= 125.76742 (deg)
Vy	= 0.115046 (km/sec)	ω	= 68.576733 (deg)
Vz	= -7.260209 (km/sec)	M	= 99.994258 (deg)

drag coefficient: $C_D = 1.3421078$

area: $A = 6.1\ (m^2)$

mass: m = 5700. (kg)

density model: 1964 Harris-Priester Atmosphere
($F_{10.7} = 100$)

gravity field: 8x8 (GEM-9)

third bodies: Moon, Sun

integrator: 12th order Cowell/Adams predictor corrector

step size: 45.0 seconds

Table 5-5
Real Data Test Case Semianalytical Truth Model

satellite: SV10299

epoch: August 30, 1977, 0 hrs., 0 min., 0 sec.

reference frame: Mean of 1950

coordinates:

Mean Equinoctial	Mean Keplerian
a = 6635.8109 (km)	a = 6635.8109 (km)
h = -0.00139098	e = 0.00979471
k = -0.00961044	i = 72.969833 (deg)
p = 0.60004557	Ω = 125.770814 (deg)
q = -0.43230204	ω = 65.360707 (deg)
λ = 294.359281 (deg)	M = 103.22775 (deg)

drag coefficient: $C_D = 1.8408701$

area: $A = 6.1\ (m^2)$

mass: m = 5700. (kg)

density model: 1964 Harris-Priester atmosphere
($F_{10.7} = 100$)

gravity field: 8x8 (GEM-9)

third bodies: Moon, Sun

integrator: 4th order Runge-Kutta

step size: 43400. sec ≈ 1/2 day

8x0 averaged potential
second order $J_2^2\ e^1$ and Drag-J_2 coupling
AOG lunar-solar single averaged (parallax=8,4), e^4

zonals (8x0), e^2
m-dailies (8x8), e^2_1
SPG tesserals (8x8), e^1
drag 3 frequencies $_0$
second order $J_2^2\ e^0$
second order J_2-m-daily coupling (8x8), e^2

Cowell truth ephemeris; this is shown quantitatively in Table 5-6, which gives the RMS position and velocity differences between the two ephemerides for the three day fit span and for the three day predict span. The agreement between the two ephemerides is quite good.

Examination of Tables 5-4 and 5-5 shows that both of the truth models also use the truncated 8x8 gravity model instead of the full 21x21 field. The reason is the same as for the filter tests: the truncated field gives better prediction performance. Table 5-7 presents the results of five tests conducted in the study of this gravity model anomaly. The setup for each test was the same as for the CDC and SDC truth models, with only the gravity model changing. The coefficient of drag was estimated in all tests. The RMS values shown are the weighted RMS observation residuals for the given three day span; the predict span is from September 2, 1977 through September 4, 1977. The prediction performance degradation can be seen by comparing the first and third tests or the second and fourth tests. The parallel CDC and SDC tests show that the phenomenon is not satellite theory dependent: it is a force model anomaly. The satellite SV10299 was in a 201x331 kilometer orbit and had an 89.93 minute period; it made sixteen revolutions per day. Calculations indicated that the resulting resonance with the sixteenth order geopotential harmonics was very sharp: long periodic motions at approximately 960 times the orbital period were introduced. The last test presented in Table 5-7 indicates that the resonant geopotential coefficients (the coefficients of sixteenth order and degree varying from sixteen through twenty-one) account for the degradation of the prediction performance.

Table 5-6
Semianalytical and Cowell Truth Ephemeris
RMS Differences

Fit Span Differences

August 30, 1977 to September 1, 1977

	POSITION RMS (KM)	VELOCITY RMS (KM/SEC)
RADIAL	0.44604D-02	0.11352D-04
CROSS TRACK	0.19394D-01	0.22629D-04
ALONG TRACK	0.11655D-01	0.51249D-05
TOTAL	0.23062D-01	0.25830D-04

Predict Span Differences

September 2, 1977 to September 4, 1977

	POSITION RMS (KM)	VELOCITY RMS (KM/SEC)
RADIAL	0.43556D-02	0.11831D-03
CROSS TRACK	0.31077D-01	0.36222D-04
ALONG TRACK	0.10166D+00	0.53005D-05
TOTAL	0.10639D+00	0.12385D-03

Table 5-7
GEM 9 Gravitational Coefficient Model Anomaly Data

Run Type	Gravity Field	Fit Span RMS	Predict Span RMS	Drag Coefficient
CDC	8x8	1.63	18.41	1.842
SDC	8x8	1.46	19.06	1.841
CDC	21x21	1.61	57.40	1.891
SDC	21x21	1.34	53.45	1.889
SDC	8x8 plus (16,16) -(21,16)	1.36	55.75	1.883

Notes: 1. GEM 9 Gravity coefficients were used.

2. The drag coefficient was estimated in all runs.

3. All runs included drag effects and lunar-solar third body perturbations.

There are several possible explanations for these results:

1. The sixteenth order GEM 9 geopotential coefficients may be in error;

2. Additional sixteenth order geopotential coefficients beyond the sixteenth through twenty first degree coefficients may be required by the sharpness of the resonance and the low altitude of SV10299;

3. The Harris-Priester Density Model may be inappropriate for use with the GEM 9 Gravity Model in this sharp resonance situation; and

4. The coefficient of drag estimated in the tests with poor performance may have been biased, either by not using a time varying model, or by using the Harris-Priester density table for $F_{10.7}=100$, which may be too far from the real values of about 85.

It is interesting to consider [19] two facts about the GEM 9 gravity modelling process [36]:

1. The GEM 9 coefficient solution did not use tracking data from any 16 rev/day satellites; the solution did use several satellites with orbital frequencies ranging from 12 revs/day to 15 revs/day;

2. The coefficient error estimates produced by the GEM 9 solution showed a sharp increase for the 16th and higher order coefficients, in comparison with the error estimates for the 12th order through 15th order coefficients.

While these results make the possibility of errors in the sixteenth order GEM 9 geopotential coefficients at least plausible, clearly more work is required before any credible conclusions can be drawn. In particular, the whole question of atmospheric modelling must be carefully investigated, both in terms of general model errors and in terms of the effects of the small geomagnetic storm that occured during the predict span.

5.2 Real Data Test Case Filter Results

This section presents the results of several tests examining the performance of the EKF and ESKF for the real data test case formulated above. These results are of interest for several reasons:

1. Real observational data of a low altitude earth satellite was processed, so that real-world errors in the observations, the gravitational and drag force models, and the event times and coordinate transforms are present;

2. Enough data was processed so that the filters achieved a steady state, in spite of the large initial errors; and

3. The process noise strength was computed using the model developed in Appendix A, so that the success of that model can be judged from the filter histories.

The results from five filter tests are reported in this section. Four of the tests are ESKF tests; there is only one EKF test, reflecting the fact that the a priori covariance and the process noise have already been selected. The four ESKF tests investigate the effects of the integration grid length and the force model on the performance of the ESKF for this long arc test case. These issues were investigated in Chapter 4 for the short arc test case. The results presented there indicate that ESKF accuracy has a slight dependence on certain force model truncations and a much greater dependence on the integration grid length used; these issues were discussed in Chapter 4 in terms of the question of whether or not to update the nominal trajectory after a station pass. The ESKF tests in this section were designed to extend those results to a long arc case.

The results from all of the filter tests are shown in Table 5-8. This table presents the force model truncation and integration grid length options selected for each ESKF run, the final coefficient of drag estimate for each run, and the RMS trajectory error statistics for the difference between a one day filter estimate prediction and the CDC truth ephemeris. These results support the following statements:

Table 5-8
Real Data Filter Performance Results

Input Parameters	ESKF Test Runs				The EKF Test Run
	A	B	C	D	
1 Force Model	1	1	1	2	
2 Integration Grid Length	43200.	29000.	9600.	21000.	10.
Performance					
Radial RMS*	0.040	0.053	0.056	0.046	0.047
Cross RMS*	0.072	0.079	0.81	0.057	0.048
Along RMS*	0.405	1.073	1.646	0.262	0.507
Estimated Drag Coefficient	1.89	1.99	2.06	1.88	1.93

* units are kilometers

Notes:
1. The B_1 matrix was computed in all ESKF runs.
2. All filter tests included drag coefficient estimation.
3. The EKF used the transformed initial conditions and process noise of the ESKF runs.
4. The ESKF force model options are:
   option 1: same as Semianalytical Truth, Table 5-5
   option 2: improves on option 1 by taking all first order short periodics to fourth order in e, and including J_2-drag and drag-drag coupling in the AOG.

1. The accurate estimation of the coefficient of drag is essential for ensuring the prediction accuracy of a low altitude satellite orbit. It can be shown that a five percent change in the drag coefficient can produce along track errors of several kilometers after one day;

2. Neglecting the along track errors as being contaminated by drag coefficient-induced errors, then all of the filter tests show equivalent performance to within the tolerance of the SDC and CDC truth ephemeris agreement (see Table 5-6);

3. Each of the filters essentially reproduces the estimation results of the CDC truth ephemeris.

Six aspects of the filter test runs of Table 5-8 are now considered in detail.

5.2.1 The Effects of Drag Coefficient Errors

The effects of drag coefficient errors can be assessed either directly or indirectly. A direct assessment can be derived by considering how the effect of a semimajor axis rate propagates through the mean motion, into a resulting perturbation in the mean anomaly; a perturbation in the mean anomaly maps directly into an along track error.

An indirect assessment of the effects of a drag coefficient error is presented here, by comparing the ESKF run D with the EKF run. Figures 5-1 and 5-2 show the along track

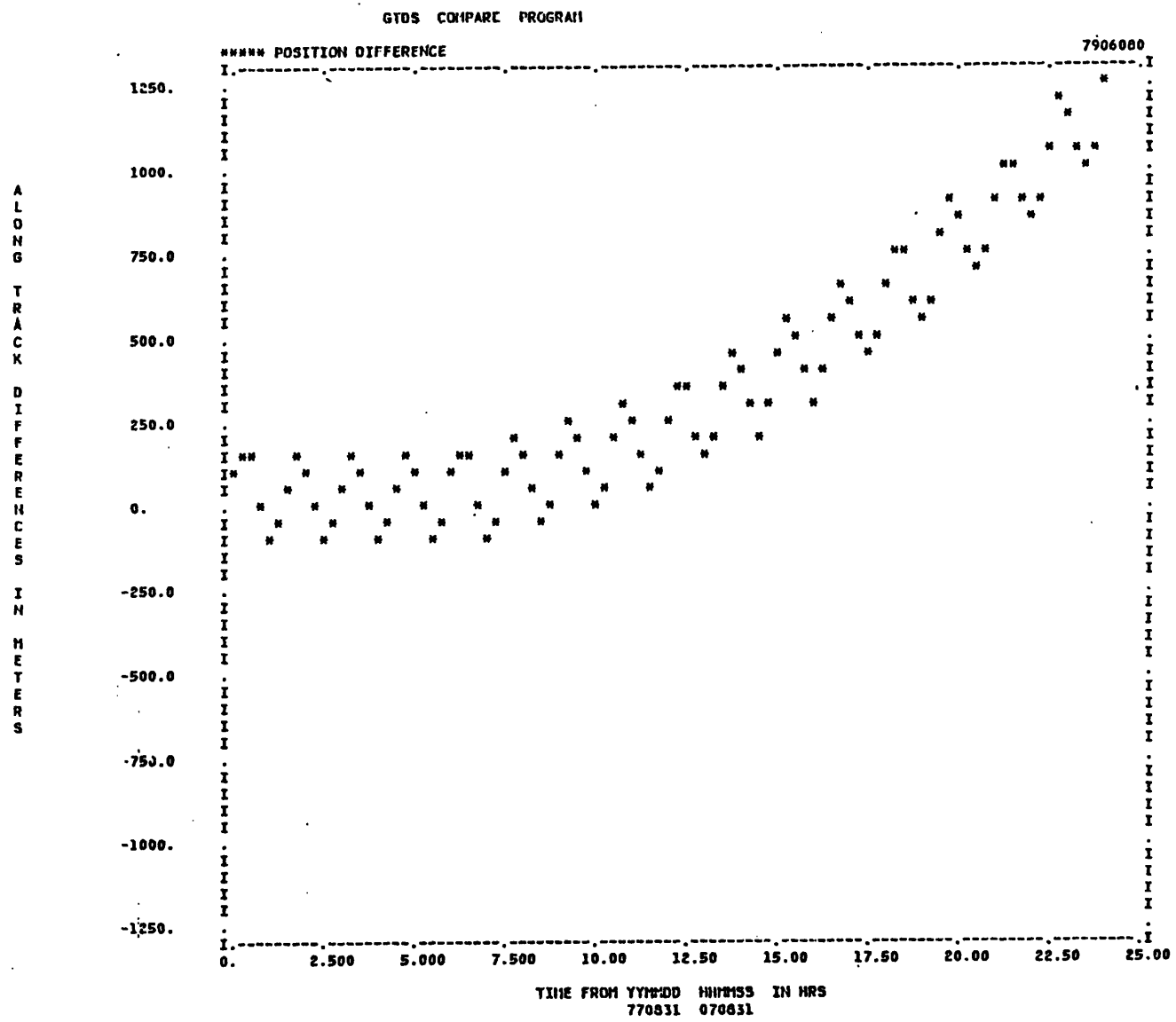

Figure 5-1. EKF Along Track Errors, Real Data Test Case

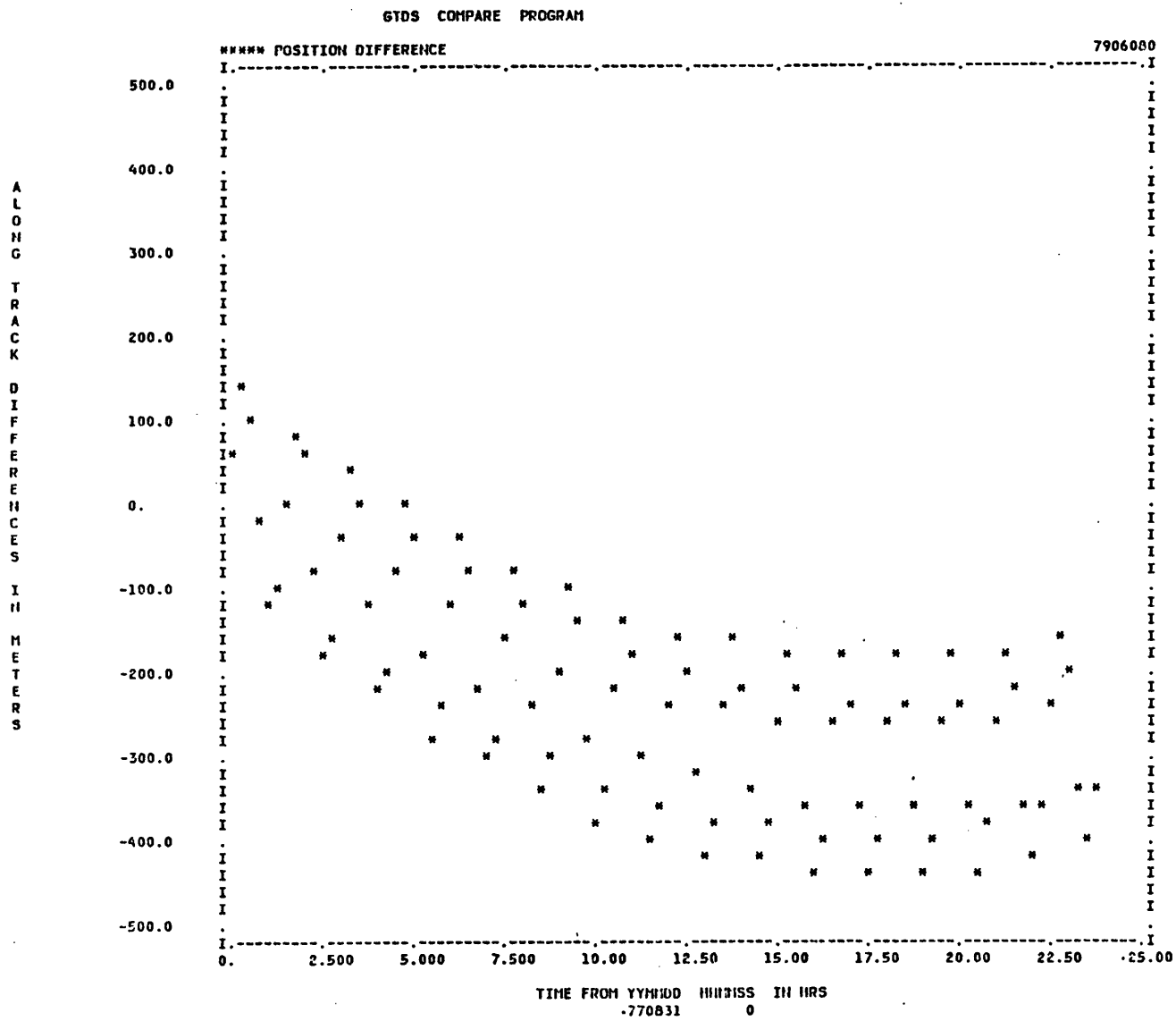

Figure 5-2. ESKF Run D Along Track Errors, Real Data Test Case

differences between the CDC truth ephemeris and the EKF and ESKF filter predictions for August 31, 1977. The along track differences are signed, and are computed as the CDC truth minus the given filter prediction. These two figures imply a total along track error between the EKF and ESKF of 1.5 kilometers after one day, growing from an essentially zero difference. Some of this error is due to initial orbital element differences between the EKF and ESKF predictions; these initial orbital element differences and the difference between their respesctive drag coefficient estimates are given in Table 5-9. All of the differences are very small.

The critical differences for along track error growth are the semimajor axis error and the drag coefficient error. A simple two body dynamical analysis shows that the semimajor axis error accounts for about 300 meters of the final 1.5 kilometer trajectory difference; the remainder is accounted for by semimajor axis error rate induced by the coefficient of drag difference. Notice that the drag coefficients differ by only three percent, which is a quite acceptable error in a drag coefficient estimate. These results justify essentially neglecting the along track RMS results in Table 5-8 when comparing the performance of various filters.

5.2.2 Preliminary Timing Results

The results of Table 5-8 indicate that the EKF and ESKF recover from large initial errors to essentially reproduce the CDC truth ephemeris estimates. This conclusion is interesting for two reasons:

Table 5-9
EKF and ESKF Element Differences

Element	Difference /EKF-ESKF D/
a	2.1 meters
e	4×10^{-7}
i	0.7 microradians
Ω	1.6 microradians
λ	0.5 microradians
C_D	0.05 = 3%

Table 5-10
Real Data Test Case Timing Estimates

Filter Run	CPU Execution Time*
ESKF B	0:17.10
ESKF D	0:25.58
EKF	1:57.24

* units are minutes:seconds

1. CDC and SDC tests starting with the same EARLYORB based initial elements and constrained to process the whole day of observations in one batch could not converge; convergence can be obtained when shorter arcs of observational data are processed first to reduce the size of the initial errors.

2. The second reason has to do with efficiency. The filter runs required only one pass through the data and started from large initial errors; the CDC truth run required four passes and started from much smaller initial errors.

It appears that the filters can achieve about the same accuracy as the batch differential corrections estimators with increases in efficiency and without sacrifice of any convergence properties.

Timing estimates for the EKF and two ESKF tests from Table 5-8 are presented in Table 5-10. The times given are based on the GO step CPU times required by the respective filter tests for processing the observations. The ESKF tests allow comparison of the timing requirements of the two force model options used. The CPU times shown indicate that the ESKF tests are between four and seven times as efficient as the corresponding EKF test. This estimate of the efficiency advantage of the ESKF should be conservative, as indicated in Chapter 4.

5.2.3 ESKF Integration Grid Length Selection

This section discusses the effect of the integration grid length on ESKF performance. The results from the short arc test case of Chapter 4 show that shorter integration grid lengths do not necessarily yield improved performance. An upper bound on the integration grid length is imposed by the bounds on the region of validity for the linearization assumption required by the ESKF.

Figures 5-3 through 5-7 show the filter histories of the osculating semimajor axis error for each of the filter tests presented in Table 5-8. The variable DA is the actual error, while the variable PA is a three standard deviation bound. The histories start after the initial condition transient has decayed, to allow the later detail to be seen. The semimajor axis error was computed relative to the CDC truth ephemeris. The error history from the EKF is included (as Figure 5-7) to provide a baseline against which the impact of varying the ESKF integration grid length can be seen.

The integration grid lengths used by each ESKF test were presented in Table 5-8. Using this data together with a detailed study of the EKF history and the histories of the ESKF tests yields three important observations:

1. Each ESKF history shows transients at the end of each integration grid; the transient at the end of the first integration grid was always the largest, due to the large error in the initial orbital elements (58 kilometers).

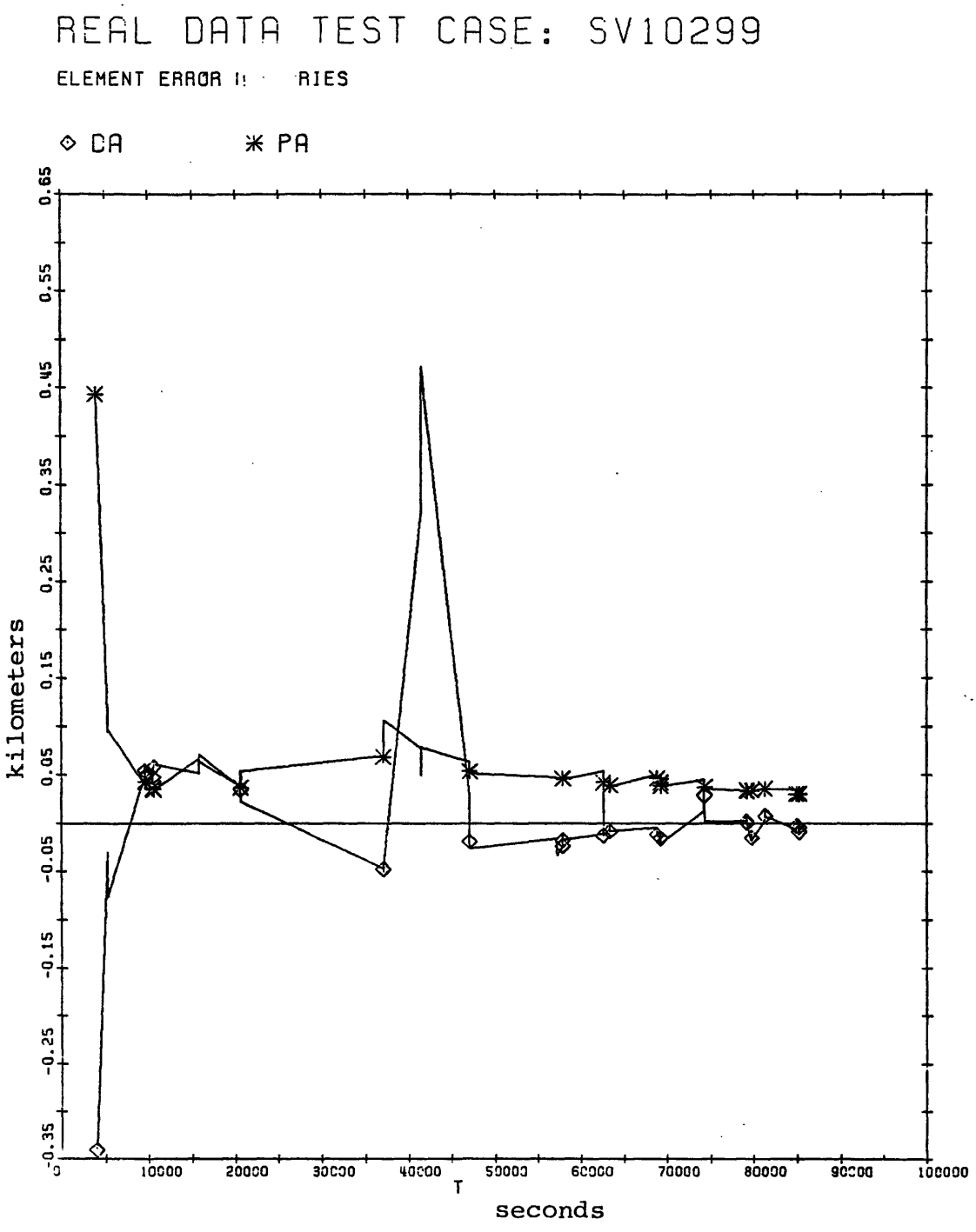

Figure 5-3. ESKF Semimajor Axis Error History, Run A (grid length = 43200 seconds)

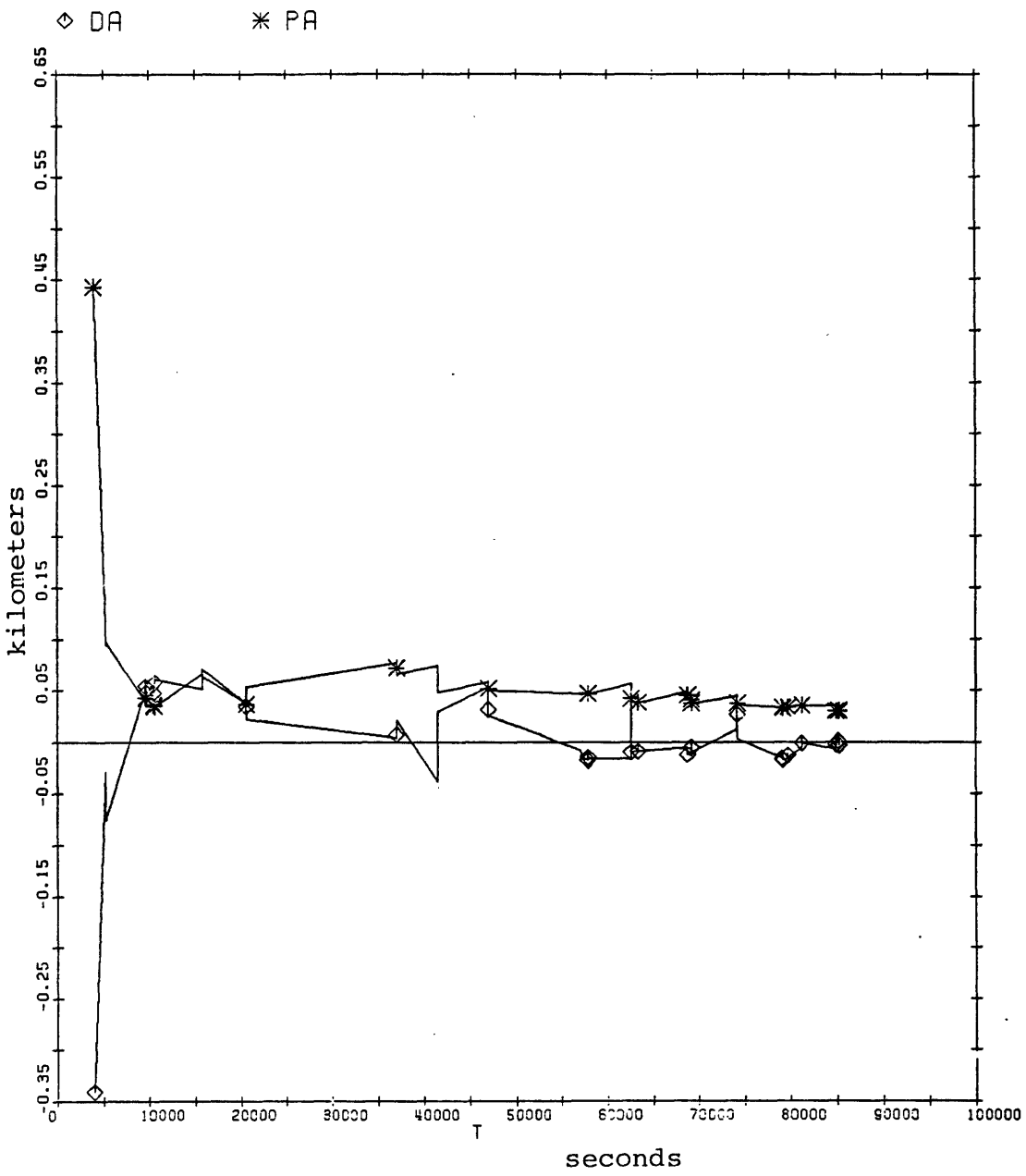

Figure 5-4. ESKF Semimajor Axis Error History, Run B (grid length = 29000 seconds)

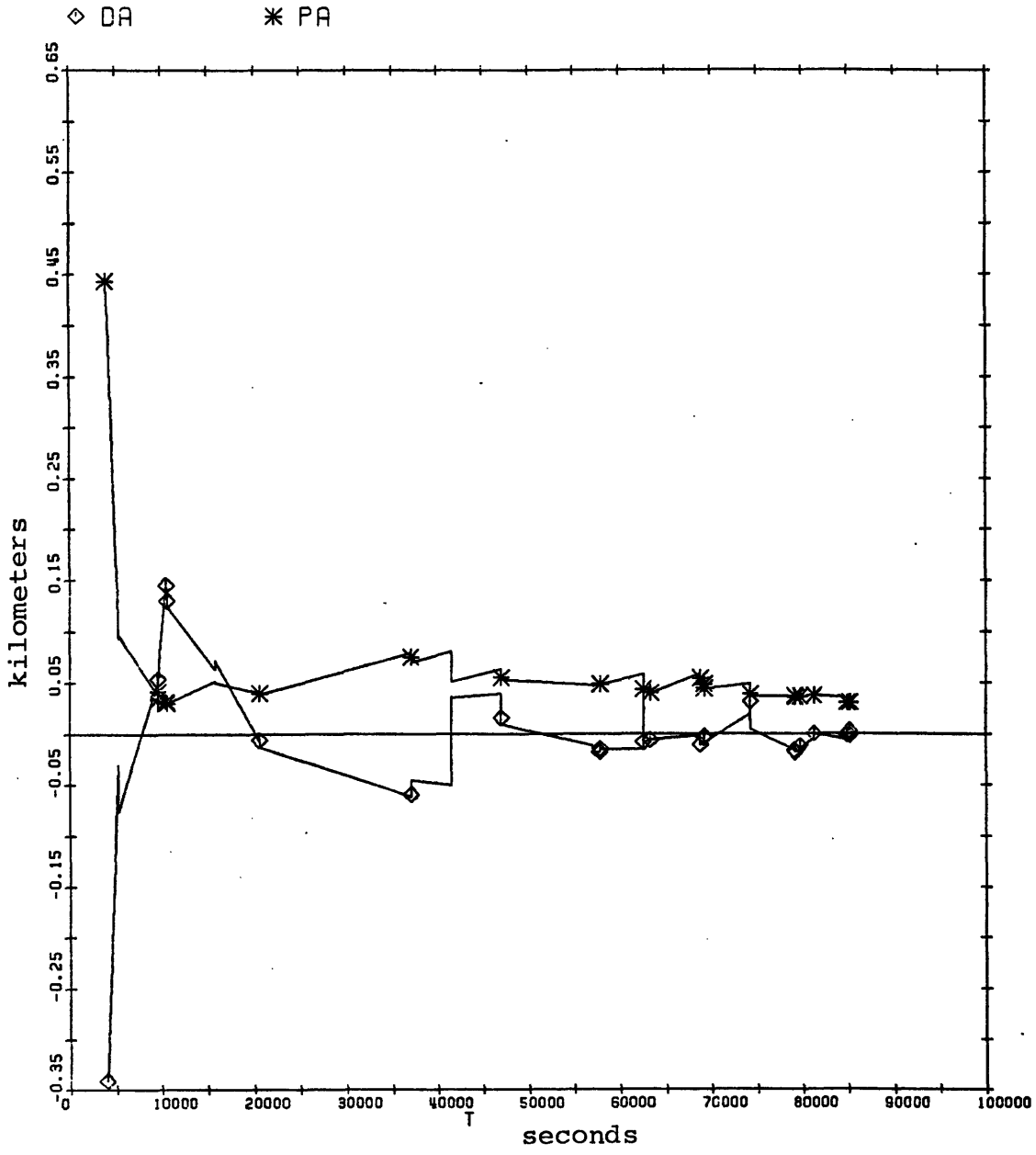

Figure 5-5. ESKF Semimajor Axis Error History, Run C (grid length = 9600 seconds)

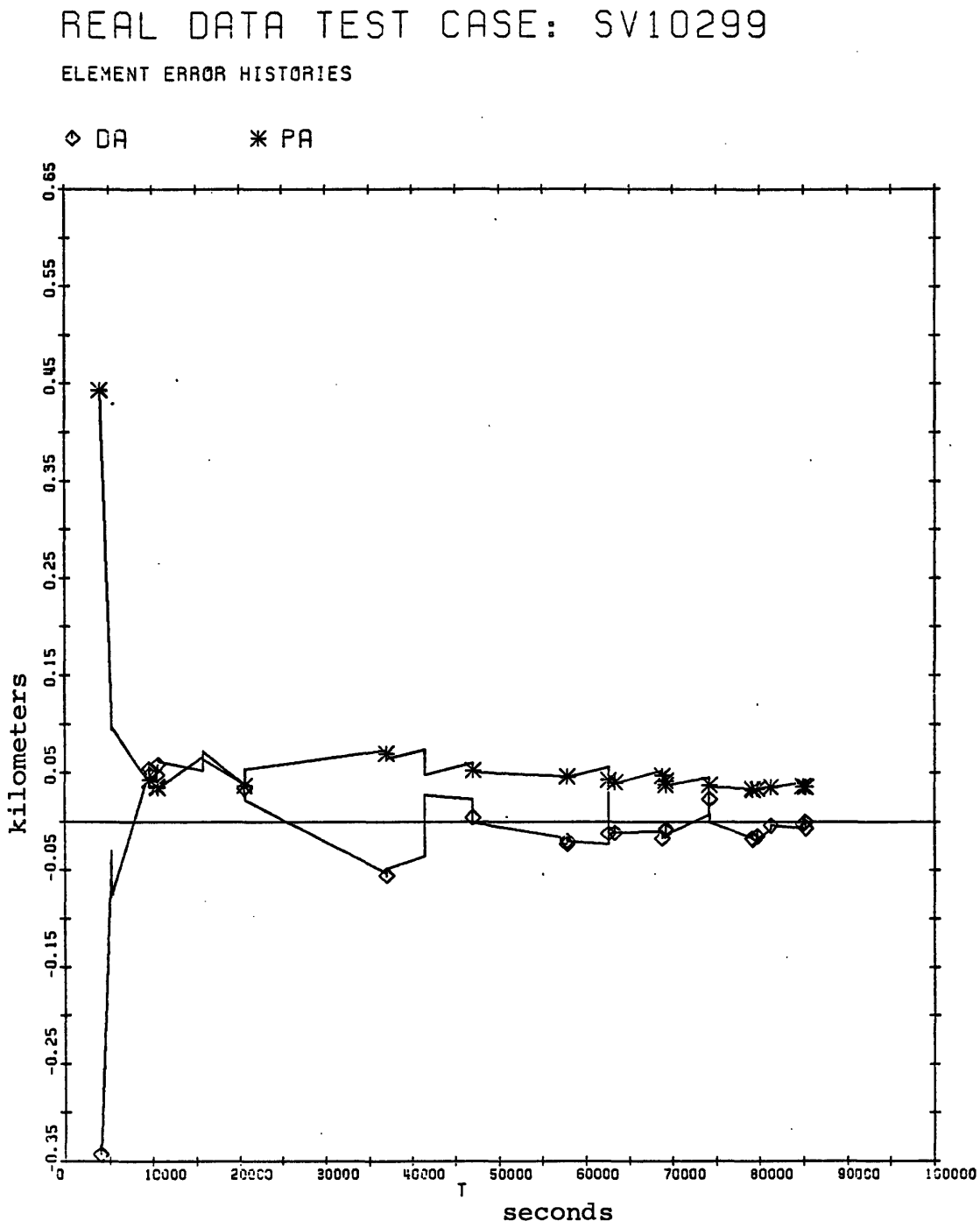

Figure 5-6. ESKF Semimajor Axis Error History, Run D (grid length = 21000 seconds)

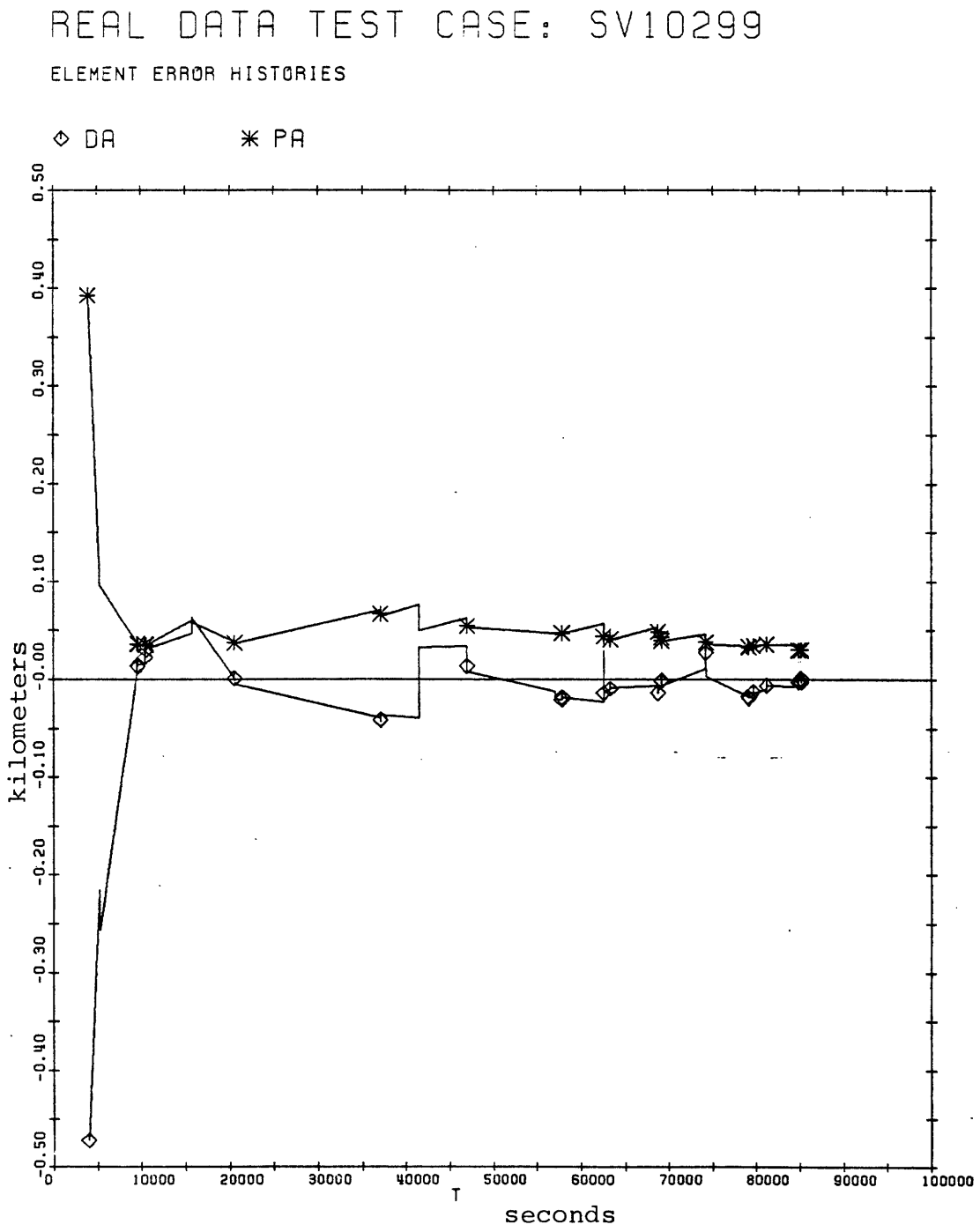

Figure 5-7. EKF Semimajor Axis Error History (integration stepsize = 10 seconds)

2. The ESKF tests B and D used intermediate integration grid lengths and show the smallest transients. The other ESKF tests used much smaller or much larger integration grid lengths and show much larger initial condition transients. Notice that the integration grid for run A ended in the middle of a long data outage (see Table 5-3); this may partially account for the large size of the transient for that test.

3. All of the filter histories agree quite closely from 60,000 seconds on. This implies that the tested integration grid lengths do not cause any appreciable accuracy differences once steady state filter operation has been achieved: the linearization errors for a steady state nominal trajectory are small.

The error histories for the other orbital elements show a very similar behavior, verifying these statements.

5.2.4 EKF and ESKF Steady State Performance

This section describes the steady state performance of the EKF and ESKF. Performance is measured by comparing the EKF and ESKF position estimates with those of the CDC truth ephemeris. Recall that the filter tests use the same force model as the CDC truth ephemeris. Thus the performance that is being measured is the ability of the filters to reproduce the batch DC estimate, in the presence of real-world observation and force model errors.

Figure 5-8 and Figure 5-9 show the position error histories for the EKF test and the ESKF test D. The variable DR is the actual error, while the variable PR represents a three standard deviation bound. Note that the histories start after the initial condition transient has decayed. There are four important observations to make:

1. The two filter histories are essentially identical, confirming all of the ESKF design assumptions for this test.

2. Both of the filter tests achieve a final position error of less than 50 meters with respect to the CDC truth ephemeris; the prediction error results presented in Table 5-8 verify this accuracy of the final filter estimates.

3. The transients in the position error and in the error bound result from the observation history, presented in Table 5-3. Each increase in the error or its bound reflects a data outage; decreases reflect the processing of new observations.

4. The actual position error is greater than the three standard deviation bound, indicating either slow filter convergence or apparent divergence.

The position error history for only one of the ESKF tests, test D, was presented here. The other ESKF tests show larger initial condition-related integration grid transients that are not pertinent to this discussion; note,

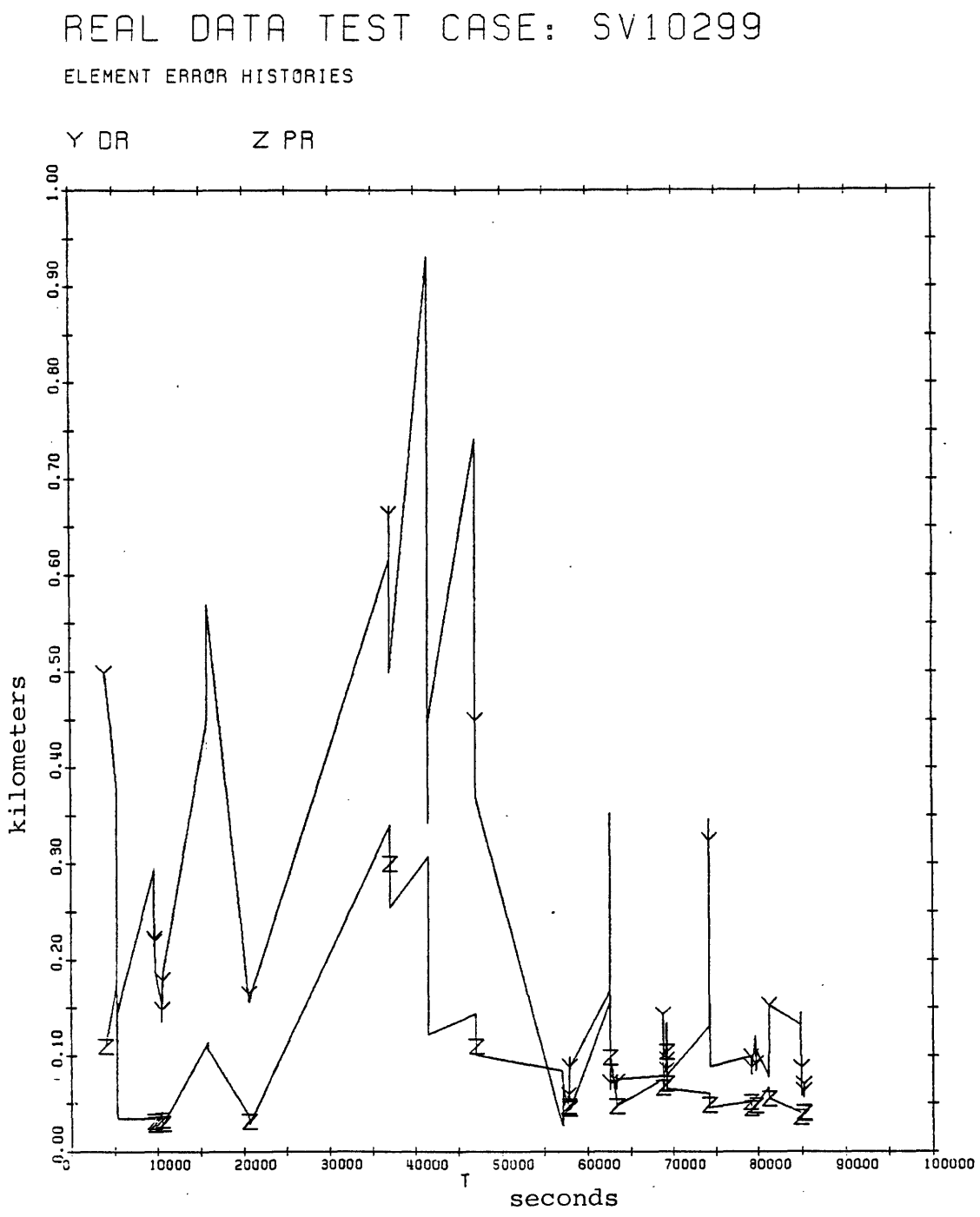

Figure 5-8. EKF Position Error History

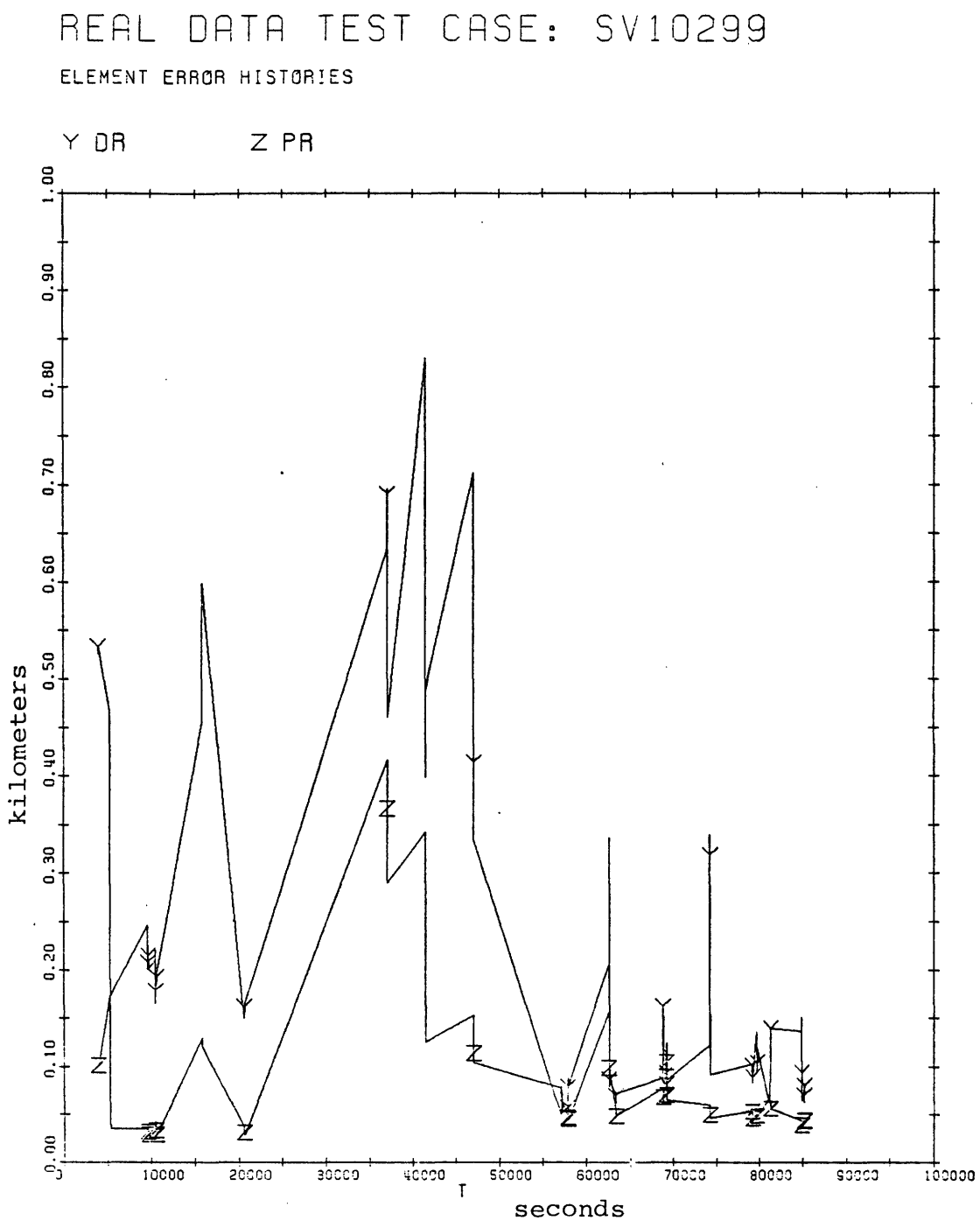

Figure 5-9. ESKF Position Error History, Run D

however, that the steady state performance of all the filter tests were essentially identical, both in the actual plot trace and in the final estimate accuracy.

The next section discusses the question of the filter process noise modelling, which is related to the question of apparent filter divergence, mentioned in (4) above.

5.2.5 Process Noise Model Verification

This section discusses the performance of the process noise model used in this real data test case. The process noise model is of interest for two reasons:

1. The correctness of the process noise model determines the accuracy of the filter estimation results; and

2. The value of the process noise strength was computed using the method derived in Appendix A. The results from this test case reflect the validity of that method.

The EKF and ESKF position error histories presented in the previous section show an apparent filter divergence: the position errors consistently exceed the three standard deviation bound. Note that the position errors remain bounded, implying that the process noise model is adequate. A more detailed investigation can be made using the element histories.

Figures 5-10 and 5-11 present the osculating Keplerian and mean equinoctial element histories for the EKF test and the ESKF test D, respectively. Variables prefixed by a 'D' refer to the actual error, while those prefixed by a 'P' refer to the corresponding three standard deviation bound. Two of the Keplerian variable names require explanation. The name 'CO' means capital omega, which is Ω, the longitude of the ascending node; the name 'LO' means lower case omega, which is ω, the argument of perigee. All of the other variable names follow directly from the usual notation.

Figure 5-10 includes the osculating Keplerian histories for the inclination, the longitude of the node, and the argument of perigee; each of these element histories shows an apparent divergence for a significant portion of the observation span. The mean equinoctial element Q is the only mean element showing an apparent divergence. The apparent divergence of Q is fundamental, since the process noise calculations for both the EKF and the ESKF are based on the process noise strength computed in mean equinoctial coordinates using the method given in Appendix A.

Three possible explanations for the mismodelling of the process noise for Q are proposed:

1. The observations offer poor observability of Q, so that either a longer data arc or multiple passes through the data are required;

2. The filters are tracking the real satellite dynamics, as indicated by the observations, rather than the truncated and aproximate force model employed by the CDC truth ephemeris; and

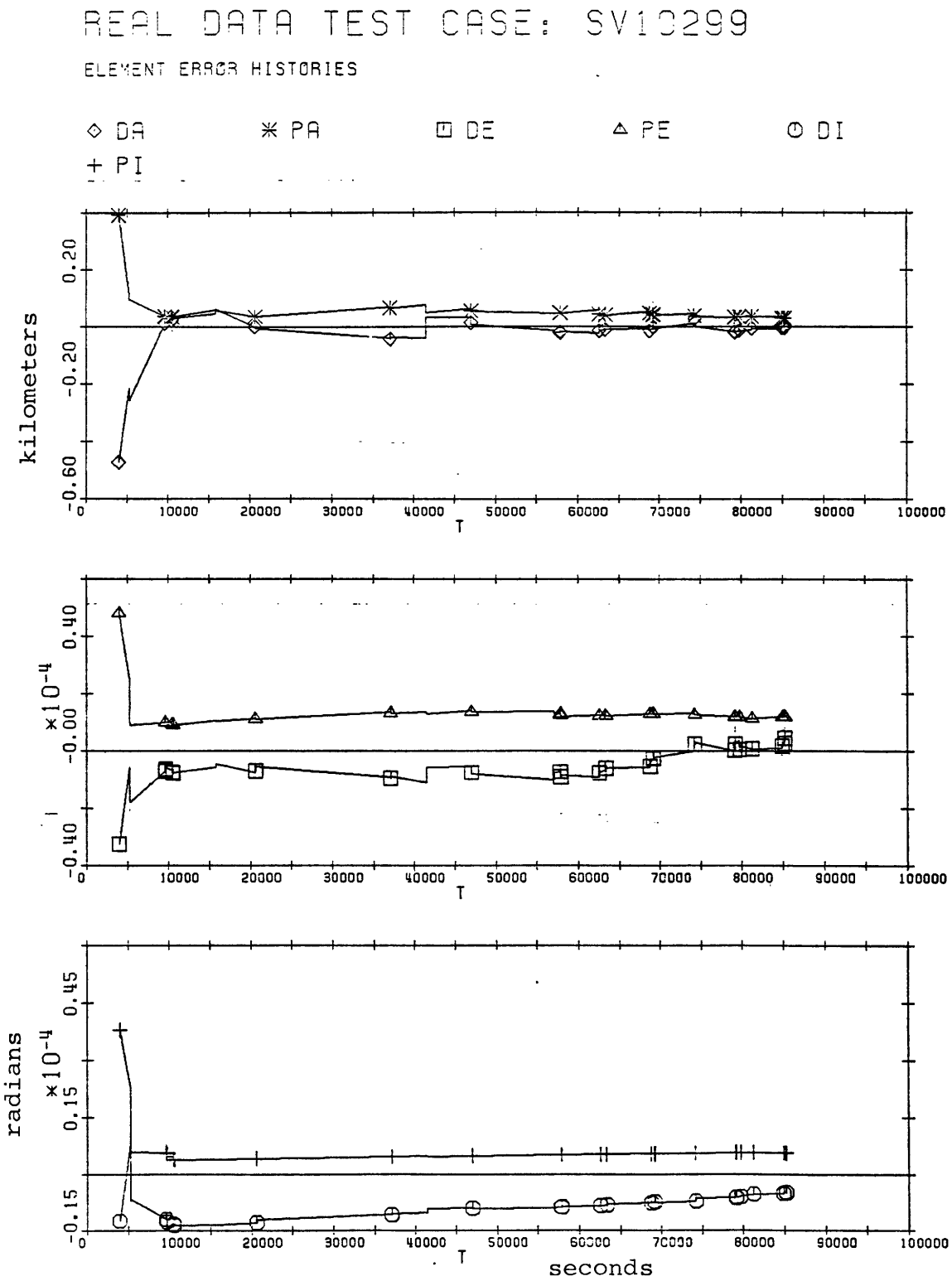

Figure 5-10. EKF Osculating Keplerian Element Histories

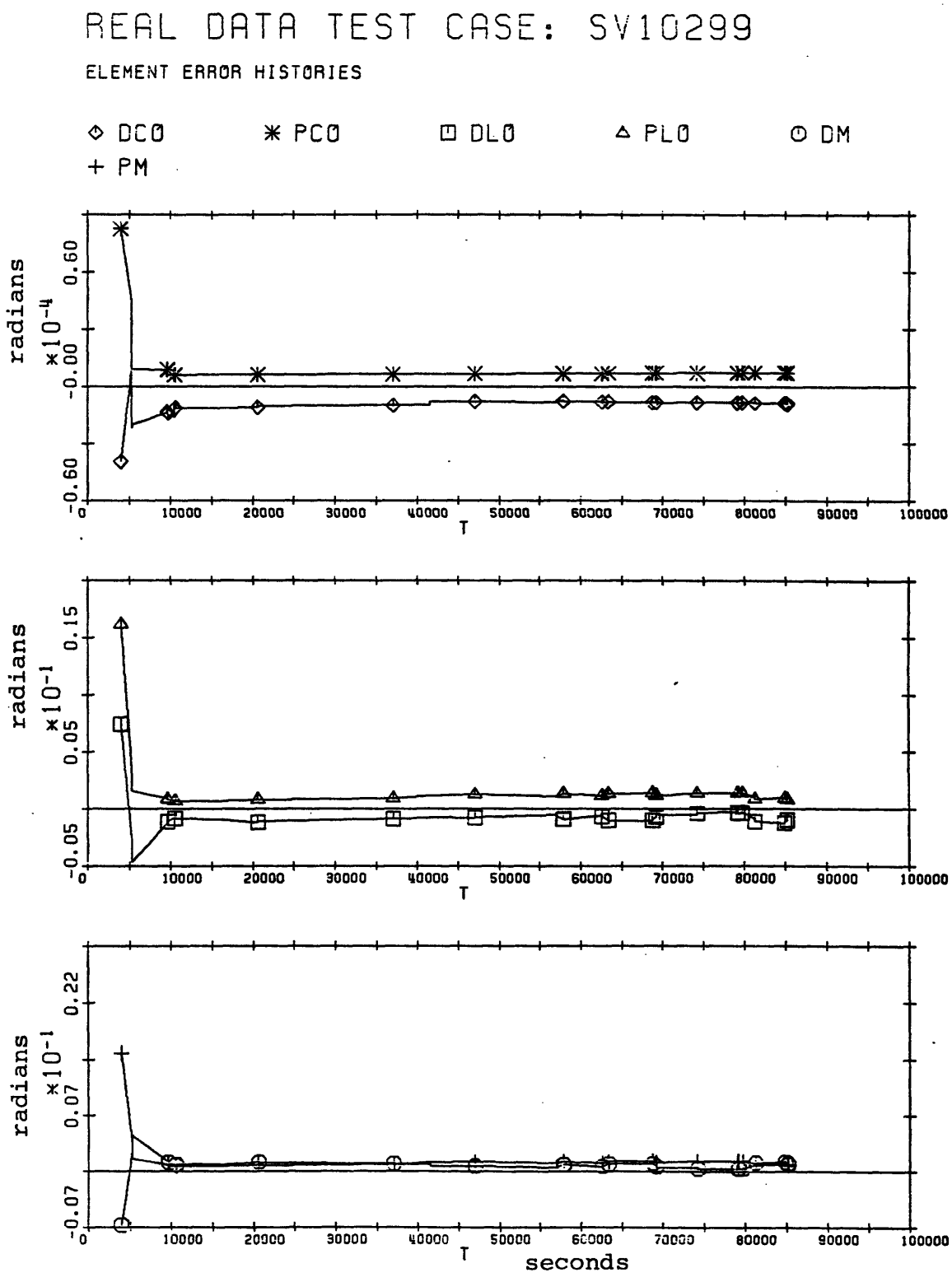

Figure 5-10. continued

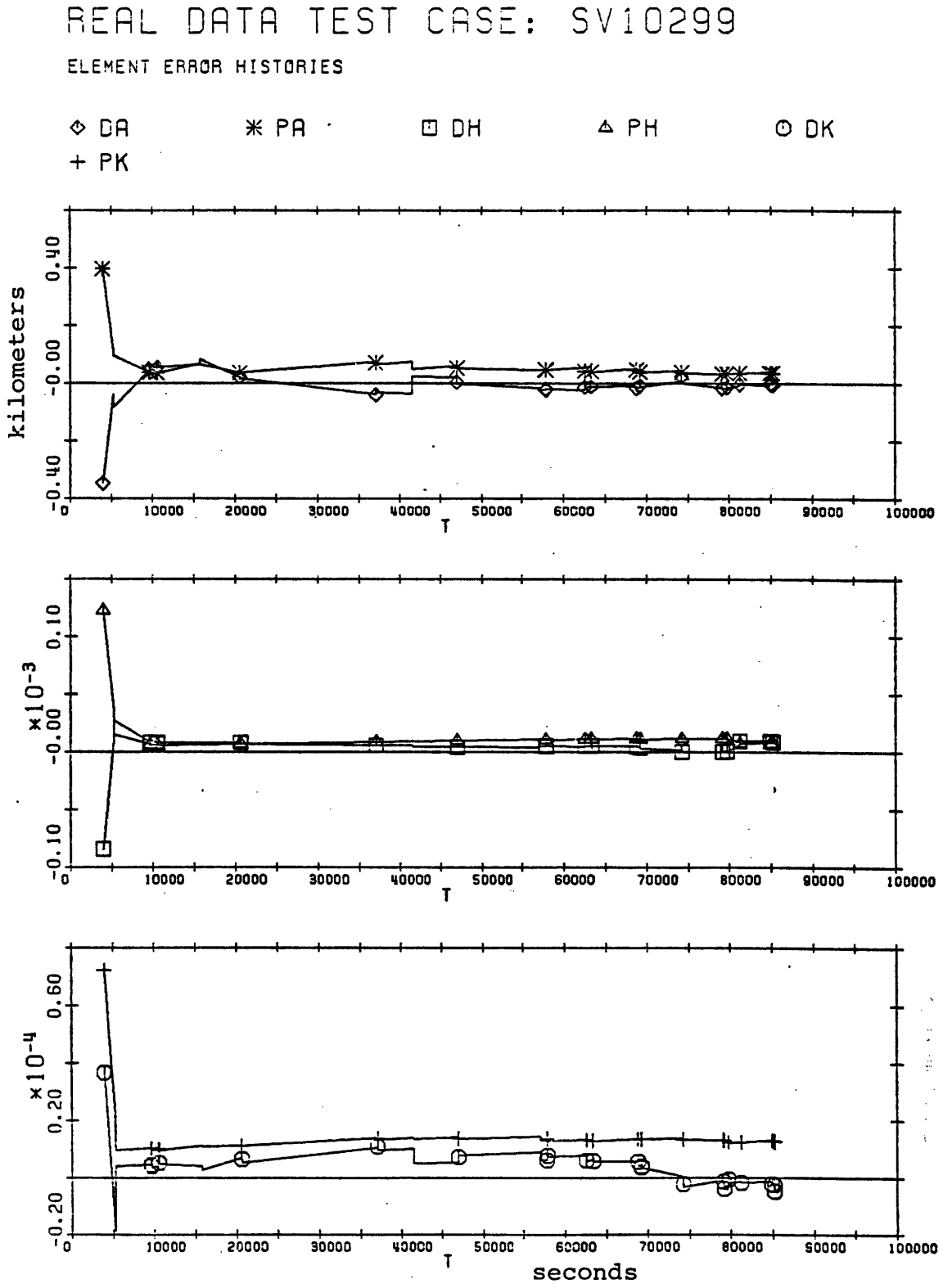

Figure 5-11. ESKF Mean Equinoctial Element Error Histories, Test D

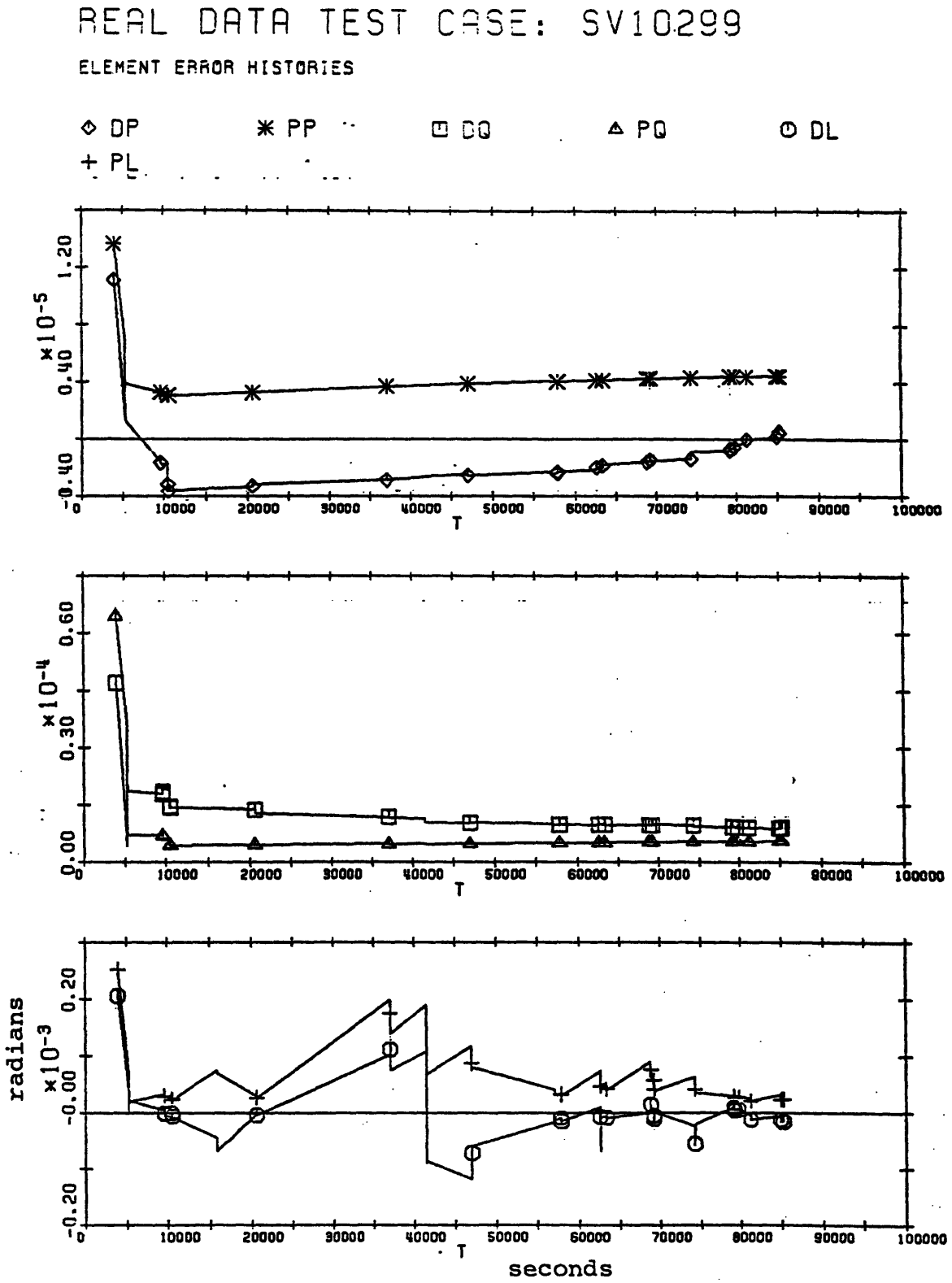

Figure 5-11. continued

3. There is an error in either the method or the statistics used in the process noise strength calculations of Appendix A.

The second proposed explanation can be made more specific. The discussion of the CDC and SDC truth ephemerides indicated that the satellite was in very sharp resonance with the sixteenth order geopotential harmonics. The effects of this resonance were not considered in the process noise calculations of Appendix A. Now a filter tends to follow the observtions more closely than does a differential corrections algorithm, so it is possible that a bias was introduced by the neglect of resonance in the force model. Certainly the error history of Q indicates that only a small bias is required. It is interesting to note that resonance generally causes motions of the orbital plane, and hence has a significant impact on the equinoctial elements P and Q.

In conclusion, Figures 5-10 and 5-11 show that the process noise model developed in Appendix A was basically successful. Additional work must be done in order to completely explain the apparent divergence of the estimate of the equinoctial element Q.

5.2.6 Semianalytical Modelling Errors

This section presents evidence indicting a very small semianalytical force model error when compared with the real world dynamics.

Figures 5-12 and 5-13 present the inclination errors from the CDC truth ephemeris for one day predictions of the final estimates of the EKF test and the ESKF test D, respectively. Notice that the EKF prediction error is quite smooth, while the ESKF prediction error shows an error residual with a twelve hour period.

Proulx, et al. [18] investigated similar 12 hour periodic errors, and successfully modelled a large portion of such errors as resulting from the coupling between the average element rates due to oblateness and the m-daily short periodics. Proulx's model was employed in all of the ESKF and SDC tests conducted for this test case; the 12 hour periodic error shown in Figure 5-13 is the residual error. While additional work is required to account for this residual error, its small magnitude does not make such work an urgent requirement.

5.3 Real Data Test Case Summary

The results of this chapter extend the conclusions of Chapter 4 in several important ways:

1. The EKF and ESKF were used to process real observational data, with the resulting accuracy consistent with that of the batch CDC and SDC estimators;

2. The primary impact of the choice of the integration grid length was found to be due to the linearization errors induced by the large initial condition errors used in this test case;

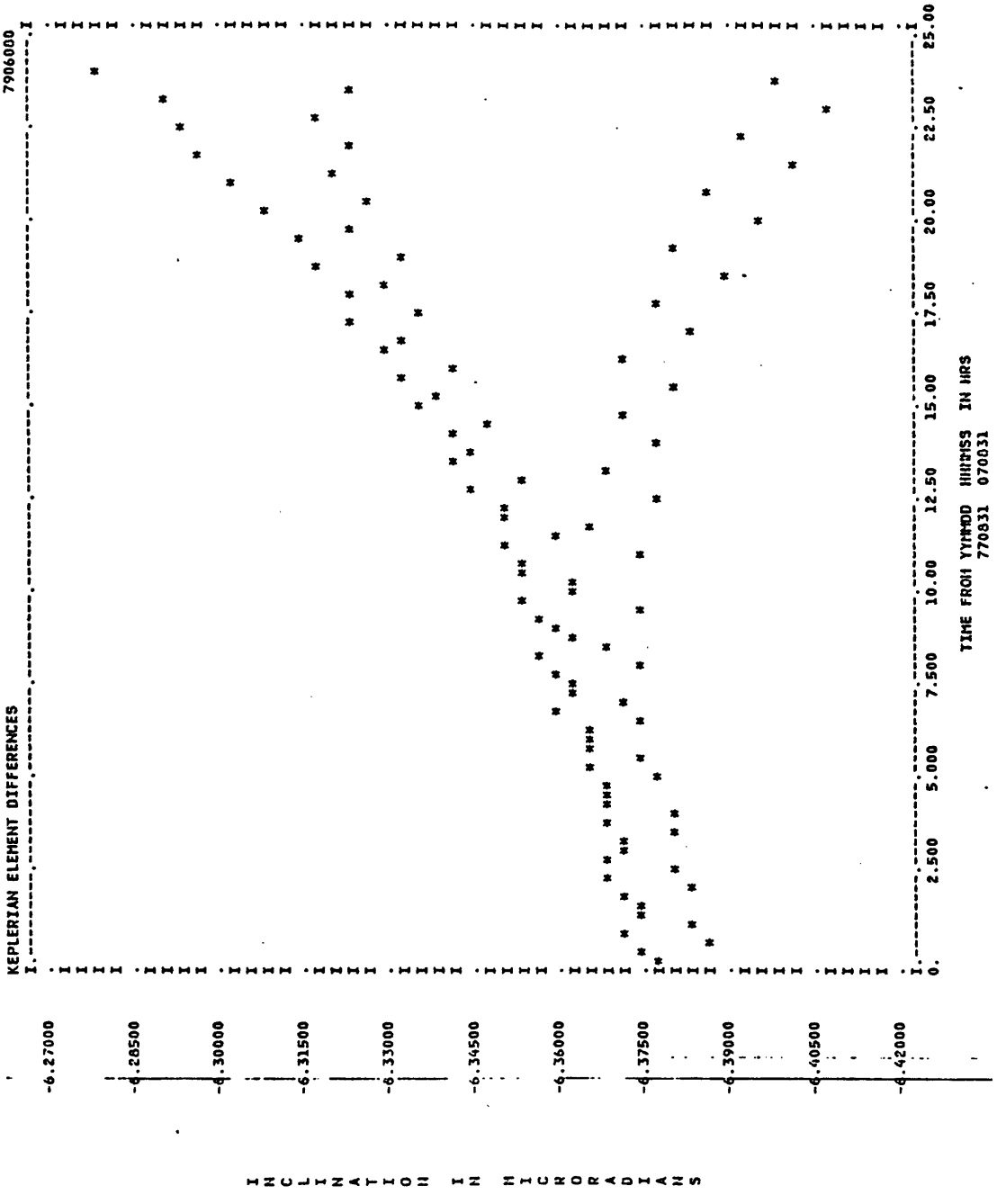

Figure 5-12. EKF Predicted Inclination Error

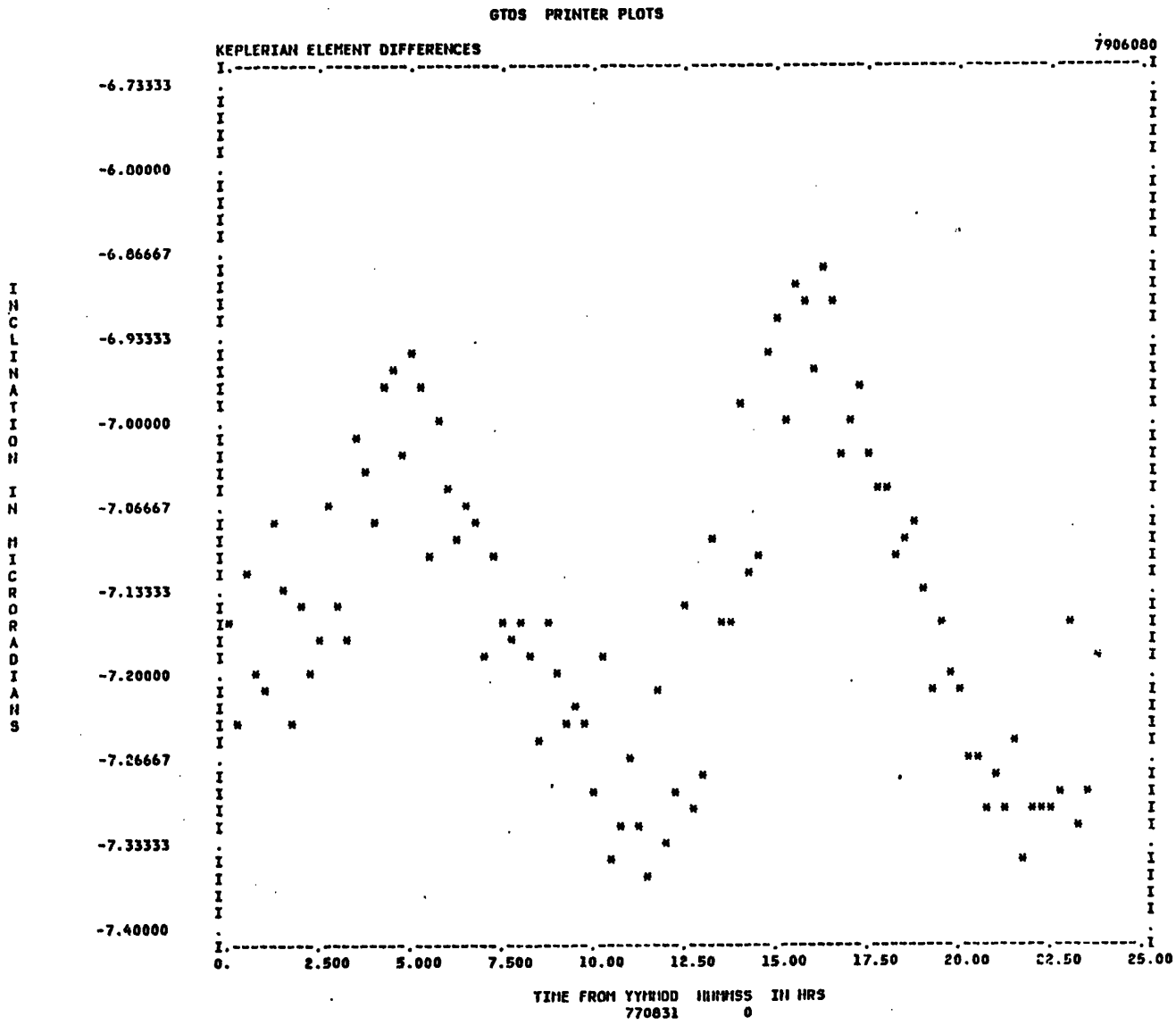

Figure 5-13. ESKF Predicted Inclination Error, Run D

3. The EKF and ESKF were found to have very similar filter histories and accuracy when corresponding input parameters were used, especially in the region of steady state performance;

4. The ESKF was found to have a considerable efficiency advantage over the EKF, even though the computer software employed for the ESKF tests has not been optimized;

5. The process noise model developed in Appendix A was basically verified, although additional work must be done to improve the modelling for one element.

In addition to these results, an interesting force model anomaly concerning the GEM 9 sixteenth order gravitational coefficients was discovered; a good deal of additional work must be done to identify and prove the mechanism for the anomaly.

Chapter 6
CONCLUSIONS AND FUTURE WORK

The primary goal of this thesis has been the design of improved sequential orbit determination algorithms by application of the computational methods of semianalytical satellite theory to the estimation algorithms resulting from sequential filtering theory.

Two new orbit determination algorithms are presented in this thesis. They are called the Semianalytical Kalman Filter (SKF) and the Extended Semianalytical Kalman Filter (ESKF). Both of these algorithms were designed with the objective of achieving the same accuracy as existing sequential orbit determination algorithms while retaining the advantage in computational efficiency enjoyed by semianalytical satellite theory.

The SKF and ESKF designs are based on suboptimal filters: the Linearized Kalman Filter (LKF) and the Extended Kalman Filter (EKF), respectively. These suboptimal filters are typically used in sequential orbit determination algorithms and have been found to perform quite adequately. The use of these filters is important for the SKF and ESKF designs, since they allow a good deal of decoupling between the computational structures of the satellite theory and the filter. Chapter 2 presents the mathematical introductions to semianalytical satellite theory and to sequential estimation theory required for the design of the SKF and the ESKF.

Chapter 3 discusses the actual designs of the SKF and the ESKF. The SKF served as the baseline for the design of the ESKF. The computational flow of each algorithm is explicitly detailed to indicate the interaction between the filters and the satellite theory. The SKF and ESKF assume that the solve vector consists of the mean equinoctial elements generated by the semianalytical orbit generator and any unknown dynamic parameters, such as the coefficients of drag or solar radiation pressure. This solve vector is the most natural one for the given satellite theory, and accounts for all of the possible interactions between the satellite theory and the filter solve vector. Chapter 3 also presents the results of three numerical tests conducted to verify simplifying design assumptions for the SKF and the ESKF. These design assumptions allow: (1) neglect of the state transition matrix in process noise calculations, (2) the use of the LKF state correction prediction equations for the ESKF, and (3) the use of the B_1 matrix for short periodic corrections instead of recomputed short periodic coefficients in the calculation of the ESKF predicted osculating elements. Each of these assumptions has a large impact on the overall efficiency of the SKF and ESKF; the latter two represent the interaction of the perturbation theory formulation of semianalytical satellite theory with the filtering techniques employed.

The results from two end-to-end orbit determination test cases are presented in Chapters 4 and 5.

The test case of Chapter 4 used a short arc of simulated data for a low altitude polar satellite to examine the performance characteristics of the SKF, ESKF, LKF, and EKF

during their transient response to a large initial condition error. No errors were introduced in the filter dynamical models, but errors were added to the observations. A realistic initial condition error was generated by using the GTDS early orbit algorithms. The performance of each filter was tested subject to several of the applicable input parameters. These parameters included:

1. the a priori covariance,
2. the process noise model,
3. the filter force model,
4. relinearization strategy for the nominal trajectory,
5. coefficient of drag estimation,
6. B_1 matrix short periodic linearization or truncation,
7. the semianalytical interpolator structure, and
8. mean early orbit initialization for the SKF and ESKF.

The performance of each test was measured in three ways: by the accuracy of ephemeris predictions based on the final filter estimate; by the position error history during the observation processing span; and by the efficiency estimate given by the CPU time required for execution.

The test case of Chapter 5 extended the results of the short-arc test case of Chapter 4 in two ways: the filters processed a sufficient amount of data to achieve a steady state, and real satellite tracking data was processed, so real-world errors occurred in the observations and in the force model. Only the EKF and ESKF were used to process

this data. The EKF and ESKF tests used corresponding (transformed) initial conditions and process noise models. The process noise model used in these tests is developed in Appendix A. This model is approximate but allows consideration of the effects of probable real world force model errors. Several ESKF tests were conducted to determine the impact of semianalytical force model truncations and the integration stepsize on ESKF performance. The same performance measures used in Chapter 4 were used here: prediction accuracy, the observation span error history, and the CPU execution time. The prediction accuracy and the observation span error history were measured relative to the baseline provided by a batch differential corrections (DC) orbit determination algorithm.

The real data test case formulation uncovered an interesting force model anomaly: the interaction of the GEM 9 16th order gravitational coefficients with the Harris-Priester Amtospheric Density Model and drag coefficient estimation caused a degradation in the prediction performance of the DC algorithms. The given satellite was in a very sharp resonance with the 16th order geopotential harmonics. The results of several DC tests defining this anomaly are presented in Section 5.1. More work is required to completely explain this anomaly.

6.1 Conclusions

The fundamental conclusion to be drawn from the work presented in this thesis is that substantial improvements in efficiency can be made without loss of accuracy by the application of semianalytical satellite theory to the

sequential orbit determination problem. This conclusion is supported by the results of the short-arc test case of Chapter 4, used to examine filter transient response, and by the results from the many-orbit test case of Chapter 5, used to examine steady state filter performance in the presence of real-world model errors.

Several other significant conclusions can be stated:

1. The computational structures of the LKF and the EKF are compatible with the interpolator structures of semianalytical satellite theory; the one possible exception occurs when the ESKF is used with the position and velocity interpolator [see Equation (3-10) and Section 4.3.2].

2. The assumptions employed in the design of the SKF and the ESKF have been verified, both by direct numerical tests, and by the final filter performance.

3. Semianalytical Satellite Theory offers considerable flexibility for truncations in the analytical development of the force model, with the potential for large improvements in the efficiency without loss of accuracy.

4. The length selected for the integration grid can have a significant effect on SKF and ESKF accuracy during transients; there were not any detectable accuracy differences during steady state filtering for the cases considered.

5. The linearized corrections to the short periodic functions obtained by use of the B_1 matrix are important for the accuracy of the ESKF predicted osculating elements.

6. The process noise model employed by any of the filters tested can have a significant impact on the resulting estimation accuracy. The process noise model developed in Appendix A was generally successful in accounting for the dynamical model errors in the real data test case.

7. Drag coefficient estimation can be very important for the accuracy of the ephemeris predictions of low altitude satellites.

8. The Epoch Point Conversion Iteration (4-1) gives a low-cost means of obtaining good mean equinoctial elements.

9. The process noise and a priori covariance can be successfully transformed from mean equinoctial coordinates to osculating position and velocity coordinates when corresponding ESKF and EKF tests are desired.

10. The EKF and ESKF are able to successfully estimate and predict satellite orbits in the presence of real-world observation and force model errors.

11. The EKF and the ESKF offer significant improvements in performance over simple global linearization algorithms like the LKF or the SKF. There

are specific applications, however, where the simpler computational structures of the LKF and SKF will make their use uniquely desirable [6].

Each of these conclusions is supported by the results from the test cases considered. None of the conclusions is totally unexpected. It is desirable that additional support be provided by further testing. This and other issues for future work are addressed in the next section.

6.2 Future Work

The research presented in this thesis motivates additional work in filtering theory, in semianalytical satellite theory, and in the requirements for the operational implementation of the orbit determination algorithms studied in this thesis. Recommendations are also presented for areas requiring further testing, both to verify the conclusions of this thesis and to establish the performance characteristics for different orbit determination problems.

One of the important results of Chapter 4 was the discovery of the sensitivity of filter performance to the process noise model employed. This discovery motivated the development of the process noise model of Appendix A, which allowed the a priori calculation of a process noise strength. Alternative approaches to the process noise modelling problem are given by the work of Wright [35] and the covariance correction term of the Gaussian Second Order Filter, which model gravity model errors and filter linearization errors, respectively. The application of these alternate approaches to the semianalytical filters discussed

herein deserves further study. In particular, it may be possible to use the slowly varying nature of semianalytical dynamics to develop very efficient implementations of these methods. The Dynamic Model Compensation (DMC) method [34] may offer additional benefits.

Two extensions of Semianalytical Satellite Theory will help support additional testing of the SKF and the ESKF. The test cases in this thesis studied low altitude nearly-circular satellite orbits. The development of explicit third body short periodics will allow mean element initialization for high altitude satellites at low cost, by use of an EPC procedure. The development of analytical B_1 matrix models for the third body perturbation and for the oblateness perturbation (closed-form in the eccentricity) will allow the ESKF to be tested efficiently with high altitude and high eccentricity satellites, respectively.

Several aspects of the operational implementation of the SKF and ESKF require investigation. Very little has been done to establish the tradeoffs between accuracy and efficiency when various truncations of the analytical development of the semianalytical force model are made. The tests presented in this thesis indicate that large increases in efficiency with only small losses of accuracy are possible. The question of software optimization should also be addressed. The current implementation did not have efficiency as a primary goal, and so a good deal of optimization is possible. A timing budget of the program flow would be helpful here. Finally, one of the important applications for the SKF and ESKF may lie in the area of autonomous satellite navigation. The standard Kalman prediction

and update algorithms currently implemented should be rather easily replaced by a more stable square root formulation. The requirements for implementing semianalytical satellite theory in a small word length computer should be studied.

The last area for future work consists of recommendations for additional orbit determination test cases to be examined. There are many extensions to the test cases studied in this thesis. For example, performance evaluations for high altitude and high eccentricity satellites are of interest. The question of steady state accuracy when very high accuracy observations are available is important. Equally important is the estimation accuracy when there is only a very sparse schedule of observations. Further tests are required to establish the exact performance properties of the ESKF when the position and velocity interpolator is used (see Section 4.3.2). The last test case proposed for future study examines the effects on filter accuracy and stability of deterministic force model errors, such as satellite maneuvers, or rapid atmospheric density changes. The use of real observational data offers one means of making these tests. In this regard, a further investigation of the force model anomaly can be made by using the tracking data from the MAGSAT satellite. This satellite should also have been in a very sharp 16th order geopotential resonance during several days of its decay.

Appendix A
PROCESS NOISE MODEL SELECTION

The results from Chapter 4 show that filter estimation accuracy can be very sensitive to the process noise model used. A trial and error search for the process noise strength giving the best estimation accuracy could be conducted for the simulated data test of Chapter 4, since a truth model existed for measuring that accuracy. The real data test case of Chapter 5 and efficiency requirements in general motivate the development of more rigorous methods for process noise modelling. This appendix discusses the selection of the process noise strength for the real data test case and indicates extensions for other situations. The transformation of the process noise covariance from equinoctial coordinates to cartesian coordinates for making analogous EKF and ESKF runs is also presented.

A.1 Process Noise Analysis for Semianalytical Satellite Theory

Process noise models are used to account for the growth of the true estimation error due to dynamical modelling errors. The basic requirement for stable estimation with a filter is that the true errors correspond to the covariances computer by the filter; the squared errors should roughly equal the computed variances. When the covariances are too small, the Kalman gain is also too small, so the required corrections are not made. When the covariances are too large, the Kalman gain is correspondingly too large and over corrections are made that can result in unstable oscillation

of the estimate errors. These insights form the basis of the three approaches to process noise modelling found in the literature:

1. Use of the white noise model for the process noise, with the strength set either by trial and error or by physical considerations [3], [20], [29], [33];

2 Modelling the process noise as a first order Markov process, with the initial conditions and dynamics selected parametrically for optimum performance [34]; and

3. Analytical development of force model error correlations based on geodetic error analysis [35].

The first approach is used here, taking advantage of the near-linearity and slowly-varying character of the semi-analytical dynamics.

The development of the process noise model assumes the formal existence of the true dynamical model as well as the known nominal model. These are represented as

$$\dot{\bar{a}} = \varepsilon \underline{A}_1(\bar{a}) + \varepsilon^2 \underline{A}_2(\bar{a}) + \ldots ; \bar{a}(t_o) = \bar{a}_0 \qquad (A\text{-}1)$$

and

$$\dot{\bar{a}}_N = \varepsilon \underline{A}_N(\bar{a}_N) + \underline{u} \; ; \; \bar{a}_N(t_o) = \bar{a}_{N_0} \qquad \text{(A-2)}$$

respectively. Note that the true model contains the complete expansion of the averaged equations of motion, so that no analytical approximations are made at all. The nominal model is truncated at first order, consistent with the Semianalytical Satellite Theory developed in Chapter 2. Also, the first order term $\varepsilon \underline{A}_N$ is not exact, reflecting the errors in known force models. The term $\underline{u}$ is the process noise; it is to be selected to minimize the difference between $\overline{\underline{a}_N}$ and $\bar{a}$.

Let $\overline{\Delta \underline{a}} = \bar{a} - \bar{a}_N$ be the trajectory error between (A-1) and (A-2). Write $\varepsilon \underline{A}_1(\cdot) = \varepsilon \underline{A}_N(\cdot) + \delta \underline{A}_1(\cdot)$ to explicitly account for force model errors. A perturbation equation for $\overline{\Delta \underline{a}}$ results from subtracting (A-2) from (A-1)

$$\Delta \dot{\bar{a}} = \frac{\partial \varepsilon \underline{A}_N}{\partial \bar{a}_N} \Delta \bar{a} + \frac{1}{2} \Delta \bar{a}^T \frac{\partial^2 \varepsilon \underline{A}_N}{\partial \bar{a}_N^2} \Delta \bar{a} + \ldots$$

$$+ \delta \underline{A}_1(\bar{a}) + \varepsilon^2 \underline{A}_2(\bar{a}) + \ldots \qquad \text{(A-3)}$$

with initial condition $\overline{\Delta \underline{a}}_o = \bar{a}_o - \bar{a}_{N_o}$. This equation accounts for all three sources of dynamical model error in the perturbation equation employed by semianalytical filters; the second, third, and fourth terms on the right hand side of (A-3) are due to:

1. neglect of higher order terms in the linearization of the equations of motion required by filtering theory;

2. first order force model errors; and

3. truncation of the asymptotic series expansion of the averaged equations of motion (see McClain [9] for the general development of this series).

These error sources are modelled using process noise as

$$\Delta\dot{\bar{\underline{a}}}_N = \frac{\partial \varepsilon \underline{A}_N}{\partial \bar{\underline{a}}_N} \Delta\bar{\underline{a}}_N + \underline{\nu} \; ; \; \Delta\bar{\underline{a}}_{N_0} = 0 \qquad \text{(A-4)}$$

The new process noise $\underline{\nu}$ is to be selected for the best matching of $\Delta\underline{a}$ and $\Delta\underline{a}_N$. This matching is done statistically, by equating covariances, in recognition of lack of knowledge of $\underline{\nu}$.

Equation (A-4) is a linear equation and so has a state transition matrix solution $\phi(t,t_o)$. The solution to (A-4) is

$$\Delta\bar{\underline{a}}_N(t) = \int_{t_o}^{t} \phi(t,\tau)\, \underline{\nu}(\tau)\, d\tau \qquad \text{(A-5)}$$

Now semianalytical (and other VOP) dynamics are almost linear, so the approximation $\phi(t,t_o) \simeq I$ is quite good, as discussed in Section 3.4. The trajectory error becomes

$$\Delta\bar{\underline{a}}_N(t) = \int_{t_o}^{t} \underline{\nu}(\tau)\, d\tau \qquad (A\text{-}6)$$

Using the white noise model for the process noise and assuming it has constant strength gives the result verified in Section 3.4.1

$$\Lambda(t,t_o) = Q \cdot (t - t_o) \qquad (A\text{-}7)$$

On the other hand, another expression for Λ can be derived using semianalytical heuristics. Since $\underline{\nu}$ is a vector of unmodelled mean element rates, it is slowly varying. It can also be deterministically modelled, since it results from errors in deterministic models. The new expression for Λ assumes that $\underline{\nu}$ is not random; thus the mean square value of $\underline{\nu}$ is

$$\Lambda(t,t_o) = \int_{t_o}^{t}\int_{t_o}^{t} \underline{\nu}(\tau)\, \underline{\nu}^T(\sigma)\, d\tau\, d\sigma \qquad (A\text{-}8)$$

$$\simeq \underline{\nu}\, \underline{\nu}^T \cdot (t - t_o)^2$$

Equating this result with (A-7) gives

$$Q = \underline{\nu}\,\underline{\nu}^T\,\overline{\Delta t} \qquad \text{(A-9)}$$

This result is approximate, as indicated in two ways. First, no time argument is given for the mean element rate errors, $\underline{\nu}$. Rather, these rates will be computed based on knowledge of the truncation, force model, and initial condition errors; these error rates are assumed (and verified) to be sufficiently slowly varying. Second, some mean value for the prediction interval $t-t_o$ must be computed, to give the best fit between the time-linear model (A-7) and the quadratic model (A-8). The mean data outage time is a good value for $\overline{\Delta t}$, since filter divergence usually starts during an outage.

A.1.1 Real Data Test Case Process Noise

The process noise model presented above in Equations (A-1) through (A-9) was initially developed for the real data test case in Chapter 5. The process noise strength for that test case was selected to account for atmospheric density model errors and geopotential coefficient errors. The computations giving the process noise used for the real data test case are summarized here, step by step.

1. Δt was taken to be the mean data outage time. Outages on August 30, 1977 ranged from 30 seconds to 4.5 hours. The mean outage time was 1.125 hours or 4050.0 seconds.

2. A literature search was conducted to determine geopotential coefficient errors. Reference [36] gives the geopotential coefficients and estimated errors for the GEM 9 field used in GTDS. Typical coefficients and their errors are presented in Table A-1.

A mean value of σ_{rel} over all geopotential coefficients was desired, for computation of $\underline{\nu}$. This value was computed by means of a weighted average of the geopotential coefficient errors. The formula used was

$$\bar{\sigma}_{rel} = \sqrt{\frac{2 \sum_{n=0}^{N} \sum_{m=0}^{n} \delta_{nm}^2}{\sum_{n=0}^{N} \sum_{m=0}^{n} C_{nm}^2 + S_{nm}^2}} \qquad \text{(A-10)}$$

The numerator represents the resulting variances in the geopotential due to the random coefficient errors δ_{nm}. The denominator scales this standard deviation to make it relative to the whole geopotential perturbation. For an 8x8 field, $\sigma_{rel} = 2.4 * 10^{-4}$ resulted.

3. A literature search [37], [38], [39] into atmospheric density model errors resulted in an error standard deviation choice of $\sigma_{rel} = 20\%$.

Table A-1
Geopotential Coefficients and Errors

Taken from Gravity Model Improvement Using Geos-3 (GEM 9 & 10) GSFC, 1977

n,m	$C_{n,m}$ 1E-6	$S_{n,m}$ 1E-6	$\delta_{n,m}$ 1E-9	σ_{rel}
2,0	-484.2	---	1	2E-6
3,0	0.958	---	1	1E-3
4,0	0.542	---	1	2E-3
5,0	0.068	---	2	3E-2
6,0	-0.151	---	2	1E-2
7,0	0.093	---	2	2E-2
8,0	0.051	---	2	4E-2
15,0	0.001	---	5	5E-0
17,0	0.016	---	5	3E-1
2,2	2.434	-1.398	3	1E-3
3,1	2.028	0.252	5	2E-3
3,2	0.892	-0.622	8	7E-3
4,1	-0.533	-0.465	5	7E-3
4,2	0.353	0.663	5	7E-3
4,3	0.988	-0.203	4	4E-3

Notes: C_{nm}, S_{nm} = geopotential coefficient

δ_{nm} = coefficient error

$$\sigma_{rel} = \frac{\delta_{nm}}{\sqrt{C_{nm}^2 + S_{nm}^2}} = \text{relative error}$$

4. Mean element rate histories were generated over a 12 hour arc with the semianalytical integrator. Mean element rate contributions due to the geopotential and drag were printed separately. An 8x8 gravity field was used. The rates are given in Table A-2. The relative error standard deviations calculated in 2) and 3) are used to compute the probable errors in the mean element rates of Table A-2; these errors and the resulting total probable error are shown in Table A-3.

5. A diagonal process noise strength matrix Q was calculated, using

$$Q_{ii} = \nu_i^2 \, \bar{\Delta t} \qquad \text{(A-11)}$$

The resulting value of Q is

Q = diag[2.E-8,4.E-19,2.E-16,1.E-17,2.E-17,8E-16]

The elements h and k and the elements p and q have similar geometry. The matrix Q is normalized to give these corresponding elements the same noise strength. The value of Q used in the test case of Chapter 5 is

Q = diag[2.E-8,2.E-16,2.E-16,2.E-17,2.E-17,8E-16]

Table A-2

Mean Element Rates

Perturbation Type	a	h	k	p	q	λ
Analytical Central Body 1st Order	0.0	.949E-8	-.69E-9 to -.13E-8	.218E-6 to .225E-6	.308E-6 to .316E-6	-.167E-5
use approx	0.0	.1E-7	-.1E-8	.2E-6	.3E-6	-.2E-5
$J_2^2 e^0$, $J_2^2 e^1$ 2nd order	0.0	-.239E-11	-.75E-12 to -.93E-12	-.127E-9 to -.133E-9	-.131E-9 to -.135E-9	-.251E-8
use approx	0.0	-.2E-11	-.8E-12	-.1E-9		-.3E-8
Drag 1st Order Only (X2 π)	-.468E-4	±.33E-11 to ±(-).17E-9	.49E-8	-.49E-10	.64E-10	-.26E-10
use approx	-.7E-5	.1E-10	.1E-8	-.1E-10	.1E-10	-.5E-11

Table A-3
Mean Element Rate Probable Errors

$$\underline{\nu} = \varepsilon \underline{A} * \sigma_{rel}$$

	$\underline{\nu}$ Drag	$\underline{\nu}$ Grav
a	-2.E-6	0.0
h	-3.E-12	2.4E-12
k	2.E-10	-2.4E-13
p	-2.E-12	4.8E-11
q	2.E-12	7.2E-11
λ	-1.E-12	-4.8E-10

Total Rate Errors

$$\underline{\nu} = \begin{bmatrix} -2.E-6 \\ -1.E-12 \\ 2.E-10 \\ 5.E-11 \\ 7.E-11 \\ -5.E-10 \end{bmatrix}$$

A.1.2 Process Noise Modeling Extensions

The method used for the process noise computation for the real data test case of Chapter 5 can be used to model the process noise terms due to initial condition (i.e., linearization) errors and truncation errors. The basic requirement is the computation of the mean element rates $\underline{\nu}$ due to the error source. The state dynamics bias correction term from the Second Order Gaussian Filter can be used as an estimate for $\underline{\nu}$ due to initial condition errors. McClain's [9] equations for higher order terms in the averaged equations of motion must serve when modelling the process noise due to mean element rate truncation.

A.2 Process Noise Transformations

The desire to compare SKF and ESKF performance with the LKF and EKF implemented in the RD GTDS FILTER program raised the question of the validity of such comparisons. That is, the semianalytical filters have parameters and inputs given in mean equinoctial coordinates, while the Cowell filters have cartesian inputs and parameters. The transformation of the initial state and covariance are straightforward and are discussed in Chapter 4. The equations for transforming the process noise are developed here.

The process noise covariances in mean equinoctial and cartesian elements are

$$\Lambda_a(t,t_o) = \int_{t_o}^{t} \phi_a(t,\tau)\, Q_a(\tau)\, \phi_a^T(t,\tau)\, d\tau \qquad \text{(A-12)}$$

and

$$\Lambda_x(t,t_o) = \int_{t_o}^{t} \phi_x(t,\tau)\ Q_x(\tau)\ \phi_x^T(t,\tau)\ d\tau \qquad \text{(A-13)}$$

respectively, where

$$\phi_a(t,\tau) = \frac{\partial \underline{\bar{a}}(t)}{\partial \underline{\bar{a}}(\tau)} \qquad \text{(A-14)}$$

and

$$\phi_x(t,\tau) = \frac{\partial \underline{x}(t)}{\partial \underline{x}(\tau)} \qquad \text{(A-15)}$$

The process noise strengths Q are related in the same manner as the initial covariances. Thus

$$Q_x(\tau) = \left[\frac{\partial \underline{x}(\tau)}{\partial \underline{\bar{a}}(\tau)}\right] \cdot Q_a(\tau) \cdot \left[\frac{\partial \underline{x}(\tau)}{\partial \underline{\bar{a}}(\tau)}\right]^T \qquad \text{(A-16)}$$

The partial derivatives ϕ_x can be expanded by the chain rule in terms of ϕ_a by

$$\phi_x(t,\tau) = \left[\frac{\partial \underline{x}(t)}{\partial \underline{\bar{a}}(t)}\right] \cdot \phi_a(t,\tau) \cdot \left[\frac{\partial \underline{x}(\tau)}{\partial \underline{\bar{a}}(\tau)}\right]^{-1} \qquad \text{(A-17)}$$

Substitution of (A-17) and (A-16) into (A-13) gives the desired transformation

$$\Lambda_x(t,t_o) = \left[\frac{\partial \underline{x}(t)}{\partial \underline{\bar{a}}(t)}\right] \Lambda_a(t,t_o) \left[\frac{\partial \underline{x}(t)}{\partial \underline{\bar{a}}(t)}\right]^{T} \qquad \text{(A-18)}$$

There are two comments. First, the partials of position and velocity are time varying, so the process noise covariance calculated in (A-18) is not linear in time, contrary to GTDS assumptions. Second, the implementation of (A-18) requires the computation of the position and velocity partials; these partials can be expanded by the chain rule using the osculating equinoctial elements as intermediate variables as done in (2-34). Only the two body partials are used; the B_1 matrix of short peridic partials are neglected.

Appendix B
SOFTWARE OVERVIEW

The SKF and ESKF were implemented in the testbed provided by the version of RD GTDS resident at CSDL. The Semianalytical Satellite Theory developed at CSDL has been implemented in this version of RD GTDS. This version of RD GTDS also contains an LKF and EKF capability, implemented by the FILTER program. Many of the FILTER subroutines are also used by the SKF and ESKF. The program development of the SKF and ESKF is summarized below as well as the set up for execution.

B.1 Software Description

Four new subroutines were written and forty-four existing subroutines were modified in this thesis work. Twenty-one of these routines were written or modified for SKF and ESKF implementation, nine for test case support, and eighteen for bug correction and code clarification.

B.1.1 SKF and ESKF Subroutine Descriptions

Short descriptions of the subroutines written and modified for filter implementation follow:

COREST: Updates the integration nominal trajectory with the current filtered correction; modified to allow SKF and ESKF updates and CDRAG and CSOLAR solve.

ESTSET: Sets switches for APG and SPPG model selection; modified to set SKF and ESKF options.

GVCVL: Sets output titles; modified to include mean equinoctial variable names.

KF: The Kalman Filter executive routine; modified to eliminate unnecessary computations to allow efficiency tests.

KFEND: Does end of filtering processing by making the final nominal trajectory update and propagating the estimate and covariance to the report time; modified for SKF and ESKF operation.

KFHIST: A new routine that generates filter state and covariance histories at observation times in cartesian, Keplerian, and mean equinoctial coordinates.

KFOBS: Controls acceptance of the next observation, propagation of the nominal trajectory, and computation of the predicted observation for Kalman Filter operation; modified to accumulate statistics on edited observations and observation residuals.

KFPRED: Implements the Kalman Filter state and covariance propagation equations; modified to interact with ORBITV for semianalytical state transition matrix computation and ESKF state prediction.

KFSTRT: Initializes the filter correction vectors and observation statistics; modified to initialize observation residual statistics.

KFUPDT: Implements the Kalman Filter state and covariance update equations; modified to accumulate observation residual statistics and to control state and covariance history output.

OBSPRT: Controls the computation of observation partials; modified for SKF and ESKF computations to account for the mean equinoctial to osculating position and velocity transformation partials (partials computation is controlled by ORBITV).

ORBITV: The executive for the Semianalytical Satellite Theory equations of motion and variational equations. Controls AOG and SPG computations (SPORB) and APG and SPPG computations (SKFPRT); modified to control SKF and ESKF nominal trajectory updates and ESKF state correction prediction and updated state computation.

OUTSLV: Prints the filter estimate and covariance at the initial report time; modified to allow mean equinoctial variables.

RESINV: Performs initialization tasks for the Semianalytical integrator by initializing the state and the partials; modified to initialize the mean equinoctial state transition matrix.

RKINTG: The variable order Runge Kutta integrator for the Semianalytical equations of motion and variational equations, written by A. Bobick [20]; modified to integrate the inverse of the state transition matrix.

RPTEST: Prints the filter estimate and covariance at the final report time; modified to allow mean equinoctial variables.

SKFMAT: A new routine that computes the transformation partials from the mean equinoctial plus dynamic parameters solve vector to the corresponding osculating equinoctial variables (i.e., implements the SPPG).

SKFPRT: A new routine that controls computation of the Semianalytical state transition matrix (uses the transition matrix inverse interpolator set up by RKINTG) and the computation of the Semianalytical solve vector to osculating position and velocity transformation partials (implements a local interpolator) required by OBSPRT.

SKFUDT: A new routine that updates the Semianalytical nominal trajectory and reinitializes the integrator at the end of an integration grid.

SNGSTP: Generates the first integration grid and short periodic coefficient interpolators for Semianalytical Runge Kutta integrator; modified to set up the state transition matrix interpolator.

SPORB: Controls calculation of the osculating position and velocity and mean equinoctial elements for the Semianalytical integrator at output times within the current integration grid. Implements the local position and velocity interpolator and uses the short periodic coefficient interpolators; modified to make ESKF updated state computations more efficient.

B.1.2 Test Case Support Subroutine Descriptions

Modifications to nine subroutines were required to support three aspects of the SKF and ESKF testing; summaries of the requirements and the subroutine descriptions follow.

The coefficient of drag was estimated in two test cases to improve estimation performance; one subroutine was modified to support this capability for the LKF and EKF.

AERO: Computes atmospheric drag forces and partial derivatives; modified to calculate CDRAG partials for CDRAG estimation by the LKF and EKF.

Two of the test cases required the capability to have station-specific observation statistics for C-Band tracking stations. Four subroutines were modified for this capability:

DSPEXC: This routine is the executive for the DATASIM capability in RD GTDS; it was modified to allow the simulation of observations of the same type with different error statistics.

OUTDS1: Prints the observation statistics summary for the DATASIM program; modified to account for station-specific statistics.

SETDC: One of the RD GTDS control card processors; modified to read in station-specific observation statistics.

WEIGHT: Computes the weight assigned to each observation residual by differential corrections and filter programs; modified to account for station-specific observation statistics.

Implementation of the process noise transformation between mean equinoctial and osculating position and velocity frames required modifying three routines. One routine was modified to support the real data process noise computation.

AVRAGE: Computes the Semianalytical mean element rates; modified to print the rate history for gravitational and drag perturbations for the real data process noise calculation.

ANOISE: Computes the process noise covariance contribution to the Kalman Filter prediction equations; modified to include the equinoctial to cartesian process noise transformations.

SETAPC: Initializes the Kalman Filter a priori and process noise covariances; modified to account for process noise transformation initialization.

SETFIL: The control card processor for the RD GTDS FILTER program; modified to allow control card input of the process noise transformation option.

B.1.3 Software Bug Removal

Eighteen subroutines were modified to remove errors or clarify the code. Since the corrections are specific to the particular subroutine implementations, only the subroutine names are given here. The modified routines are EDITOR, ELERD, EO, KFINIT, OBEDIT, OBS, OBSWF, OBSWT, OUTPAR, RPTIME, RSETRK, SETRUN, SPCOTO, SPJ2PR, VARSP, VRSPAN, VRSPFD, and WFCONT.

B.1.4 Interaction Diagrams

Software interaction diagrams for key routines of Section B.1.1 and B.1.2 are shown in Figure B-1. See reference [3] for additional information.

B.2 Program Execution

This section describes the setup of the JCL, RD GTDS control cards, and software flags in subroutines ESTSET and HWIRE as required for SKF and ESKF program runs.

B.2.1 JCL Setup

Up to three data sets may be required for an SKF or ESKF run.

The Linkage Loader control cards describing the overlay structure are currently in

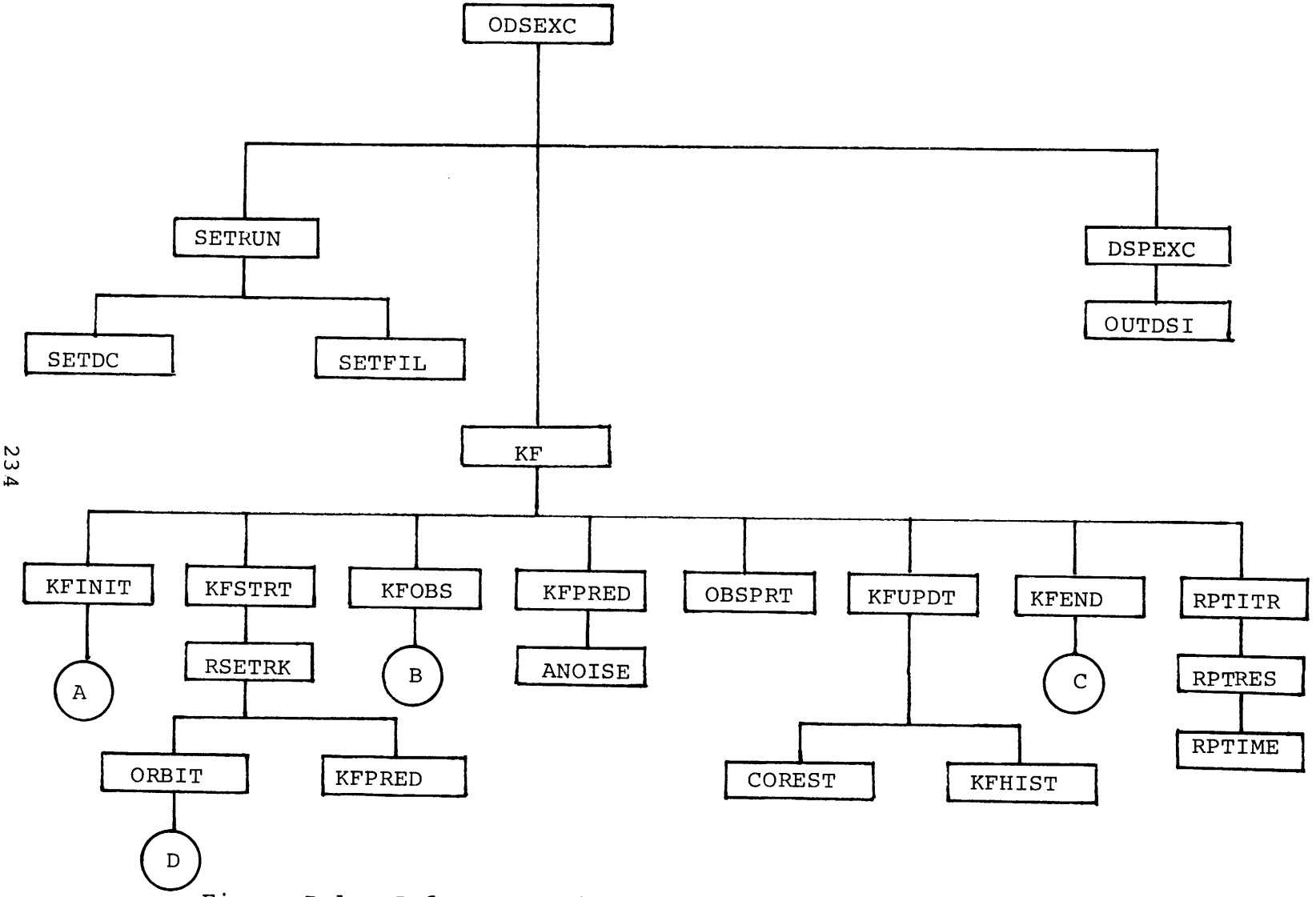

Figure B-1. Software Interaction Diagrams (page 1 of 3)

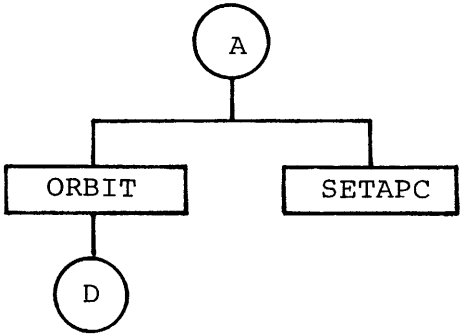

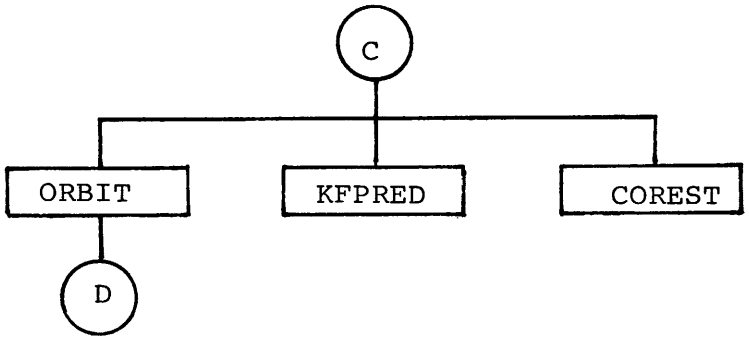

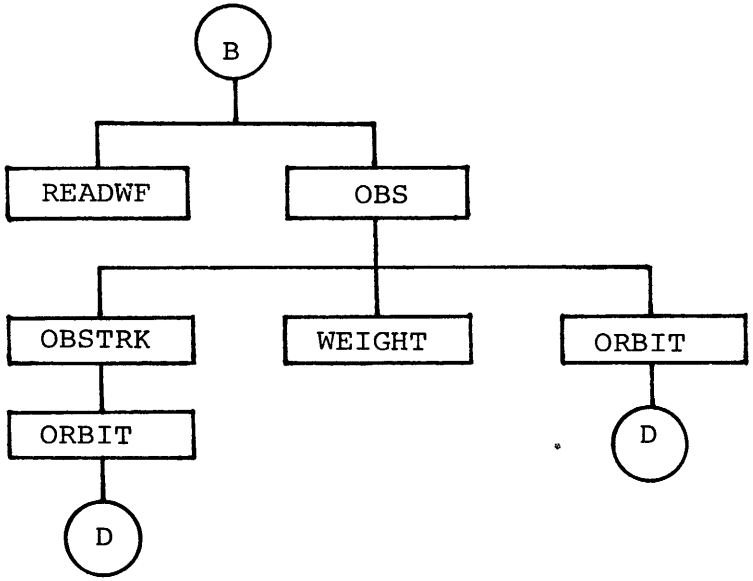

Figure B-1. Software Interaction Diagrams (page 2 of 3)

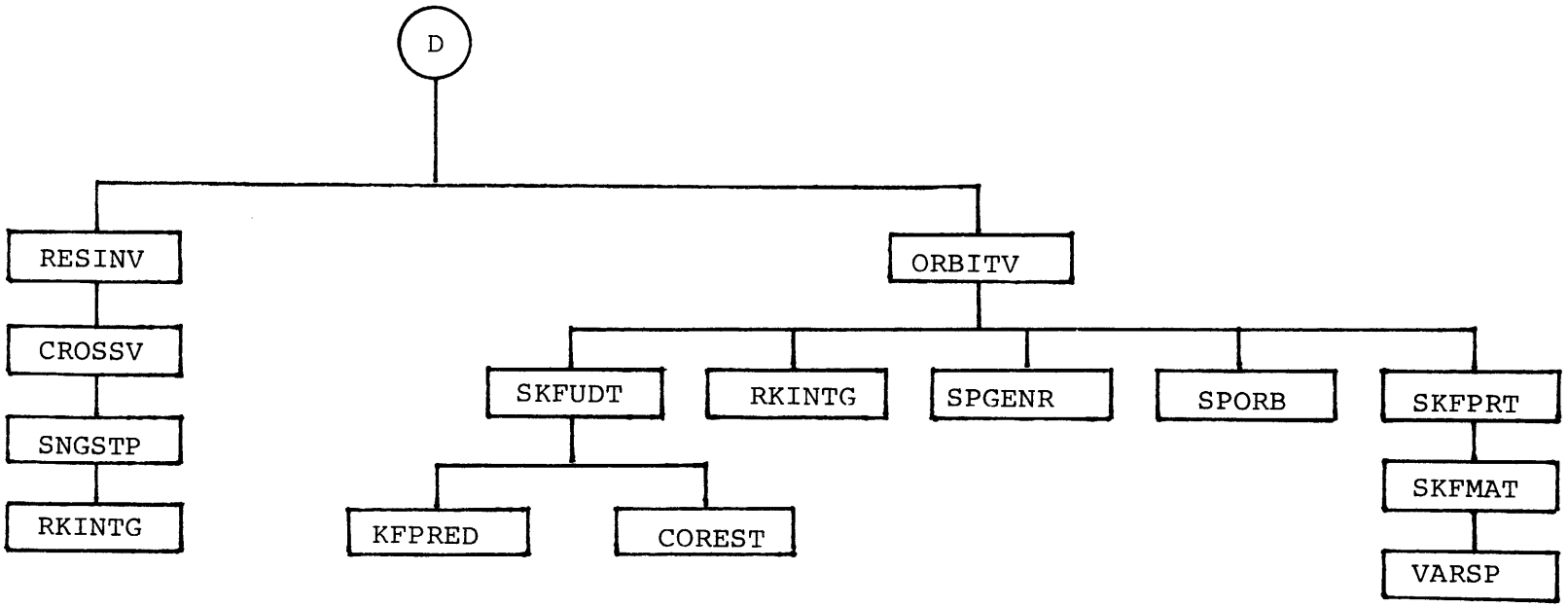

Figure B-1. Software Interaction Diagrams (page 3 of 3)

SPT1244.SKF.GTDS.OVERLAY.OBJ

The source code, INCLUDE statements, and load modules for the updated routines of Section B.1 are in

	FORT
SPT1244.GTDS.UPDATE.	OBJ
	LOAD

respectively.

The state and covariance histories may be generated on output data sets for plotting by setting the flags (discussed below) IWUPD, IWPRD, and IPRFIL. Data sets of the required format can be generated by the ALLDS command.

B.2.2 RD GTDS Control Cards

The RD GTDS control cards directly impacting the SKF and ESKF operation as well as the new control card implemented for station-specific observation statistics are described here.

The selection of an extended-type Kalman Filter versus a linearized-type filter remains unchanged from the previous FILTER implementation but is repeated here for emphasis. The pertinent control card is

col 1-8	9-11	12-14
FILTER	I	J

The variable I=1 selects either the LKF or SKF, while I=2 selects the EKF or ESKF. The variable J=1 indicates that process noise covariances should be computed.

Selection between semianalytical and Cowell filters (e.g., LKF vs. SKF or EKF vs. ESKF) for the same FILTER card is accomplished by the ORBTYPE card. This card selects the orbit generator type; it has the format

col 1-8	9-11	12-14	15-17	18-28	39-59
ORBTYPE	I	J	K	S	T

The pertinent variables are I, S, and T. Setting I=5 selects the Semianalytical Filter while I=10 selects the Cowell version. The variable S sets the integrator step-size; typical values are S=10 for Cowell and S=21600 for Semianalytical integrations. The variable T=1 is required for semianalytical runs.

The process noise transformation from the equinoctial frame to the cartesian frame for making a LKF or EKF run analogous to a SKF or ESKF run is set by the INPUT card; the format of this card is

col 1-8	9-11
INPUT	I

The variable I=1 selects inertial cartesian process noise, while I=2 triggers the transformation. The process noise strength is input by SPNOISE cards as described in [3]; when I=2 the input strength is taken to be in equinoctial coordinates.

The new control card implementing the station-specific observation statistics is called the "station card zero" card by analogy with GTDS terminology for the control cards describing other properties of the tracking station network. The new card has the form

col 1	2-8	9	10-11,12-14,15-17			18-38,39-59,60-80		
/	statname	0	I_1	I_2	I_3	R_1	R_2	R_3

where

statname = a legal RD GTDS station name

I_1, I_2, I_3 = RD GTDS observation type

R_1, R_2, R_3 = the corresponding observation standard deviation

The appropriate units are meters, centimeters per second, and arc seconds for range, range rate, and angle measurements, respectively.

B.2.3 Software Switches

The software switches required for SKF and ESKF operation are set in the subroutine ESTSET, but interaction of the ESKF with the position and velocity interpolator requires the discussion of the subroutine HWIRE. Before the implementation of SKF software, these subroutines selected the semianalytical variational equations (APG + SPPG) and equations of motion (AOG + SPG) force model options, respectively.

The flags added to ESTSET affect filter operation and intermediate output. The output flags are summarized in Table B-1. There are three flags that determine SKF and ESKF operation and one flag that enables the LKF to emulate SKF operation by relinearization of the nominal trajectory.

The flag IUPD=1 causes relinearization of the Semi-analytical nominal trajectory for the SKF and ESKF at the end of an integration grid by adding the filter correction to the final grid state; when IUPD=2 the semianalytical linearization is global over the observation span.

The flag INTINV=1 turns on the state transition matrix inverse interpolator; otherwise, the required inverse is computed explicitly.

The flag ILKFUP=1 causes LKF relinearization at intervals specified by DTLKF. Otherwise, the linearization is global.

The selection of the ESKF versus the SKF is controlled by the flag IESKF. When IESKF=2, the SKF is selected. The choice of the ESKF observation prediction equations changes according to whether or not the local position and velocity interpolator is being used. The different equations employed in the two cases are discussed in Chapter 3. The position and velocity interpolator is switched on and off in the routine HWIRE; INTPOS=1 turns the interpolator on, INTPOS=2 turns it off. The corresponding settings of the flag IESKF are IESKF=3 and IESKF=1. Both ESKF implementations assume that the short periodic coefficient interpolator is on.

Table B-1
Print Flag Settings
(1 = ON; 2 = OFF)

ISLVPT	print the nominal trajectory elements before and after adding in the filter correction
IWPRD	print the filter state and covariance in cartesian, keplerian, and mean equinoctial (for SKF/ESKF) elements as predicted at the current observation time
IWUPD	print the corresponding state and covariances after the measurement update
IPRFIL	this set the output FRN for the filter history (e.g., =43 implies output on FT43F001)

REFERENCES

1. Koenkiewicz, R., and A. J. Fuchs, "An Overview of Earth Satellite Orbit Determination," AAS 79-107, presented at the AAS/AIAA Astrodynamics Conference, Provincetown, Mass., June 1979.

2. Kes, F. C., R. G. Lagowski, and A. J. Grise, "Performance of the TELESAT Real-Time State Estimator," AIAA preprint 80-0573.

3. Dunham, J. B., R&D GTDS Filter Program Software Specifications and User's Guide, CSC/SD-79/6032, January 1980.

4. Hoots, F. R., and Roehrich, R. L., "Models for Propagation of NORAD Element Sets," Project SPACETRACK Report No. 3, December 1980, Aerospace Defense Command, Peterson AFB, CO.

5. Mathematical Foundation for SCC Astrodynamic Theory, Aerospace Defense Command Space Computational Center Program Documentation, DCD3, September 1977.

6. Van Dierendonck, Melton, Birnbaum, and Harkins, "The Approach to Satellite Ephemeris Determination for the NAVSTAR Global Positioning System," Navigation, J. of Inst. Nav., Vol. 23, No. 1, Spring 1976.

7. Battin, Croopnik, and Lenox, "The Epoch State Navigation Filter," AIAA J. of Guidance and Control, Vol. 1, No. 5, Sept. 1978.

8. Menendez, The Epoch State Filter Performance in a Semiautonomous Navigation System, S.M. Thesis, Massachusetts Institute of Technology, Cambridge, Mass., February 1981.

9. McClain, W. D., A Recursively Formulated First Order Semianalytic Artificial Satellite Theory Based on the Generalized Method of Averaging, Volume 1, NASA-CR-156782, N78-28147, November 1977.

10. Cefola, "A Recursive Formulation for the Tesseral Disturbing Function in Equinoctial Variables," No. 76-839, AIAA/AAS Astrodynamics Conference, San Diego, Calif., August 1976.

11. McClain, W. D., A Recursively Formulated First Order Semianalytic Artificial Satellite Theory Based on the Generalized Method of Averaging, Volume 2, NASA-CR-156783, N78-28148, 1978.

12. Collins, S. K., Long Term Prediction of High Altitude Orbits, Ph.D. Dissertation, Department of Aeronautics and Astronautics, Massachusetts Institute of Technology, Cambridge, Mass., March 1981.

13. Green, A. J., Orbit Determination and Prediction Processes for Low Altitude Satellites, Ph.D. Dissertation, Department of Aeronautics and Astronautics, Massachusetts Institute of Technology, Cambridge, Mass., December 1979.

14. Cefola, P., and McClain, W. D., "A Recursive Formulation of the Short-Periodic Perturbations in Equinoctial Variables," AIAA Preprint 78-1383, presented at the AIAA/AAS Astrodynamics Conference, Palo Alto, Calif., August 1978.

15. McClain, W. D., and Slutsky, M. S., "A Theory for the Short Period Motion of an Artificial Satellite," presented as Paper No. AIAA-80-1658 at the AIAA/AAS Astrodynamics Conference, Danvers, Mass., August 11-13, 1980.

16. Zeis, E. G., A Computerized Algebraic Utility for the Contruction of Non-Singular Satellite Theories, M.S. Thesis, Massachusetts Institute of Technology, Cambridge, Mass., September 1978.

17. Slutsky, M. S., and McClain, W. D., "The First-Order Short Periodic Motion of an Artificial Satellite Due to Third Body Perturbations," Paper No. AAS 81-106, presented at the AAS/AIAA Astrodynamics Conference, Lake Tahoe, Nevada, August 3-5, 1981.

18. Proulx, McClain, Early, and Cefola, "A Theory for the Short Periodic Motion Due to the Tesseral Harmonic Gravity Field," Paper No. 81-130, presented at the AAS/AIAA Astrodynamics Conference, Lake Tahoe, Nevada, August 3-5, 1981.

19. Early, L., and Cefola, P., unpublished work, C. S. Draper Laboratory, Inc., Cambridge, Mass., 1980-1981.

20. Jazwinski, Stochastic Processes and Filtering Theory, Academic Press, New York, 1970.

21. McClain, Long, and Early, "Development and Evaluation of a Hybrid Averaged Orbit Generator," Paper No. 78-1382, AIAA/AAS Astrodynamics Conference, Palo Alto, Calif., August 1978.

22. Broucke, R., and Cefola, P., "On the Equinoctial Orbit Elements," Celestial Mechanics, 5, 303-310, 1972.

23. Bobick, A., unpublished work, C. S. Draper Laboratory, Inc., Cambridge, Mass., 1979.

24. Jazwinski, "Adaptive Filtering in Satellite Orbit Determination," presented at the 2nd Asimolar Conference on Circuits and Systems, Pacific Grove, Calif., October 1968.

25. Jazwinski, "Nonlinear and Adaptive Estimation in Re-entry," Paper No. 72-374, AIAA Guidance and Control Conference, Stanford, Calif., August 1972.

26. Widnall, "Enlarging the Region of Convergence of Kalman Filters Employing Range Measurements," AIAA Journal, Vol. 11, No. 3, March 1973.

27. Athans, Wishner, and Bertolini, "Suboptimal State Estimation for Continuous-Time Nonlinear Systems from Discrete Noisy Measurements," IEEE Transactions Automatic Control, Vol. AC-13, No. 5, October 1968.

28. Denham and Pines, "Sequential Estimation when Measurement Function Nonlinearity is Comparable to Measurement Error," AIAA Journal, Vol. 4, No. 6, June 1966.

29. Gelb, ed., Applied Optimal Estimation, The MIT Press, Cambridge, Mass., 1974.

30. Shaver, J. S., Formulation and Evaluation of Parallel Algorithms for the Orbit Determination Problem, Ph.D. Dissertation, Department of Aeronautics and Astronautics, Massachusetts Institute of Technology, Cambridge, Mass., March 1980.

31. Walter, "Conversion of Osculating Orbital Elements into Mean Elements," Astronomical Journal, Vol. 72, No. 8, October 1967.

32. May, "A Study of the Effects of State Transition Matrix Approximations," presented at the Flight Mechanics/Estimation Theory Symposium, Goddard Space Flight Center, Maryland, October 1979.

33. Dowd, Adaptive Estimation of Atmospheric Drag on Near Earth Satellites, IASOM TR 77-4, Univ. of Texas at Austin, December 1977.

34. Myers, Filtering Theory Methods and Applications to the Orbit Determintion Problem for Near-Earth Satellites, Ph.D. Dissertation, Univ. of Texas at Austin, 1974.

35. Wright, "Sequential Orbit Determination with Auto-Correlated Gravity Modelling Errors," J. Guidance and Control, Vol. 4, No. 3, May 1981.

36. Lerch, Klosko, Laubscher, and Wagner, Gravity Model Improvement Using GEOS-3 (GEM 9 and 10), Goddard Space Flight Center, September 1977.

37. Barlier, Falin, Ill, and Jaeck, "Structure of the Neutral Atmosphere Between 150 and 500 km," Space Research, XIII, 1973.

38. Hickman, Ching, Rice, Sharp, and Straus, A Survey of Currently Important Empirical Thermospheric Models, The Aerospace Corportion, Report No. SSL-78(3960-04)-3, April 1978.

39. Rugge, "Comparison of Densities Deduced From Radar Determined Orbital Decay and Accelerometer Measurements," Space Research, XIV, 1974.

40. J. Pilkington and D. King-Hele, Table of Earth Satellites, Vol. 3, 1974 to 1978, Royal Aircraft Establishment, Farnborough, England, January 1980.

41. R. Smith, Task 757 Final Report Precision Orbit Studies, Computer Science Corporation Report CSC/TM-80/6029, October 1980.